

# Design and Performance Analysis of PCF Based Plasmonic Biosensor with Optimized Asymmetric Slotted Airhole

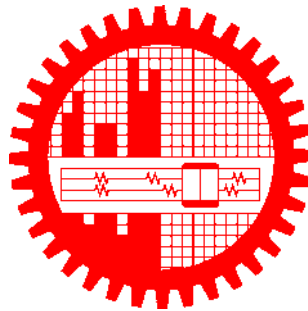
by

Hasan Sarker

Submitted to

Department of Electrical and Electronic Engineering

in partial fulfillment of the requirements for the degree of  
Masters of Science in Electrical and Electronic Engineering



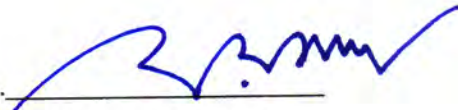
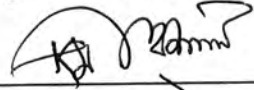

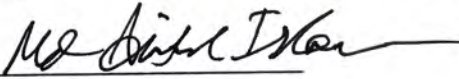
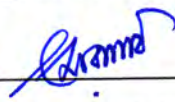
Department of Electrical and Electronic Engineering  
Bangladesh University of Engineering and Technology  
(BUET)

Dhaka - 1205, Bangladesh

January 2022

This thesis titled, “**Design and Performance Analysis of PCF Based Plasmonic Biosensor with Optimized Asymmetric Slotted Airhole,**” submitted by Hasan Sarker, Roll No.:1017062264, Session: October 2017, has been accepted as satisfactory in partial fulfillment of the requirement for the degree of MASTERS OF SCIENCE IN ELECTRICAL AND ELECTRONIC ENGINEERING on 08<sup>th</sup> January 2022.

## BOARD OF EXAMINERS

1.   
Dr. Mohammad Faisal  
Professor  
Department of Electrical and Electronic Engineering,  
Bangladesh University of Engineering and Technology, Dhaka.  
Chairman  
(Supervisor)
2.   
Dr. Md. Kamrul Hasan  
Head and Professor  
Department of Electrical and Electronic Engineering,  
Bangladesh University of Engineering and Technology, Dhaka.  
Member  
(Ex-Officio)
3.   
Dr. Md. Shah Alam  
Professor  
Department of Electrical and Electronic Engineering,  
Bangladesh University of Engineering and Technology, Dhaka.  
Member
4.   
Dr. Md. Asiful Islam  
Associate Professor  
Department of Electrical and Electronic Engineering,  
Bangladesh University of Engineering and Technology, Dhaka.  
Member
5.   
Dr. Mohammad Rakibul Islam  
Professor  
Department of Electrical and Electronic Engineering,  
Islamic University of Technology, Gazipur.  
Member  
(External)

## Candidate's Declaration

This is to certify that the work presented in this thesis entitled, "Design and Performance Analysis of PCF Based Plasmonic Biosensor with Optimized Asymmetric Slotted Air-hole," is the outcome of the research carried out by Hasan Sarker under the supervision of Dr. Mohammad Faisal, Professor, in the Department of Electrical and Electronic Engineering, Bangladesh University of Engineering and Technology (BUET), Dhaka-1205, Bangladesh.

It is also declared that neither this thesis nor any part of this work has been submitted anywhere else to award of any degree, diploma, or other qualifications.

Signature of the Candidate



---

Hasan Sarker  
1017062264

*Dedicated to our beloved Prophet (PBUH)*

# Acknowledgement

First and foremost, I offer my sincere gratitude and indebtedness to my thesis supervisor, Professor Dr. Mohammad Faisal, for his continuous and constant supervision and support throughout my thesis with his patience and knowledge. I shall ever remain grateful to him for his valuable guidance, advice, encouragement, cordial and amiable contribution to my view. He helped me a lot in every aspect of this work and guided me with proper directions whenever I searched for one. He acted as my supervisor and helped me make important decisions in my academic career. His patient hearing of my ideas, critical analysis of my observations, and detection flaws in my thinking and writing have been invaluable (especially during research articles). I also want to thank him for affording so much time for me to explore the areas of my research and new ideas and improve the writing of this dissertation.

I want to thank Aslam Mollah, Assistant professor, Dept. of ETE, RUET. His constant help, valuable suggestions, and proper guideline motivated and contributed to completing this work properly. He spent valuable time from his busy schedule, for which I am incredibly grateful to him. I would like to thank my thesis committee members for their helpful suggestions. I thank Dr. Md. Kamrul Hasan, Dr. Md. Shah Alam, Dr. Md. Asiful Islam and especially the external member Dr. Mohammad Rakibul Islam. In this regard, I remain ever grateful to my parents, my family, without whose prayers and constant support I could never reach this stage of my life.

Lastly, I am grateful to almighty Allah for keeping me safe and sound and redirecting me to the right path while chasing the wrong.

# Abstract

Nowadays, sensors are being miniaturized due to the high demand for lightweight, small size, portable, compact structure, highly efficient, real-time, and cost-effective devices for sensing applications. Photonic crystal fiber (PCF) fulfills the demand mentioned above, providing an excellent guiding property and design freedom. Surface plasmon resonance (SPR) refers to the coupling of the surface plasmon wave and electromagnetic wave in between the metal-dielectric interface. It offers a highly sensitive, efficient, label-free, and real-time sensing technique. So, the combination of the PCF with SPR technology fulfills the all requirements of biosensors. To introduce the widely known SPR phenomenon, deposition of metals is compulsory. The sensing performance of a biosensor is highly dependent on the suitable selection of plasmonic material.

In this dissertation, a novel PCF-SPR biosensor is numerically characterized with high sensing performance for bio-analyte sensing particularly in the analyte refractive index (RI) ranging from 1.29 to 1.42. The proposed PCF-SPR sensor consists of a solid silica core and adjacent rectangular air holes in the cladding region. The entire outer surface of the proposed sensor is covered by a thin gold film to introduce the widely known SPR phenomenon. Sensing methodology is appropriately addressed and each of the designed parameters of the sensor structure is tuned sufficiently to find out the desired sensing performance. Finite element method (FEM) based mode solver software (COMSOL Multiphysics version 5.3a) is used with the help of Matlab interface to investigate the performance of the proposed sensor. Considering RI changes at the outer surface, appealing sensing performance such as maximum wavelength sensitivity of 2,16,000 nm/RIU and maximum amplitude sensitivity of 1138.52 RIU<sup>-1</sup> is attained. In addition, the proposed sensor possesses a resolution of  $4.63 \times 10^{-7}$  RIU, linearity of 0.9861, a figure of merit of 1981.651 RIU<sup>-1</sup>, and detection accuracy of 0.019802 nm<sup>-1</sup>. However, the promising sensing characteristics of the proposed sensor indicate its potential to be effectively used for the perfect detection of the biochemical and organic samples in biochemical industries.

# Contents

<b>Certification</b>	<b>i</b>
<b>Candidate's Declaration</b>	<b>ii</b>
<b>Dedication</b>	<b>iii</b>
<b>Acknowledgement</b>	<b>iv</b>
<b>Abstract</b>	<b>v</b>
<b>List of Figures</b>	<b>x</b>
<b>List of Tables</b>	<b>xiii</b>
<b>List of Abbreviations</b>	<b>xvi</b>
<b>List of symbols</b>	<b>xvii</b>
<b>1 Introduction</b>	<b>1</b>
1.1 Introduction . . . . .	1
1.2 Literature Review . . . . .	1
1.3 Problem Statement . . . . .	3
1.4 Objectives of the Thesis . . . . .	4
1.5 Possible Outcome . . . . .	5
1.6 Methodology . . . . .	5
1.7 Thesis Outline . . . . .	6
<b>2 Theoretical Background and Methodology</b>	<b>7</b>
2.1 Introduction . . . . .	7
2.2 Optical Sensor . . . . .	8
2.3 Optical Biosensor Principles . . . . .	8
2.4 Interferometry . . . . .	9
2.5 Luminescence . . . . .	9
2.6 Fundamental of SPR . . . . .	10
2.7 Conventional SPR Mechanism . . . . .	11

2.7.1	Prism Coupler . . . . .	11
2.7.1.1	Otto Configuration . . . . .	12
2.7.1.2	Kretschmann Configuration . . . . .	13
2.7.2	Grating Coupler . . . . .	14
2.7.3	Fiber Based SPR Configuration . . . . .	14
2.8	PCF . . . . .	14
2.9	PCF Based SPR Sensing . . . . .	16
2.10	Interrogation of Surface Plasmon Waves . . . . .	17
2.10.1	Amplitude Interrogation . . . . .	18
2.10.2	Wavelength Interrogation . . . . .	18
2.10.3	Phase Interrogation . . . . .	18
2.10.4	Angular Interrogation . . . . .	19
2.10.5	Polarization Interrogation . . . . .	19
2.11	SPR in Biosensing . . . . .	19
2.12	Numerical Methods . . . . .	20
2.12.1	FEM . . . . .	20
2.12.2	Formation of FEM . . . . .	21
2.13	Optical Tunable Source . . . . .	22
2.14	Optical Spectrum Analyzer . . . . .	22
2.15	Refractive index of some analytes . . . . .	23
2.16	Summary . . . . .	24
<b>3</b>	<b>Modeling and Performance Parameters</b>	<b>25</b>
3.1	Introduction . . . . .	25
3.2	Design with Theoretical Modeling . . . . .	25
3.2.1	Design Approach . . . . .	26
3.2.2	Selected Material Properties . . . . .	28
3.2.3	Perfectly Matched Layer . . . . .	29
3.2.4	Proposed Block Diagram Specimen . . . . .	29
3.3	Numerical Analysis . . . . .	30
3.3.1	Confinement Loss . . . . .	30
3.3.2	Wavelength Sensitivity . . . . .	31
3.3.3	Amplitude Sensitivity and Sensor Length . . . . .	31
3.3.4	Sensor Resolution . . . . .	31
3.3.5	FOM and Detection limit . . . . .	32
3.4	Fabrication Feasibility Study . . . . .	32
3.5	Summary . . . . .	33
<b>4</b>	<b>Simulation Results and Discussion</b>	<b>34</b>



4.1	Introduction . . . . .	34
4.2	Optimization of structural and performance reinforcement parameters . . . . .	34
4.2.1	Normal Approach of air holes . . . . .	35
4.2.1.1	Variation of the gold layer thickness . . . . .	35
4.2.1.2	Variation of Air Hole Height . . . . .	36
4.2.1.3	Effect of Inclination . . . . .	37
4.2.2	Inclined Approach . . . . .	38
4.2.2.1	Inclination of Air holes . . . . .	39
4.2.2.2	Thickness variation of the gold layer . . . . .	40
4.2.2.3	Variation of Air Hole height . . . . .	42
4.2.2.4	Variation of Air Hole Width . . . . .	44
4.2.2.5	Addition and Effect of the Adhesive Layer . . . . .	46
4.2.2.6	Effect of Metallic Stripe . . . . .	47
4.2.2.7	Thickness Variation of Analyte Layer . . . . .	48
4.2.2.8	Thickness Variation of PML . . . . .	49
4.3	Performance Analysis . . . . .	50
4.3.1	Dispersion relationship . . . . .	50
4.3.1.1	Normal Approach . . . . .	51
4.3.1.2	Inclined Approach . . . . .	51
4.3.2	Confinement Loss . . . . .	52
4.3.2.1	Normal Approach . . . . .	53
4.3.2.2	Inclined Approach . . . . .	54
4.3.3	Wavelength Sensitivity . . . . .	54
4.3.3.1	Normal Approach . . . . .	55
4.3.3.2	Inclined Approach . . . . .	55
4.3.4	Linearity . . . . .	57
4.3.5	Amplitude Sensitivity and Sensor length . . . . .	57
4.3.5.1	Normal Approach . . . . .	59
4.3.5.2	Inclined Approach . . . . .	60
4.3.6	Sensor Resolution . . . . .	60
4.3.6.1	Normal Approach . . . . .	62
4.3.6.2	Inclined Approach . . . . .	62
4.3.7	Performance Analysis with Double Layer PM . . . . .	63
4.3.8	Application . . . . .	64
4.3.8.1	Concentration Detection of Sucrose Solution . . . . .	65
4.3.9	Summary . . . . .	67
<b>5</b>	<b>Conclusions</b>	<b>68</b>
5.1	Conclusions . . . . .	68

5.1.1	Normal Approach . . . . .	68
5.1.2	Inclined Approach with Single PM . . . . .	69
5.1.3	Inclined Approach with Double PM . . . . .	69
5.2	Future Prospects of Our Work . . . . .	69

<b>References</b>		<b>71</b>
-------------------	--	-----------

# List of Figures

2.1	Interferometry a) Fiber optic version and b) Integrated optic version, adapted from Ref [39]. . . . .	9
2.2	The propagation of SPW wave at metal and dielectric interface, adapted from Ref [38] . . . . .	10
2.3	Commonly used coupling mechanism a) Prism coupler, b) Grating coupler, and c) Optical wave-guide based SPR, adapted from Ref [9]. . . . .	12
2.4	Otto coupling mechanism, adapted from Ref [44]. . . . .	13
2.5	Kretschmann coupling Configuration, adapted from Ref [44]. . . . .	13
2.6	Fiber based SPR Configuration adapted from Ref [44]. . . . .	14
2.7	Basic graphical setup of practical sensing using a proposed sensor with sample output response . . . . .	16
2.8	Biosensing using the SPR principle adapted from Ref [50] . . . . .	20
2.9	Finite element method. . . . .	21
3.1	A cross-section view of the proposed sensor's geometrical structure with the air holes' normal approach. . . . .	26
3.2	Cross-sectional view of the geometrical structure of the proposed sensor with the inclined approach of the air holes. . . . .	27
3.3	(a) Cross-sectional view of the proposed geometrical structure with inclined air holes, (b) to (d) step by step development process, and (e) Block diagram for sensing analytes using the proposed sensor. (CPU: Central Processing Unit; PML: Perfect Matched Layer; PCF: Photonic Crystal Fiber) . . . . .	29
4.1	Confinement loss with different thicknesses of Gold layer ( $t_g$ ). . . . .	35
4.2	Effect of air holes height on confinement loss with RI = 1.38 and 1.39. . . . .	36
4.3	Effect of the height of air holes on AS with RI = 1.38 and 1.39. . . . .	37
4.4	Effect of inclination on confinement loss with RI = 1.38. . . . .	38
4.5	Angular rotation of the air holes with $\Phi$ (a) $0^\circ$ to (s) $90^\circ$ with a increment of $5^\circ$ for the geometrical structure of the proposed sensor. . . . .	39
4.6	Effect of angular rotation of the air holes on (a) CL and (b) AS with RI of 1.38 and 1.39 for the geometrical structure of the proposed sensor. . . . .	40

4.7	Effect of gold layer thickness on (a), (c) CL and (b), (d) AS with $\Phi = 35^\circ$ and $0^\circ$ respectively for RI of 1.38 and 1.39 of the proposed geometrical sensor structure. . . . .	42
4.8	Effect of air-hole height on (a), (c), (f) CL and (b), (d), (f) AS with $\Phi = 35^\circ$ and $t_{au} = 25$ nm for RI of 1.38 and 1.39 of the proposed geometrical sensor structure. . . . .	43
4.9	Effect of air-hole width on (a), (c), (f) CL and (b), (d), (f) AS with $\Phi = 35^\circ$ and $t_{au} = 25$ nm for RI of 1.38 and 1.39 of the proposed geometrical sensor structure. . . . .	45
4.10	Geometrical structure of the proposed sensor with the adhesive layer. . .	46
4.11	Effect of the adhesive layer on (a) CL and (b) AS with RI of 1.38 and 1.39 for the geometrical structure of the proposed sensor. . . . .	47
4.12	Effect of the metallic stripe on (a) CL and (b) AS with RI of 1.38 and 1.39 for the geometrical structure of the proposed sensor. . . . .	48
4.13	Effect of the analyte layer on (a) CL and (b) AS with RI of 1.33 and 1.34 for the geometrical structure of the proposed sensor. . . . .	49
4.14	Effect of the PML on (a) CL and (b) AS with RI of 1.33 and 1.34 for the geometrical structure of the proposed sensor. . . . .	49
4.15	Optical field distribution for the (a) SPP Mode, (b) to (c) core guided mode for both $x$ - and $y$ - polarization (d) coupling mode. . . . .	50
4.16	Dispersion relation as a function of wavelength for the SPP mode and core mode with an analyte RI of 1.38. . . . .	51
4.17	Phase matching condition among the SPP mode, core mode (imag.), and core mode (real) for RI = 1.38. . . . .	52
4.18	Confinement loss spectrum of the proposed sensor for core mode with analytes of different RI from 1.33 to 1.43. . . . .	53
4.19	Descriptive presentation of Confinement Losses with different operating wavelength for RI of 1.29 to 1.42. . . . .	54
4.20	Graphical representation of confinement losses through intensity for analytes with RI = 1.29 to RI = 1.42. . . . .	55
4.21	Peak shift of resonant wavelength with the variation of RI. . . . .	56
4.22	Propagation length and peak shift of the proposed sensor with various RI for the inclined approach of air holes. . . . .	57
4.23	Amplitude sensitivity concerning wavelength for the value of RI from 1.33 to 1.43 in $y$ -polarized mode. . . . .	59
4.24	Sensor length with different analyte RI for normal approach. . . . .	60
4.25	Amplitude sensitivity through graphical depiction for the proposed sensor using different analytes with RI of 1.30 to 1.43. . . . .	62

4.26	Descriptive presentation of Confinement Losses with different operating wavelength for RI of 1.29 to 1.42. . . . .	63
4.27	Amplitude sensitivity through graphical depiction for the proposed sensor using different analytes with RI of 1.29 to 1.41. . . . .	64
4.28	Confinement loss (a) and Amplitude sensitivity (b) for different sucrose solutions . . . . .	67

# List of Tables

2.1	Component of permeability tensor [p] and [q]. . . . .	22
2.2	Refractive Index of different analytes within 1.29 to 1.43. . . . .	23
3.1	Optimized Parameters Used in Normal Approach of the Proposed Structure. . . . .	27
3.2	Optimized Parameters Used in Inclined Approach of the Proposed Structure. . . . .	27
4.1	Effect of $t_g$ on Confinement Loss with RI = 1.38. . . . .	36
4.2	Performance Analysis of The Sensor with Different Air-holes Height. . . . .	36
4.3	Effect of Inclination on Confinement Loss with RI = 1.38. . . . .	38
4.4	Different Geometrical Parameters optimization of the proposed sensor for RI = 1.38 and 1.39 . . . . .	41
4.5	Effect of the adhesive layer on CL and AS with RI of 1.38 and 1.39 for the geometrical structure of the proposed sensor. . . . .	47
4.6	Effect of the metallic stripe on CL and AS with RI of 1.38 and 1.39 for the geometrical structure of the proposed sensor. . . . .	48
4.7	Effect of the analyte layer thickness on CL and AS with RI of 1.33 and 1.34 for the geometrical structure of the proposed sensor. . . . .	48
4.8	Effect of the PML thickness on CL and AS with RI of 1.33 and 1.34 for the geometrical structure of the proposed sensor. . . . .	50
4.9	Performance Analysis of the Proposed Sensor for Different Analyte RI With $\Delta n_a = 0.01$ , $t_g = 30$ nm at Y-Polarized Mode. . . . .	56
4.10	Performance Investigation of the Proposed Sensor with $t_{au} = 25$ nm, $\Phi = 35$ deg. and $\Delta n_a = 0.01$ using Analytes of Different RI. . . . .	58
4.11	Performance Investigation of the Proposed Sensor with $t_{au} = 25$ nm, $t_{tio_2} = 05$ nm, $\Phi = 35$ deg. and $\Delta n_a = 0.01$ using Analytes of Different RI. . . . .	61
4.12	Relative Performance Analysis of the Suggested Sensor with the Detection Range of RI. . . . .	64
4.13	Refractive Indexes of Sucrose Solution. . . . .	65
4.14	Concentration Detection of Different Sucrose solutions. . . . .	66

5.1 Performance Comparison of Proposed Sensor for Single and Double  
PM within a Range from  $RI = 1.29$  to  $RI = 1.42$ . . . . . 69





# List of Abbreviations

AS	Amplitude Sensitivity
ATR	Attenuated Total Reflection
Au	Gold
CL	Confinement Loss
DA	Detection Accuracy
dB	Decibel
EF	Evanescent Field
EM	Electromagnetic
EW	Evanescent Wave
FEM	Finite Element Method
FOM	Figure of merit
FWHM	Full Width Half Maximum
MOF	Microstructured Optical Fiber
OSA	Optical Spectrum Analyzer
PBG	Photonic Bandgap
PCF	Photonic Crystal Fiber
PDE	Partial Differential Equation
PhC	Photonic Crystal
PM	Plasmonic Material
PML	Perfectly Matched Layer
RI	Refractive Index
RIU	Refractive Index Unit
SL	Sensor Length
SMF	Single Mode Fiber
SP	Surface Plasmon
SPP	Surface Plasmon Polariton
SPR	Surface Plasmon Resonance
SPW	Surface Plasmon Wave
SR	Sensor Resolution
TIR	Total Internal Reflection
WR	Wavelength Resolution
WS	Wavelength Sensitivity

# List of Symbols

$\Delta\lambda_{\min}$	Minimum spectral resolution
$\Delta\lambda_{\text{peak}}$	Shift of the resonance peak
$\Delta n_a$	Variations in RI
$\Gamma_L$	Spectral width of the Lorentz oscillators
$\Omega_L$	Strength of the Lorentz oscillators
$\alpha_{\text{neff}}$	Confinement loss
$\beta$	Propagation constant
$\varepsilon$	Dielectric constant
$\eta_t$	RI of TiO <sub>2</sub>
$\eta_{(\text{SiO}_2)}$	Effective RI of SiO <sub>2</sub>
$\gamma_D$	Damping coefficient
$\lambda$	Wavelength
$k_0$	Wave number
$\omega$	Angular frequency
$\omega_D$	Plasma frequency
$\theta$	Incident angle of light
$\Delta\varepsilon$	Weight factor
$\eta_{\text{eff}}$	Effective refractive index
$\mu$	Magnetic permeability
$c$	Velocity of light in free space
$E$	Electric field
$H$	Magnetic field
SiO <sub>2</sub>	Fused silica
$t$	Thickness of TiO <sub>2</sub>
$t_g$	Thickness of gold layer
TiO <sub>2</sub>	Titanium dioxide
$v$	Phase velocity

# Chapter 1

## Introduction

### 1.1 Introduction

In recent days, sensors have played an essential role in improving the quality of our daily life. For example, sensors are being used for health monitoring, health promotion, and disease detection and prevention. A fiber optic sensor usually uses optical fiber as the sensing element, and they are used to sense light, vibrations, motion, moisture, pressure, temperature, or concentration of chemical species, etc. [1]. Optical fiber sensors are widely used for remote sensing since they require no electrical power at the remote location. In addition, they can be easily fitted in small areas and can be positioned correctly due to their tiny size. In the 1980s, the first optical biosensor has been commercially developed [2]. Among different optical biosensors, plasmonic biosensor based research has been highly attracted by the researchers' community over the last few decades due to the behavior of its real-time and label-free monitoring, a wide range of sensing applications, and high sensitivity [3,4]. It is used to analyze biomolecular interactions more precisely and helps to detect chemical and biological analytes/samples. In the same way, it can be applied to biochemistry, medical sciences, environmental and industrial monitoring, food safety, drug detection, and so on [3–8].

### 1.2 Literature Review

Due to the popularity of SPR technology-based PCF sensor, a lot of research works have been investigated and reported already including i) twin core [3], ii) exposed core [9], iii) tapered core-less [10], iv) micro structured [11], v) single-mode [12], vi) doped core [13], vii) D shape (side polished) [14], viii) exposed-suspended core [6] and xi) Alphanumeric core [15], etc.

Recently, Firoz et al. has proposed an SPR based multi-analyte detection hybrid sensor through internal and external sensing with a detection range of 1.33 to 1.40 [16]. Maximum WS for external and internal approaches are 10000 nm/RIU and 12000 nm/RIU having a corresponding resolution (RIU) of  $1 \times 10^{-5}$  and  $8.33 \times 10^{-6}$ , respectively. AS in  $\text{RIU}^{-1}$  for both cases are 567 and 807, respectively. Coating internal metallic film and analyte filling/cleaning for the internal approach increases the fabrication challenges. Again, Yashar et al. has reported a D-shaped PCF PCF-based sensor for liquid analyte sensing from  $\text{RI} = 1.27$  to  $\text{RI} = 1.37$  with both external and internal sensing scheme separately for the multi-layer film [17]. In the external approach, analyte and metallic film are on the flat upper portion that removes the problem of the internal approach, but the polishing problem still exists. WS (nm/RIU) for the external approach is 22400, and WS is very low (2320 nm/RIU) for the internal scheme. A dual core PCF - SPR sensor has been reported by Mahfuz et al. for a detection range from 1.33 to 1.42 with WS (nm/RIU) of 28000 [5]. However, the author has improved sensing performance from the previously reported one but not up to the satisfactory level. Aslam et al. have proposed a suspended core localized SPR sensor with an excellent WS of 50000 nm / RIU, but AS is still low [6]. Again, the structure is not robust enough due to the single attachment of the core with the outer peripheral region.

A twin-core PCF plasmonic RI sensor was proposed by Paul et al. [18] in which maximum AS is  $10858 \text{ RIU}^{-1}$  and  $725.8918 \text{ RIU}^{-1}$  for  $y$ - and  $x$ -polarized modes respectively. The maximum WS and wavelength resolution (WR) are 9000 nm/RIU and  $1.11 \times 10^{-5} \text{ RIU}$  for both modes. Later in an identical fashion, a numerical analysis of a dual core PCF-based SPR RI sensor was submitted by Paul et al. [19] in broader sensing of analyte RI range from 1.33 to 1.41. For  $x$ - and  $y$ -polarized mode, the maximum WS and WR are 5800 nm/RIU and  $1.72 \times 10^{-5} \text{ RIU}$  and 11500 nm/RIU and  $8.7 \times 10^{-6} \text{ RIU}$ , respectively. It offered the maximum AS ( $\text{RIU}^{-1}$ ) of 554.9 and 636.5 for  $x$ - and  $y$ -polarized mode, respectively at RI of 1.40. It is noticeable that this reported work emphasized the high spectral density rather than AS for detecting wavelengths of different ranges. Both sensors mentioned above were for double-core using gold as a PM. A single-mode, highly sensitive PCF-based SPR RI sensor was proposed by Guo et al. [20] over a RI of range from 1.35 to 1.46 with a maximum WS of 1931.03 nm/RIU without taking account of AS. Also, an air-core PCF-based SPR biosensor has been introduced by Paul et al. [21] for sensing High RI ranging from 1.42 to 1.53. The maximum WS, WR, and AS obtained from this sensor are 11,700 nm/RIU,  $8.55 \times 10^{-6} \text{ RIU}$ , and  $159.7 \text{ RIU}^{-1}$ , respectively for RI of 1.42. Another highly sensitive PCF-based SPR biosensor with circular air holes and hexagonal lattice structure was designed and investigated for both gold and silver by Al Mahfuz et al. [22]. The maximum AS acquired for both silver and gold for  $y$ - polarized mode is  $1656 \text{ RIU}^{-1}$  and  $1086 \text{ RIU}^{-1}$ , respec-

tively, with the same WS and WR of 12000 nm/RIU and  $8.33 \times 10^{-6}$  RIU for both PMs. Similar work is done with H-shaped PCF-based SPR for comprehensive range RI detection by Han et al. [23] with gold coating only having WS of 25,900 nm/RIU. Bing et al. [24] designed an interesting PCF-based biosensor with the numerical analysis. They proposed simultaneous detection of a dual-channel sensor with maximum wavelength sensitivities of 11,600 nm/RIU and 10,600 nm/RIU, respectively for two channels.

However, multi-mode [25] PCF has a large core diameter compared to single-mode PCF. Twin core, tapered, and doped core PCF add additional fabrication complexities to achieve them in practice. Again, D-shaped PCF requires perfect polishing for the expected response, and mistakes during polishing may damage the fiber after fabrication. Side and dual polished, H-shaped, open ring channel, micro structured, and microwire fiber add more complexity in structure with fabrication challenges. The internal sensing process has an analyte filling problem and requires perfect cleaning for reusing them.

### 1.3 Problem Statement

Biosensor combines biological elements with physicochemical detector to detect chemical substance. Biological sensing elements are incorporated with the device to track out a specific chemical or a group of chemicals. Nowadays sensors are being miniaturized due to the high demand for lightweight, small size, portable, compact structure, highly efficient, real-time, and cost-effective devices for sensing application [7, 26]. Photonic crystal fiber (PCF) fulfills the above demand providing an excellent guiding property and design freedom [2]. Surface plasmon resonance (SPR) offers a highly sensitive, efficient, label-free, and real-time sensing technique [1, 26]. So, researchers combine PCF with SPR for the perfect detection of analytes. PCF based biosensor has many applications including different sensing applications and perfect detection of biomolecules, for example, cancer cell detection [27], food poisoning detection [28], bio-imaging [29], biochemical reaction monitoring [30], environmental and biological monitoring [20], thickness monitoring [31], chemical, biochemical, and organic chemical detection [32, 33], gas sensing [8], alcohol sensing [34] and bio-sensing [35], etc.

Apart from SPR based PCF, other sensing methods include prism coupling, modal interferometer, fiber Bragg grating, slot-wave guide and long-period fiber grating [31, 36–39], etc. However, these methods are expensive and make the devices bulky, too [38]. Again, lower sensitivity is a significant limitation reported by Tien et al. [40]. On the contrary, PCF based SPR technique builds a more accurate policy than conventional fibers or prism in controlling the propagation nature of light and evanescent fields [41]. Also, it has greater design flexibility, low sample requirements, and miniaturization

amenities [19, 20]. The shape of the PCFs can be circular, hexagonal, decagonal, octagonal, non-hexagonal, hybrid and the change of the geometry can be made easily to improve the guiding properties [18, 19, 23, 27, 39]. Aluminum, copper, silver, and gold are the commonly used noble plasmonic materials (PMs) for biosensors [39, 42]. Among them, gold and silver are used frequently for SPR biosensors [42]. The most appealing characteristic of the PCF based SPR technique is the endless single mode behavior which is independent of the used materials. It provides excellent performance and incredible versatility [18, 20]. However, multi-mode PCF has a large core diameter compared to single-mode PCF. Twin core, tapered, and doped core PCF add additional fabrication complexities to achieve them in practice. Again, D-shaped PCF needs precise polishing after fabrication and mistakes during polishing may damage the fiber. Dual polished, H-shaped, open ring channel, microstructured, and microwire fiber add more complexity in structure with fabrication challenges. The Internal sensing process has an analyte filling problem and requires perfect cleaning for reusing them. Almost all optical sensors are designed with a large number of different-sized circular air holes with fabrication challenges. Despite signs of progress, several perspectives related to the reduced number of air holes with non-circular asymmetric shapes have remained unexplored and evaluated numerically. The main aim of my work is to maximize the sensitivity of the biosensor with the most simplified and realistic design lessening fabrication complexities as well as cost. This work will replace the symmetric air-holes with asymmetric ones and reduce the total number of air-holes without sacrificing performance.

## 1.4 Objectives of the Thesis

The main objective of this thesis is to design and numerically investigate the performance of a PCF-based plasmonic biosensor with optimized asymmetric slotted air-hole. The proposed sensor will be able to detect biochemical and biological analytes. The presence of biological and biochemical analytes can be known by observing the wavelength sensitivity (WS) based on wavelength interrogation method, amplitude sensitivity (AS) based on amplitude interrogation method, linearity, and sensor resolution of resonance wavelength.

The key objectives of this research are as follows:

- i. To design and optimize a slotted photonic crystal fiber-based plasmonic biosensor for efficient, highly sensitive, and real-time sensing approach
- ii. To find out the dispersion relationship and to take into account the effect of differ-

ent design parameters for the dispersion relationship of other analytes

iii. To evaluate the sensitivity, sensor length, wavelength resolution, and figure of merit of the proposed sensor, including the inclination effect of the air holes

iv. To investigate the effect of double-layer plasmonic material instead of single-layer on the performance of the sensor and to make a trade-off between the area of plasmonic material (PM) used and sensing parameters

## 1.5 Possible Outcome

The possible outcome of this thesis is the subsequent idea development, design and optimization, performance analysis, and inclusive understanding of a novel PCF-based plasmonic biosensor with higher amplitude sensitivity, wavelength sensitivity, and lower wavelength resolution. It can be used in sensing and biosensing applications, especially as a detector of analytes such as water, acetone, ethanol, kerosene, sugar solution, etc.

## 1.6 Methodology

Commercially available software, COMSOL 5.3a, will be used for the 2D design and simulation of the geometrical model of the proposed PCF. A finite element method (FEM) will be chosen to solve Maxwell equations to determine various modal characteristics of the fiber. To characterize the PCF, an extremely fine mesh element will be selected in COMSOL 5.3a to ensure the accuracy of the simulation. During simulation, the average element quality obtained from the COMSOL 5.3a will be nearly 0.90 %, indicating less than 0.1 % computational error. A circular, perfectly matched layer (PML), which is about 10 % of the total radius of the fiber, will be employed to truncate computational regions. The proposed PCF-based biosensor will have several slots in the cladding that helps confine the light more tightly inside the core. The circular core will have only rectangular air holes in a symmetrical pattern. Such of balanced structure will reduce the complexity of the fiber without sacrificing its performance of the fiber. The frequency response of the PCF will be investigated having single layer PM with circular shape by modal analysis. Of desired modes and obtained simulated data will be plotted using ORIGIN with optimized parameters. Then the single layer PM will then be replaced by double-layer PM with proper combination to increase the sensing performance following the above-mentioned process. Again, the circular layer of PM will be replaced with arcs for double -layer PM to make a trade-off between the area of PM used and sensing parameters. Finally, the obtained results will be compared with

some existing counterparts.

## 1.7 Thesis Outline

The rest of this thesis is organized as follows.

**Chapter 2** gives an overview of an optical sensor, SPR, fundamental of SPR with different interrogation of surface plasmon wave (SPW), detailed technical review of the PCF-based SPR sensor, finding the research gap, and fixing the objectives. A short literature review is carried out, from where we conceived some instructions for further proceedings. **Chapter 3** discusses the geometry and modeling with theoretical numerical analysis and design feasibility study used in our research. The main body of **Chapter 4** is based on a slotted PCF-based SPR biosensor. Here a single model is designed and analyzed from different perspectives. Firstly, the effect of gold layer thickness and other structural reinforcement parameters and their variations on sensitivity is studied to get the optimum output response from the proposed sensor. Sensor performances are investigated based on the wavelength and amplitude interrogation methods discussed here step by step. Furthermore, the fabrication tolerance of the proposed PCF sensor is investigated. Finally, **Chapter 5** concludes the work presented in this thesis and discusses the scope for future study.



# Chapter 2

## Theoretical Background and Methodology

### 2.1 Introduction

More than a century ago, the SPR phenomenon was originated and the first steps were taken by Zenneck in 1907 [43]. He had resolved Maxwell equations and had produced a wave equation that propagates along a surface. It numerically demonstrated that electromagnetic waves in the radio spectrum synthesize at the boundary of two media. Specifically, one being the lossless dielectric medium and the other a lossy medium such as a metal or conductor. Then he had further suggested the propagation constant of the lossy medium, which is in control for the occurrence of the surface wave at the interface of metal-dielectric. Sommerfeld published two years later that Zenneck's surface waves propagated fast and decayed exponentially into both media and had an amplitude squared inverse relationship with its propagating distance from its source dipole [44]. Not much progress was made in SPR in subsequent years until 1957. In 1957 Ritchie had proven SPW excitation numerically to exist on the metal surface [45]. In the year 1959, Powell and Swan had observed the characteristics of electron energy loss spectrum involving the surface properties [46]. Not long after, in the same year, the electromagnetic wave was found to be associated with plasma radiation coupled to surface plasmon [47]. In addition to this contribution, Stern and Ferrell mathematically quantified the dispersion of electromagnetic waves on metal surfaces.

Attenuated total reflection (ATR) coupling method using a glass prism was developed by Otto in 1968 to couple electromagnetic radiation of light waves to surface plasma [48]. The Otto configuration had a gap between the metal surface and base of the glass prism, making it suitable for use in cases where the metal surface was not to be touched

like the study of single-crystal surfaces. But maintenance of gap between glass and prism layer was a great limitation. later this limitation was modified by Kretschmann et al. and proposed a configuration having contact between the glass prism base and became famous for the bulk excitation of surface plasmons [49]. Until late 1970, the potential of SPR for characterizing thin films and monitoring processes at metal interfaces was realized. SPR for the biosensing and the detection of gas was demonstrated by Liedberg and Nylander in 1982 [50]. After that milestone work, academic researchers and the scientific community had shown interest. Since then, there has been an explosion in the development of SPR sensing techniques, configuration, and devices for detecting and measuring biological and chemical substances [51].

For the performance analysis of above mentioned research works, mode guiding property of the PCFs is needed. Considering the mode solving property several well-known methods are available such as plane wave expansion method, multipole method, eigenmode expansion method and finite element method (FEM).

## **2.2 Optical Sensor**

Nowadays, optical sensing can be classified in different manners based on configuration, working principle, and detection purpose [37]. Based on operating principle, the sensor can be classified as a) wavelength modulated, b) phase-modulated, c) intensity-modulated, and d) polarization modulated. Again, classification based on the configuration includes a) SPR, b) interferometer, c) optical ring resonator, and d) photonic crystal-based sensor. Detection purposes may include physical, chemical, and biosensors for detecting temperature, strain, pressure, pH, gas, DNA, glucose, blood flow, etc.

## **2.3 Optical Biosensor Principles**

For detecting biological and chemical species, optical sensing can be classified mainly into three categories: interferometry, luminescence and SPR. Refractive index (RI) sensor techniques such as interferometry and surface plasmon resonance are based on pure change in the modes phase. On the other hand, absorption sensor techniques such as luminescence quenching are based on pure changes in attenuation [52].

## 2.4 Interferometry

This optical sensing technique involves splitting a source light wave into two waves and interfering with one another after each light wave has traversed its designated path. One wave is made to propagate along a way that goes through the sample (sensing path) while the other crosses a different route with no sample (reference path). The dielectric

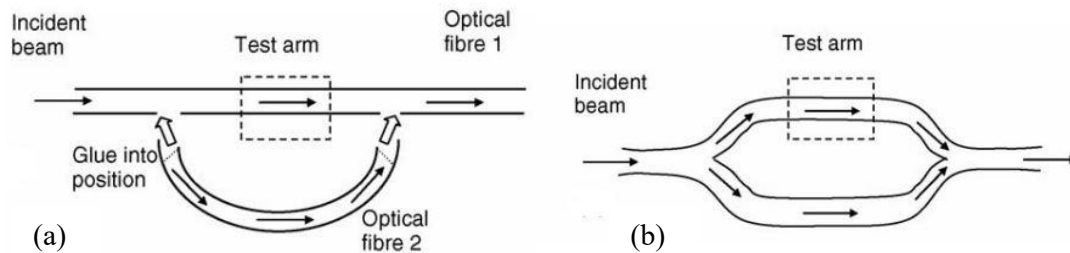


Figure 2.1: Interferometry a) Fiber optic version and b) Integrated optic version, adapted from Ref [39].

constant,  $\epsilon$  is a characteristic quantity of the sample and  $\epsilon$  of the sensing path and the reference path alter due to the molecular interactions. For an infinite homogeneous medium, the phase velocity,  $v$  is given by

$$v^2 = \left(\frac{\omega}{\beta}\right)^2 = \frac{1}{\mu\epsilon}, \quad (2.1)$$

where  $\mu$  represents the magnetic permeability and  $\beta$  and  $\omega$  for propagation constant and angular frequency respectively. A change in  $\epsilon$  alters the phase velocities of the light wave propagating through it. Thus at the output, changes in the sample can be reliably detected when the two light waves recombine constructively (both light waves are in phase) or destructively (both light waves are out of phase), resulting in high or low output power levels at the output respectively.

## 2.5 Luminescence

Luminescence is another kind of optical sensing technique. It employs light emitting probe molecules known as fluorophores or luminophores. The lifetime or intensity variation of the fluorophores is detected and used for sensing purposes [53]. The EF is used to excite the sensor particles and for improving sensitivities, particles may be forced to emit their radiation in guided modes [54]. The loss of light is much more critical due to the scattering nature than RI based methods and a low amount of light reaches the detector. So, the propagation losses must be minimized for guiding beams using high quality optics.

## 2.6 Fundamental of SPR

When the numbers of free electrons and positive ions on a conductor (or metal) are equal, the total charge density of a conductor (or metal) is zero. Any external field in the conductor creates the tendency of electrons moving towards the positive ion and vice versa. A longitudinal oscillation introduces due to such continuous transportation of charge in the conductor (known as surface plasmon (SP)) [55]. The oscillation of the SP is shown in Figure 2.2 and it is normally supported by the metal and dielectric interface. An electromagnetic (EM) wave is formed by the collective oscillation of electrons that is known as SPW. Only TM-polarized (*P*-polarized) light can excite SP in

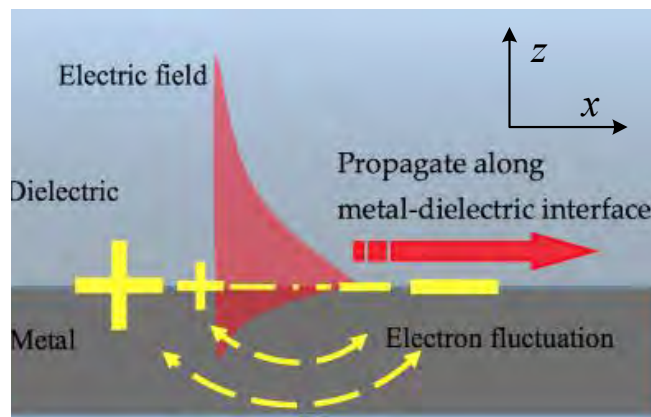


Figure 2.2: The propagation of SPW wave at metal and dielectric interface, adapted from Ref [38]

which the magnetic field vector is parallel to the plane of interface and perpendicular to the direction of the SPW. Therefore, SPW is characterized by the propagation constant as [51]

$$\beta = \frac{\omega}{c} \sqrt{\frac{\epsilon_{co} \times \epsilon_{di}}{\epsilon_{co} + \epsilon_{di}}}, \quad (2.2)$$

where  $c$  represents the velocity of light in free space and the dielectric permittivity of the conductor (metal) and dielectric medium are  $\epsilon_{co}$  and  $\epsilon_{di}$ , respectively. From Eqn. 2.2, property SPW depends on the property of the dielectric and metal medium, and the excitation of the electrons in the conductor is required to create the SP oscillation. So, the EM field is imposed on the surface from the light source, and an optical tunable source is used in this case. The electrical permittivity for the dielectric is positive and negative for the conductor. For the dielectric medium, Eqn. 2.2 can be rewritten considering the propagation constant (maximum) as [56]

$$\beta = \frac{\omega}{c} \sqrt{\epsilon_S}, \quad (2.3)$$

where  $\epsilon_S$  is the dielectric permittivity of the sensing medium. The propagation constant for SPW is higher than the propagation constant of light in the dielectric medium. SP requires the light with extra momentum or energy because it can't be excited with the normal light having the same polarization state as the SPW. Moreover, the propagation constant of the SPW and light source should be matched to another.

## 2.7 Conventional SPR Mechanism

Eqn. 2.3 shows a direct relationship with the dielectric constant of the medium at which rate the light wave propagates through a dielectric medium at a given frequency. An incident light beam or the bombardment of electrons can be required to excite the SP for a resonant pattern and the momentum of the incoming beam should match with the plasmons. When the propagation constants of the SP and incident light energy match to one another by both magnitude and polarization, SPWs are induced. It can be achieved by the following conventional methods

1. A prism coupler
2. A grating coupler and
3. Fiber optic waveguide coupling.

### 2.7.1 Prism Coupler

Figure 2.3 (a) shows the prism-based coupling configuration, and it experiences TIR at prism-metal layer boundary when the light wave passes through a high RI prism and the EW generated at the prism-metal interface propagates along with the metal layer. The propagation constant of the generated EW can be equal to the SPW so that both waves propagate along the metal-dielectric boundary [50]. The characteristics of both waves are so similar that they may interact with one another. Adjustment of the propagation constant is made by adjusting the angle of incidence. Mathematically;

$$\beta_e = \frac{\omega}{c} \sqrt{\epsilon_p} \times \sin(\theta), \quad (2.4)$$

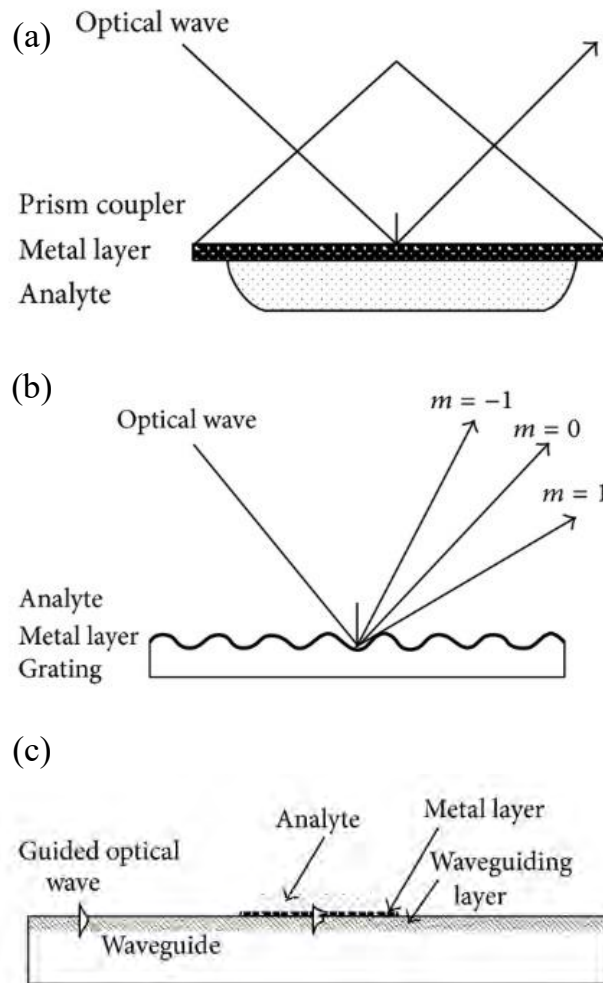


Figure 2.3: Commonly used coupling mechanism a) Prism coupler, b) Grating coupler, and c) Optical wave-guide based SPR, adapted from Ref [9].

where  $\theta$  means the angle of incident light with the prism,  $\epsilon_p$  is the prism dielectric constant and  $\beta_e$  represents the propagation constant of the evanescent field. This method is known as attenuated total reflection (ATR). Based on this coupling mechanism, the Otto configuration and the Kretschmann configurations are developed for the sensing purpose.

### 2.7.1.1 Otto Configuration

Otto et al. reported ATR in 1968 that suggested a coupling method that involves the coupling of SPWs to an EW generated as a result of incident light undergoing based on the incident angle of the light [57]. The incident angle of the light must be greater than the critical angle,  $\theta_{(ATR)}$ . The main differentiating characteristic of this configuration shown in Figure 2.4 is the air gap sandwiched between the metal-dielectric layer. Gen-

erated EF propagates along with the air-dielectric interface, and then it excites a SPW which propagates along with the metal-air interface. The width of the air gap is 200 nm, and the challenge is to realize the air gap practically. Some advances in single crystal metal surface research helped reduce the limitation of this configuration.

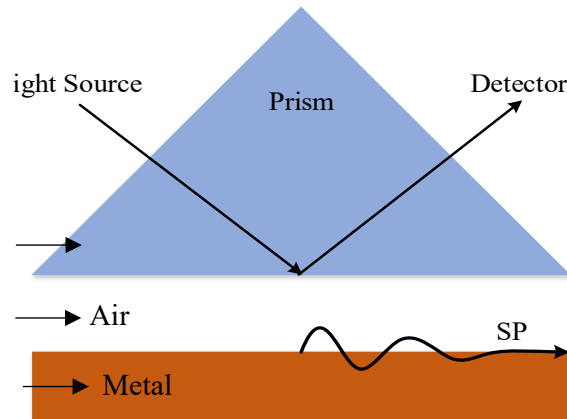


Figure 2.4: Otto coupling mechanism, adapted from Ref [44].

### 2.7.1.2 Kretschmann Configuration

Kretschmann configuration shown in 2.5 improves the limitations of Otto's configuration, and that's why it is very similar to the Otto configuration [58]. Kretschmann and Reather figured that if the metal layer was made thin enough (50 nm) and the prism was in direct contact with the metal, the EF could radiate through the thin metal. This radiated field excites SPWs and propagates along with the dielectric-metal interface. However, the excitation of SPW has a different approach and excitation of SPWs occurs only when the propagation constants of both EF and SPWs match at a particular incidence angle.

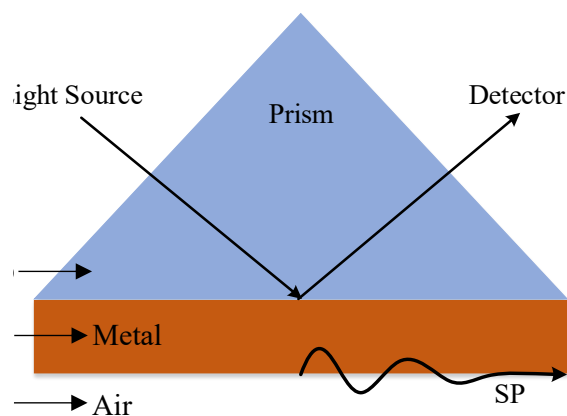


Figure 2.5: Kretschmann coupling Configuration, adapted from Ref [44].

## 2.7.2 Grating Coupler

As shown in Figure 2.3 (b), gratings on a metal surface can alternatively excite SPW. The incident light impinges on the gratings and is detracted into multiple paths by the irregular nature of the gratings. However, if any of the wave vectors of the diffracted light is parallel to the surface grating and its propagation constants is similar then the excitation of SPW occurs [59]. The incident light on the grating directly illuminates the surface of the metal, thus requiring the sample dielectric to be optically transparent to enable light to pass through it [60]. The reverse of using SPWs to generate light using the grating coupler is possible.

## 2.7.3 Fiber Based SPR Configuration

Figure 2.6 shows fiber based SPR sensing configuration, and it is more advantageous than prism-coupling SPR sensors. It is capable of remote sensing having a small size with design liberty [37]. The light guiding mechanism of fiber based SPR is similar to the prism-coupling SPR sensing and TIR mechanism guides the light through the fiber. The conventional core of prism coupling SPR configuration is replaced by the fiber. For sensing through SPR configuration, a coated metal layer with dielectric sensing is deposited in the place of a certain portion of the cladding. Light source is used at one end of the fiber and using TIR mechanism light propagates through the core of the fiber. When the light strikes on the metal surface, EF is generated and this field creates SPWs in core-metal interface.

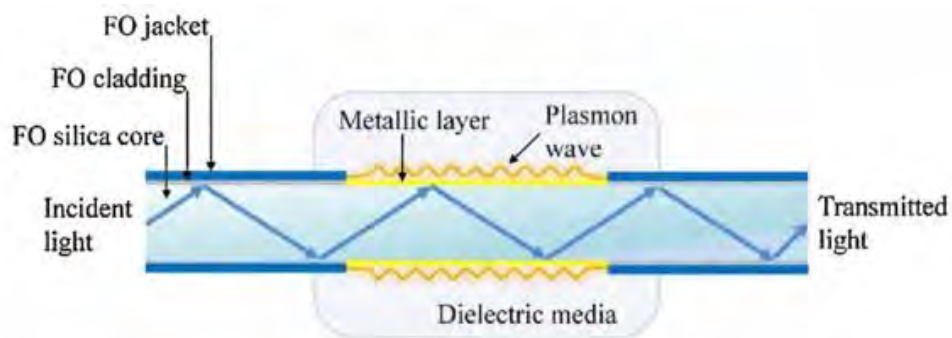


Figure 2.6: Fiber based SPR Configuration adapted from Ref [44].

## 2.8 PCF

Photonic crystal (PhC) is composed of a periodic dielectric, metallic dielectric or even superconductor and it is inhomogeneous in nature. It has a periodic structure and the



dielectric property of this material varies periodically with respect to the corresponding wavelength of the light. When a light source embeds this crystal, it can localize the light and the spontaneous emission of atoms occur [61]. The most amazing property of this crystal is the periodic reflection which occurs at the borders of alternating dielectric material. The motion of the photon is affected in the similar manner as the motion of the electrons in solids is affected by ionic lattice. As a result, the propagation of electromagnetic waves is allowed and forbidden in certain energy bands as the electrons mentioned before. The light can pass in a certain frequency band for the proposed structure with a certain angle and can't propagate at some other depending on the wavelength. The wavelength that can pass is known as modes and other disallowed wavelengths are known as photonic bandgap (PBG) - this phenomenon results in spontaneous emission of photons. Schrodinger equation expresses the behavior of electronic crystal and the behavior of PhC is given by the wave (two Maxwell's curl) equation.

$$\frac{\delta^2 E_x(z)}{\delta z^2} - \left(\frac{\omega}{c}\right)^2 \epsilon(z) E_x(z) = 0, \quad (2.5)$$

where  $E_x(z)$  is propagating electric field in  $z$  direction and the dielectric constant of the medium is represented by  $\epsilon(z)$ .

Using the excellent properties of PhC, a special class of fiber is made which is known as PCF that can confine light and this confinement characteristics is not possible for normal fiber. There are many types of PCF for example

- a) PBG (Photonic bandgap fiber) — Uses the bandgap effect to confine light
- b) Holey fiber — Introducing air holes in the cross section of the fiber
- c) Hole assisted fiber — Higher index core modified by the presence of the air hole in the core
- d) Bragg fiber — Concentric ring of multi-layer film is used to form PBF and
- e) MOF (Microstructured optical fiber) — Light guided not by the difference of RI but by the modification of the structure

Nowadays, PCFs are being used in many applications, such as biosensors, chemical sensors, optical sensors, solar cells, pressure sensors, dispersion compensators, laser, nonlinear signal processing, and others.

## 2.9 PCF Based SPR Sensing

PCF consists of core and cladding layers having air holes in a periodic order in the cladding and/or core region. The propagation characteristics of the PCF can be controlled by the arrangement of the air holes. The guiding property of the PCF can be governed by the variation of the total number of rings and by varying the dimension of the air holes. Different conventional RI sensing approaches include prism coupling, modal interferometer, fiber Bragg grating, slot waveguide, and long-period fiber grating. However, they make the devices bulky and lower sensitivity is a great limitation including other restrictions and difficulties reported by Tien et al. [40]. On the contrary, PCF based SPR technique builds up an accurate policy to control the propagation nature of light and EFs in place of conventional fibers or prism [41]. It is more advantageous than the conventional one because it has greater design flexibility, low sample requirements, and miniaturization amenities [19,20]. The most appealing characteristic of PCF based SPR technique is the endless single-mode behavior which is independent of the used materials. It provides excellent performance and an excellent opportunity for versatility [18,20]. The shape of the PCFs can be circular, hexagonal, decagonal, octagonal, non-hexagonal, hybrid and the change of the geometry can be made easily to uplift the guiding properties and sensing performance [18,19,23,27,39]. The PCF-SPR

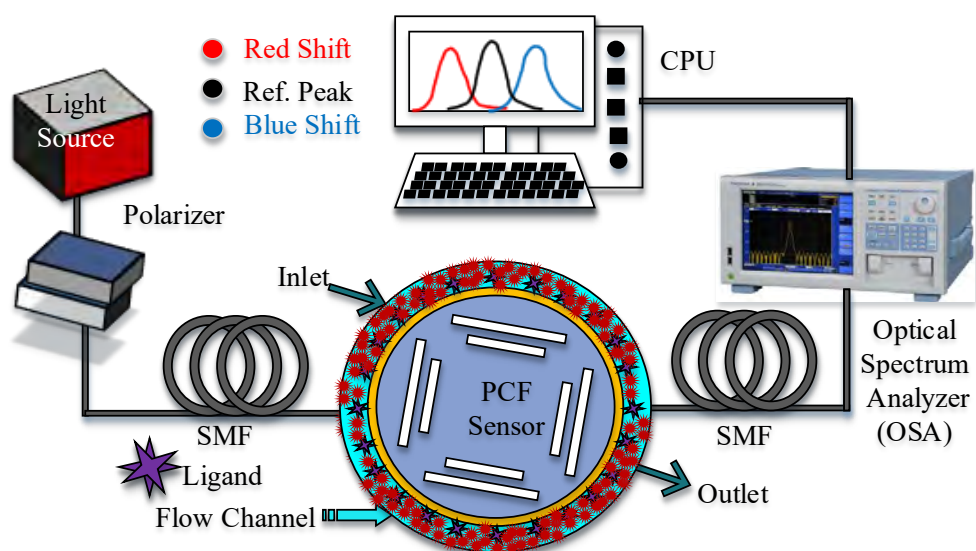


Figure 2.7: Basic graphical setup of practical sensing using a proposed sensor with sample output response

sensor works based on the EF created by the propagation of light and its penetration into the cladding region. Optimization can be made in the PCFs' geometrical structure for an optimum EF, and light propagation in the leaky core guided mode can be controlled

and improved. The proper selection of core-cladding diameter can launch light light at zero incident angle and control the light propagation in single mode. Again, it not only increases the sensitivity of the sensor but also provides a sharp resonance peak. The sharp resonance peak aids with a lower full width half maximum (FWHM) and gives higher detection accuracy (DA).

For achieving the single mode operation of light, optimization can be introduced in core-cladding position, fiber diameter, number of air-holes, air-hole diameter, and PM layers' thickness [62]. This EF will strike the metal surface and produce a massive number of free electrons that interact on the surface of PM. Electrons start to resonate when the frequencies of the free electrons of the PM's surface and EF are equal. It results in a SPW propagating through the metal and dielectric interface. When both frequencies are matched, this unique phenomenon is called as resonance condition, which creates a high loss peak of the narrow band. At the resonant state, the real part of the effective mode index ( $n_{eff}$ ) of surface plasmon polariton (SPP) mode and core mode overlap each other [18, 39]. In this resonance wavelength, the sensor provides the highest sensing performance for a PM of specific RI. Resonance wavelength of the phase matching condition changes with the variation of the analyte's RI. With the variation of the sample or analyte's RI, the corresponding wavelength for the phase matching condition can be measured. By observing the loss peak variation with RI variation, the unknown sample could be detected. A simple block diagram for applying RI for different analytes by the proposed sensor is shown in figure 2.7 with sample input and output. Light source (optical tunable) emits light followed by a polarizer and propagates through a single mode fiber (SMF). Using splicing technology, SMF is coupled with the proposed sensor and aids in propagating the emitted signal from the optical source. Using a pump, liquid analytes enter into and exit from the analyte channel placed in between the PML and gold layer. Another SMF is connected with the sensor using splicing that helps the optical spectrum analyzer (OSA) measure the transmitted signal coming from the sensor. Finally, after processing the output, the peak shifting of the output signal can be observed and analyzed through a central processing unit. Here, the solid green line represents the reference signal, and red and blue dotted lines show the resonance point shifting to shorter and longer wavelengths, respectively.

## 2.10 Interrogation of Surface Plasmon Waves

SPR manifests itself when SPW couples with the EW (generated for the incident light wave), inducing a resonant energy transfer from the EW to the SPW. Consequently, the strong concentration of the SPW in the dielectric makes it very sensitive to changes in

the optical properties of the dielectric [51]. This interaction between the SPR and the incident light wave alters the properties of the light, such as amplitude, spectral distribution, polarization, and phase. Variations in these features can be correlated through changes in the propagation constant of the SPW [51]. Therefore, induced changes in the RI at the surface of the metal, consequently changes the propagation constant of the SPW and corresponding changes in RI can be determined by measuring changes in those light wave characteristics [63]. The following detection modes are commonly used of the optical wave at resonance;

- a) Amplitude / Intensity interrogation [64]
- b) Wave Length / Spectral Interrogation [65]
- c) Phase interrogation [66]
- d) Angular interrogation [67]
- e) Polarization interrogation [68]

### **2.10.1 Amplitude Interrogation**

This interrogation method involves measuring the change in intensity of the light wave after its interaction with the SPW at a fixed wavelength and angle of incidence. The coupling of the EW to the SPW transfers energy resonantly to the SPW, consequently registering a change in light wave intensity. The largest difference in light intensity indicates the wavelength and angle at which the most robust coupling occurred.

### **2.10.2 Wavelength Interrogation**

This interrogation approach employs a fixed angle of incident light while varying its wavelength to finally determine the wavelength yielding the strongest coupling of the component of the light wave vector parallel to the metal surface propagating at the same rate as the SPW. The wavelength at which the strongest coupling occurs would register the highest loss or the lowest reflectivity as the resonant transfer of light energy from the EW to the SPW.

### **2.10.3 Phase Interrogation**

This interrogation method involves measuring the shift in phase of the light wave after interacting with the SPW at a fixed wavelength and angle of incidence. The coupling of the evanescent wave to the SPW transfers energy resonantly to the SPW, consequently

registering a change in the light wave phase. The most significant phase shift indicates the wavelength and angle at which the strongest coupling occurred [66].

#### **2.10.4 Angular Interrogation**

This form of interrogation provides a way to determine the component of the light wave vector parallel to the metal surface, which excites the SPW. The coupling strength of the SPW to the EW is measured at a constant wavelength while varying the angle on incident light wave until an angle yielding the strongest coupling. A peak indicates the strongest coupling in the reflectivity or attenuation (loss) spectrum plots.

#### **2.10.5 Polarization Interrogation**

This interrogation method involves measuring the change in the polarization of the light wave after its interaction with the SPW at a fixed wavelength and angle of incidence [63]. The coupling of the EW to the SPW transfers energy resonantly to the SPW, consequently registering a change in light wave polarization. The most significant change in light polarization indicates the wavelength and angle at which the strongest coupling occurred.

### **2.11 SPR in Biosensing**

Mentioning that a more significant portion of the SPW field is concentrated in the dielectric, the changes in the RI of the dielectric habitually changes the propagation constant of the SPW. This relationship between RI and SPW propagation constant is the underlying operating principle of SPR biosensors. The biosensing process involves the capture of analytes contained in the liquid sample by biomolecular recognition elements (antigens) immobilized on the metal surface that target the analytes. The binding of antigens and analytes causes a localized increase in the RI of the sample close to the metal surface, consequently increasing the propagation constant of the SPW propagating along the metal surface (Figure 2.8). This change in the propagation constant of the SPW can be accurately measured by optical means. Changes in the magnitude of the propagation constant of the SPW depend on both the degree of penetration of the magnetic profile of the SPW and the volume of change in the RI of the sample resulting from bio-molecular binding events. The binding induced change in the propagation constant of the SPW is proportional to the RI change and the depth of the area within which the change occurs.

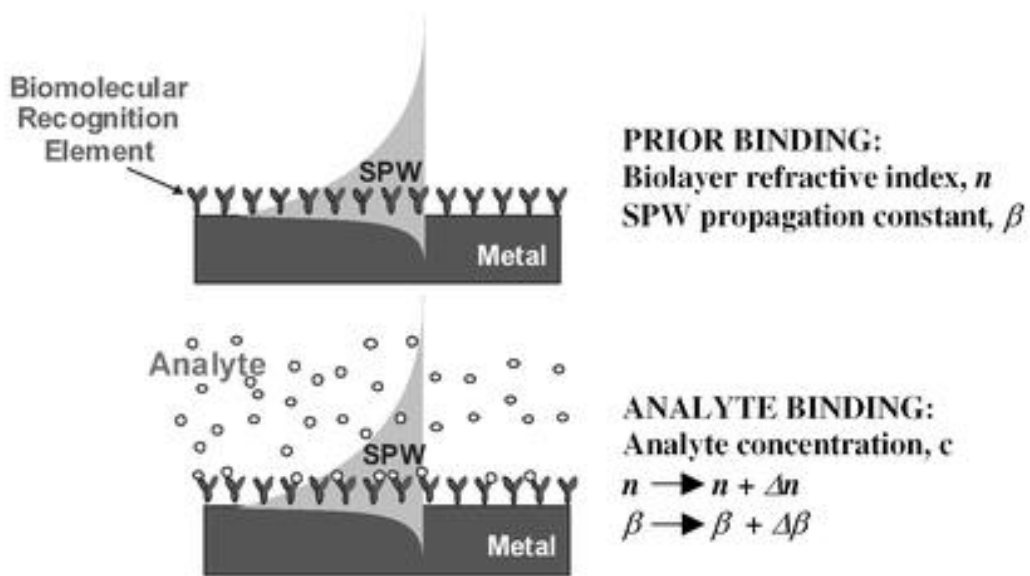


Figure 2.8: Biosensing using the SPR principle adapted from Ref [50]

## 2.12 Numerical Methods

A lot of numerical works have already been carried out for the PCFs simulation such as plane wave expansion method, multi pole method, eigen mode expansion method and FEM. To investigate the PCFs properties, several numerical methods are available. The accuracy of these numerical methods is depending on some basic properties as a) Full vector formulation b) Direct insertion c) CL measurement d) Capacity to calculate the arbitrary cross-section and e) Symmetry exploitation. Considering this above mentioned properties, FEM is chosen as a mode solver for our proposed biosensor.

### 2.12.1 FEM

The finite element method (FEM) is a mathematical tool which is able to find the approximate solution of partial differential equations (PDEs) for complex structures with boundary conditions. Here it is used to investigate the propagation characteristics of light to get the resonance modes in the fiber [37]. FEM allows the solution of a large class of partial differential equations without any limitation by geometry. The main advantage of this method is that it divides the large computational area into small triangular or rectangular area. For fibers, the use of triangular sub-spaces provides a good approximation for its circular nature [69]. It allows to change the air fill fraction. Considering the unique structures of PCFs, a full vector FEM formulation would be required to study wave propagation of light through fibers. It is able to calculate the real and complex effective index of the structure that describe the propagation behavior and gives an approximate dispersion relation of the PCF.

Full vectorial FEM incorporates anisotropic perfectly matches layers (PML), enabling one to solve for as many modes as desired in a single run without iteration [70]. Analysis of leaky modes is also possible with PMLs. Both loss and dispersion properties are determined in a single execution. In the case of propagation mode computation, FEM creates a matrix that numerically approximates the partial differential operator of the problem transforming it into a numerical eigenvalue problem. Then the problem is solved using numerical algebra techniques. The FEM method involves four basic steps through which a physical problem is solved:

1. To generate mesh for device geometry into a finite number of elements,
2. To derive the governing PDEs for each typical element,
3. To generate the system PDEs Assembling of all elements of the device and
4. To solve the system PDEs for determining the unknowns.

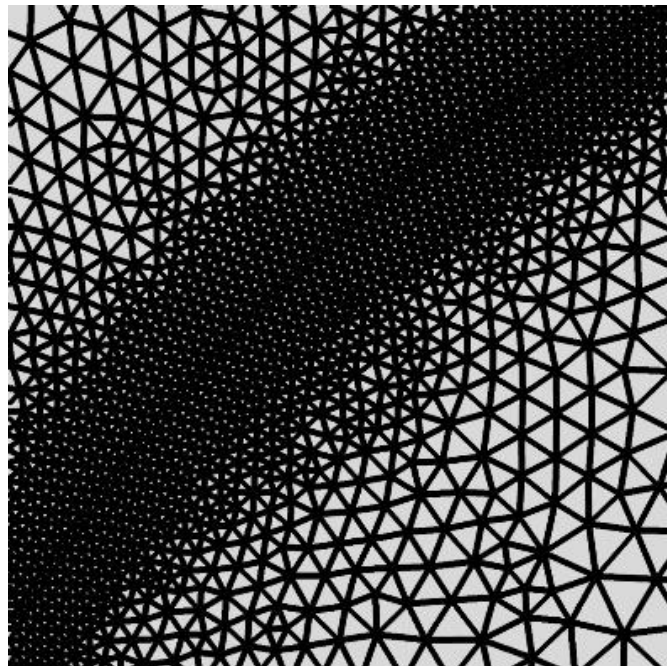


Figure 2.9: Finite element method.

### 2.12.2 Formation of FEM

FEM allows dividing the cross section of PCF in the transverse  $x$ - $y$  plane into triangular or rectangular elements with efficient irregularities. Element's size, shape, and RIs can be different and it can describe the medium characteristics accurately as well as the PCF structure including air-holes. For the proper study of hybrid mode and polarization-dependent wave propagation, a full vectorial analysis is required. Consider an optical

waveguide having an arbitrary cross-section in the transverse  $x$ - $y$  plane and it has an available full vectorial wave equation which is derived from Maxwell's equations in the form of

$$\nabla \times ([p] \times \phi) - k_0^2 [q] \phi = 0, \quad (2.6)$$

where  $[p]$  and  $[q]$  represents the permeability tensors and  $\phi$  represents the magnetic field,  $H$  or the electric field  $E$ .  $[p]$  and  $[q]$  can be written alternatively as

$$[p] = \begin{bmatrix} p_x & 0 & 0 \\ 0 & p_y & 0 \\ 0 & 0 & p_z \end{bmatrix} \quad \text{and} \quad [q] = \begin{bmatrix} q_x & 0 & 0 \\ 0 & q_y & 0 \\ 0 & 0 & q_z \end{bmatrix}$$

The component of  $[p]$  and  $[q]$  are given in table 2.1 and  $n_x$ ,  $n_y$  and  $n_z$  represent the RIs in  $x$ ,  $y$  and  $z$  plane.

Table 2.1: Component of permeability tensor  $[p]$  and  $[q]$ .

Parameter	$\phi$	$p_x$	$p_y$	$p_x$	$q_x$	$q_y$	$q_x$
Magnetic field	$H$	$1/n_x^2$	$1/n_y^2$	$1/n_z^2$	1	1	1
Electric field	$E$	1	1	1	$n_x^2$	$n_y^2$	$n_z^2$

## 2.13 Optical Tunable Source

For the study of spectroscopy especially wavelength-induced chemical and/or biological property or wavelength-dependent physical changes of materials, tunable light source is a perfect choice. It provides a great versatility as both a high resolution and broadband monochromatic light source. It is popular for measurement applications for its spectral responsivity and quantum efficiency with the degree of capability and these are the main parameters for translating the performance of a system. Normally Xenon, Mercury-Xenon arc lamps are used as a tunable light. It consists of two electrodes (one anode and one cathode) having gas like Xenon, Argon, Neon or Mercury in between the electrode and ionization of the gas generates light.

## 2.14 Optical Spectrum Analyzer

Spectrum analyzer is used to measure the power spectrum of known and unknown signals, and basically, it measures the magnitude of the input signal concerning the frequency of that signal. Most of the measured input signals are electrical, and the appropriate transducer is applied if the input signal is a light wave or an acoustic wave. An



optical spectrum analyzer (OSA) is used to measure the spectrum of the optical signal directly without the help of any transducer. It can quickly determine the bandwidth, harmonics, frequency, distortion, power, and other spectral components. Again, it can be plugged into AC power. It uses very low power, and battery power can operate it. So, it is portable also with optional power and a very lightweight device. The display of the OSA is viewable, and it transfers data efficiently from the analyzed network. Also, it can synchronize the data from a network.

## 2.15 Refractive index of some analytes

After designing and investing the performance a biosensor, it is very important to find out which samples we detect using biosensor. For this reason, it is also important to know the RI of different analytes as well as output of our proposed sensor for each analyte. Here, the RI of some analytes is given in table 2.2 within the range that our proposed sensor can detect.

Table 2.2: Refractive Index of different analytes within 1.29 to 1.43.

SL. No.	Analyte name	Refractive Index
1.	Water ice	1.31
2.	TFE/PDD (Teflon AF)	1.315
3.	Water	1.333
4.	Cryolite	1.338
5.	Propene	1.34
6.	Polytetrafluoroethylene (Teflon)	1.35–1.38
7.	Sugar solution, 25%	1.3723
8.	Sugar solution, 50%	1.4200
9.	Cornea (human)	1.373/1.380/1.401
10.	Kerosene	1.39
11.	10% glucose solution in water	1.3477
12.	20% glucose solution in water	1.3635
13.	Silicone oil (nD <sup>25</sup> )	1.393–1.403
14.	Acetone (propanone)	1.36
15.	Ethanol (ethyl alcohol)	1.361
16.	Milk, Ether	1.35
17.	Acetic Acid	1.37
18.	Octane	1.40
19.	Heptane	1.38

## **2.16 Summary**

This chapter summarizes the basics of an optical sensor with its principle, fundamental and excitation of SPR including Otto, Kretschmann, grating coupler and fiber-based PCF configuration, fundamentals of PCF and PCF based SPR sensing, different interrogation method of SPW, a brief description of FEM and implementation of SPR in bio-sensing with a literature review of previous works. The subsequent chapters will fulfill the objectives mentioned in the objection section of the introduction chapter.

# Chapter 3

## Modeling and Performance Parameters

### 3.1 Introduction

Nowadays, sensors are being miniaturized due to the high demand for lightweight, small size, portable, compact structure, highly efficient, real-time, and cost-effective devices for sensing application [4, 5]. PCF fulfills the above-mentioned demand providing an excellent guiding property and design freedom. SPR offers a highly sensitive, efficient, label-free, and real-time sensing technique [4]. So, researchers combine PCF with SPR for perfect detection and apply it for different sensing applications, including organic chemical sensing, gas sensing, cancer cell detection, alcohol sensing, bio-imaging, food poisoning detection, communication devices, material science, and medicine [3–8], etc. Design optimization and proper plasmonic material are crucial for getting adequate output. This chapter will discuss the design procedure of our proposed sensor and the theoretical study of performance measuring parameters.

### 3.2 Design with Theoretical Modeling

PCF sensors can be designed in circular, semicircular, D, double D, H, hexagonal, octagonal shape, and different hybrid models. Here, we have proposed a slotted PCF biosensor based on the SPR technique, and the performance of the sensor is uncovered and evaluated numerically through the FEM. The main aim of our work is to maximize the sensitivity of the biosensor with the most simplified and realistic design, lessening the fabrication complexities and cost. This work has replaced the symmetric air-hole with an asymmetric one and reduced the total number of air holes without sacrificing

performance. After completing the PCF design, the performance measurement parameters greatly depend on the suitable selection of PM. This section will cover the fields mentioned earlier.

### 3.2.1 Design Approach

Figure 3.1 shows the cross-sectional view of the proposed slotted PCF based SPR biosensor in an  $x$ - $y$  plane with two layers of rectangular air holes in a normal approach. In this raised model, a PML is used as a boundary radiation absorber to investigate the light propagation characteristics of the sensor with the help of FEM. The fused silica is chosen as background material and the Sellmeier dispersion equation is used in the simulation process to represent it. The air holes are placed at an equal distance from the center and if the height of the air holes is increased equally, they will touch one with another forming a square at the center of the fiber.

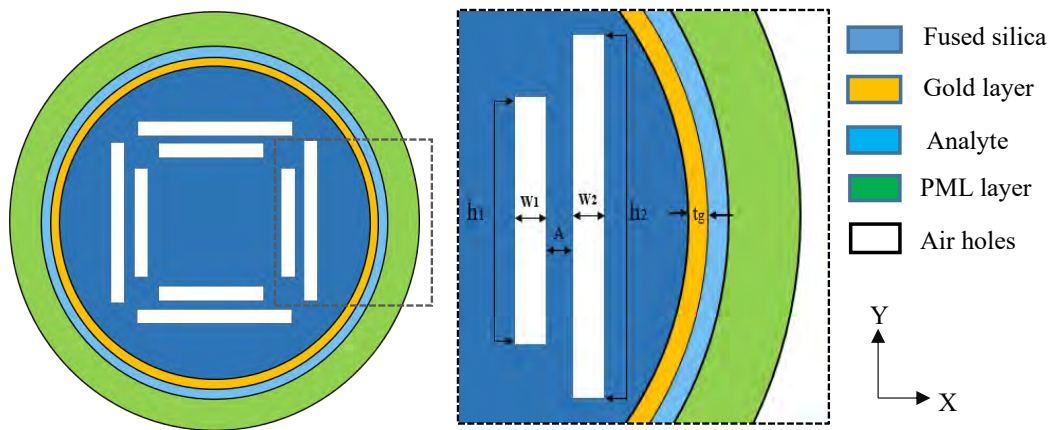


Figure 3.1: A cross-section view of the proposed sensor's geometrical structure with the air holes' normal approach.

The distance between the center of the fibers to any 1<sup>st</sup> layer air hole center is 2.5  $\mu\text{m}$ , and the center-to-center distance between two air holes in the opposite direction is 5  $\mu\text{m}$ . The center-to-center distance between two adjacent air holes is called the pitch distance ( $\Lambda$ ), and  $\Lambda$  is picked as 1  $\mu\text{m}$  as an optimized value. The square lattice structure helps to increase the overall sensitivity by coupling energy between the plasmonic and core mode [18]. So, it is chosen because it also helps to increase the area between the circular gold ring and the core. The air holes remaining at the 2<sup>nd</sup> layer are positioned at a center-to-center distance of 4  $\mu\text{m}$  from the circle's center. The radius of the circle containing the gold layer is 5.03  $\mu\text{m}$ , and the distance from the center of any air-hole of the 2<sup>nd</sup> layer is 1.03  $\mu\text{m}$ . The optimized thickness of the gold layer is 0.03  $\mu\text{m}$  with an inner radius of 5.00  $\mu\text{m}$  from the center of the fiber. The thickness of the analyte layer

Table 3.1: Optimized Parameters Used in Normal Approach of the Proposed Structure.

<b>RI</b>	<b><math>\lambda</math> (<math>\mu\text{m}</math>)</b>	<b><math>\Lambda</math> (<math>\mu\text{m}</math>)</b>	<b><math>h_1</math> (<math>\mu\text{m}</math>)</b>	<b><math>h_2</math> (<math>\mu\text{m}</math>)</b>	<b><math>w_1</math> (<math>\mu\text{m}</math>)</b>	<b><math>w_2</math> (<math>\mu\text{m}</math>)</b>	<b><math>t_g</math> (nm)</b>
1.33	0.570	1	2.50	4.25	0.50	0.50	30

is 1.2  $\mu\text{m}$ , and the PML layer is used outside of the analyte layer to avoid boundary radiation problems. All the parameters used to develop the structure of the proposed sensor are precisely in Table 3.1. The proposed structure firstly shows an optimization for an analyte of RI 1.33 and the optimized wavelength is 0.57  $\mu\text{m}$ . Again, the cross-

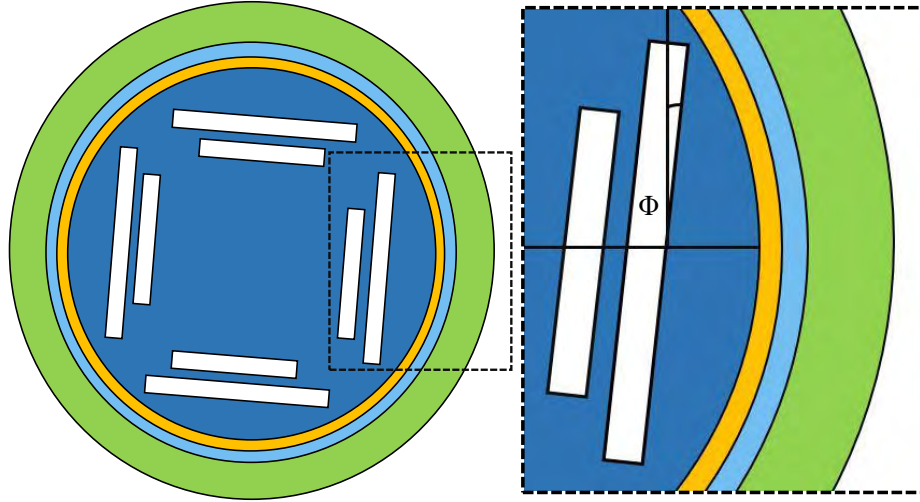


Figure 3.2: Cross-sectional view of the geometrical structure of the proposed sensor with the inclined approach of the air holes.

Table 3.2: Optimized Parameters Used in Inclined Approach of the Proposed Structure.

<b>RI</b>	<b><math>\lambda</math> (<math>\mu\text{m}</math>)</b>	<b><math>\Lambda</math> (<math>\mu\text{m}</math>)</b>	<b><math>h_1</math> (<math>\mu\text{m}</math>)</b>	<b><math>h_2</math> (<math>\mu\text{m}</math>)</b>		
	<b><math>w_1</math> (<math>\mu\text{m}</math>)</b>	<b><math>w_2</math> (<math>\mu\text{m}</math>)</b>	<b><math>t_g</math> (nm)</b>	<b><math>\Phi</math> (deg.)</b>	<b><math>t</math> (nm)</b>	
1.33	0.570	1	2.50	4.25		
	0.50	0.50	25	35	05	

sectional view of the geometrical structure of the proposed sensor is shown in figure 3.2 with the angular displacement of the air holes. Angular displacement ( $\Phi$ ) of the air holes from the perpendicular position shown in figure 3.2 is made with an optimized value to make a sufficient path for propagating light efficiently through the metal-dielectric interface. It will help to increase the sensitivity and overall performance of the proposed sensor. The height of the smaller air holes is  $h_1$ , and for larger air holes, it is denoted by  $h_2$ . Similarly, the width of the smaller and larger air holes are  $w_1$  and  $w_2$ , respectively. The path between the air holes facilitates strongly coupling the incident light from the core guided mode to the cladding mode as SPW. The radius of the inner circle is 5.70  $\mu\text{m}$ , and the thickness of the gold film  $t_g$  around a thickness of 25 nm is placed at the top of the  $\text{SiO}_2$ . Other parameters are kept as same as before and shown in table 3.2.

### 3.2.2 Selected Material Properties

We are choosing the proper material that influences the sensing performance and the detection capability of the proposed sensor. For the proposed geometrical structure, fused silica (SiO<sub>2</sub>) is selected as the background material, and the RI of the SiO<sub>2</sub> is obtained from the Sellmeier equation

$$\eta_{(SiO_2)}^2(\lambda) = 1 + \sum_{i=1}^{i=3} \frac{M_i}{1 - (N_i/\lambda)^2}, \quad (3.1)$$

where the effective RI of SiO<sub>2</sub> is represented by  $\eta_{(SiO_2)}(\lambda)$  and  $\lambda$  = corresponding operating wavelength (μm). Again, Sellmeier's constants are used in Eqn. 3.1 are  $M_1 = 0.696263$ ,  $N_1 = 0.0684043 \mu\text{m}$ ,  $M_2 = 0.4079426$ ,  $N_2 = 0.1162414 \mu\text{m}$ ,  $M_3 = 0.8974794$ , and  $N_3 = 9.896161 \mu\text{m}$ . The variation of RI due to the temperature effect is neglected, and the variation of RI is  $1.28 \times 10^{-5}$  per degree Celsius. So, it is avoided under normal circumstances.

As mentioned before, gold is chosen as the plasmonic material and coated around the outer surface of the sensor. The Drude - Lorentz formula is used to measure the dielectric constant of the gold film, and dispersion is calculated concerning wavelength through this formula [71]

$$\varepsilon_{Au}(\omega) = \varepsilon_\alpha - \frac{\omega_D^2}{\omega(\omega + i\gamma_D)} - \frac{\Delta_\epsilon \Omega_L^2}{(\omega^2 - \Omega_L^2) + i\Gamma_L \omega}, \quad (3.2)$$

here plasma frequency =  $\omega_D$ , angular frequency,  $\omega = \frac{2\pi c}{\lambda}$  with  $c$  = the velocity of light,  $\gamma_D$  = damping coefficient,  $\Delta_\epsilon$  = weight factor (1.09),  $\Omega_L$  = strength of the Lorentz oscillators,  $\Gamma_L$  = spectral width of the Lorentz oscillators and permittivity at high frequency,  $\varepsilon_\alpha = 5.9673$ . Again, the values of the above parameters are:  $\frac{\omega_D}{2\pi} = 2113.6$  THz,  $\frac{\gamma_D}{2\pi} = 15.92$  THz,  $\frac{\Gamma_L}{2\pi} = 104.86$  THz and  $\frac{\Omega_L}{2\pi} = 650.07$  THz.

Again, TiO<sub>2</sub> has a high RI and helps generate a large number of surface electrons. It helps to be attracted to the fields from the core so that interaction with SPP mode is possible. So, it is used as an adhesive layer in between the gold and SiO<sub>2</sub>, and the following equation helps in determining the RI of TiO<sub>2</sub> [72]:

$$\eta_t = \sqrt{A + \frac{B}{\lambda^2 - C}}, \quad (3.3)$$

where  $\eta_t$  represents the RI of TiO<sub>2</sub>,  $A = 5.913$ ,  $B = 2.441$ ,  $C = 0.803$  and  $\lambda$  is in μm.

### 3.2.3 Perfectly Matched Layer

A PML is a non-isotropic absorbing layer that doesn't reflect the outgoing wave from the interior of the computational region. An additional layer is usually added to the structure to decollate a computational region from the surroundings to simulate it in open boundaries using FEM. It helps to absorb the incident wave from a non-PML layer to a PML layer and doesn't reflect at the interface. It is usually used in normalized Euler equation, Helmholtz equation, poroelasticity, and elastodynamics. As part of the model, it is specified to be made of a different absorbing material of varied thickness. This absorbing material must have matched anisotropic permeability and permittivity with the physical medium outside the PML such that there are no reflections. Maxwell's equations can formulate the PML by introducing a complex-valued coordinate transform under the requirement that the wave impedance remains unaffected.

### 3.2.4 Proposed Block Diagram Specimen

The cross-sectional view of the geometrical structure of the proposed sensor is shown in figure 3.3 (a) the angular displacement of the air holes and figure 3.3 (b) to (d) shows step by step development of the proposed sensor with an inclined approach using gold film at the outside of the SiO<sub>2</sub> structure. A simple block diagram for practical sens-

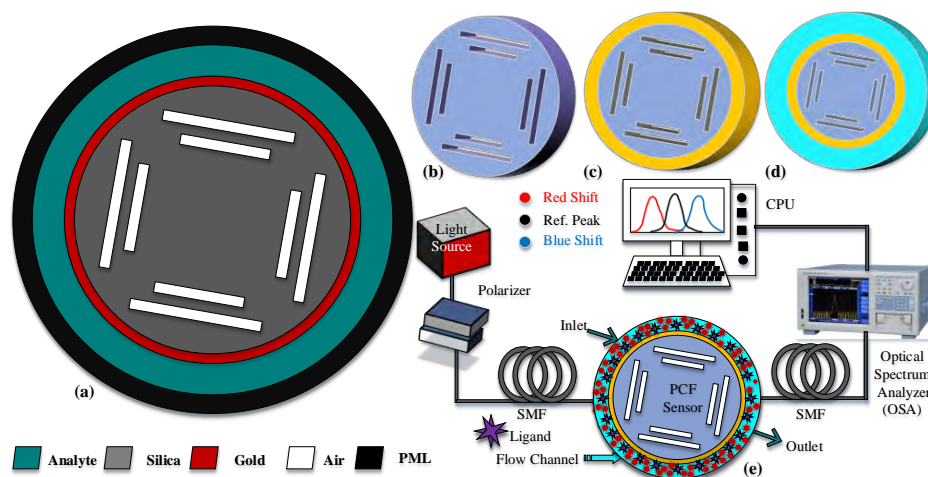


Figure 3.3: (a) Cross-sectional view of the proposed geometrical structure with inclined air holes, (b) to (d) step by step development process, and (e) Block diagram for sensing analytes using the proposed sensor. (CPU: Central Processing Unit; PML: Perfect Matched Layer; PCF: Photonic Crystal Fiber)

ing of RI for different analytes by the proposed sensor is shown in figure 3.3 (e) with sample input and output. Light source (optical tunable) emits light followed by a polarizer and propagates through a single mode fiber (SMF). Using splicing technology,

SMF is coupled with the proposed sensor and aids to propagate the emitted signal from the optical source. Using a pump, liquid analytes enter into and exit from the analyte channel placed in between the PML and gold layer. Another SMF is connected with the sensor using splicing that helps the OSA to measure the transmitted signal coming from the sensor. Finally, after processing the output, the peak shifting of the output signal can be observed and analyzed through a central processing unit. Here, the green solid line represents the reference signal and red and blue dotted lines shows the shifting of resonance point to shorter and longer wavelength respectively.

### 3.3 Numerical Analysis

For this proposed PCF structure, the FEM is used to measure the sensing performance with the help of COMSOL Multiphysics software 5.3a. The following parameters are used to measure the performance of the proposed sensor. Note that the main feature of the sensing performance is WS and AS. Using the wavelength and amplitude interrogation method, the sensitivity of the proposed sensor will be measured.

#### 3.3.1 Confinement Loss

Confinement loss (CL) occurs due to the geometrical structure and the leaky nature of the modes of a PCF. Basically, when we try to put modes in a small place like the core, the modes circulate partly out of the core of the fiber, and this leakage phenomenon creates CL. Based on the number and size of air holes and wavelength, the CL will be structure dependent for a fiber with core and cladding. The variation of the resonance peak of the CL spectrum is used to evaluate the sensing performance of the proposed PCF sensor. The characteristics CL curve varies by the peak value and position of the resonance point for different analytes with separate RI. The CL ( $\alpha_{neff}$ ) is defined by [19]

$$\alpha_{neff} \approx 8.686k_0\text{Im}(\eta_{eff}) \times 10^4 dB/cm, \quad (3.4)$$

where  $\text{Im}(\eta_{eff})$  is the imaginary value of the refractive index,  $k_0 = 2\pi/\lambda$  is the wave number in the free space and  $\lambda$  is the operating wavelength in  $\mu\text{m}$ . For the value of the RI of certain analytes, we have calculated the CL curve by Eqn. (3.4) and it reaches its maximum value at resonance wavelength.



### 3.3.2 Wavelength Sensitivity

In this subsection, the variation of the resonance peak of the CL is measured to determine the variation of RI. Here, through the wavelength interrogation method, sensitivity is calculated for each unit of RI known as refractive index unit (RIU). The variations in RI ( $\Delta n_a$ ) are calculated by detecting the shift of the resonance peak ( $\Delta \lambda_{peak}$ ). Using the wavelength interrogation mode, the WS is denoted as [73]:

$$S_\lambda \left[ \frac{nm}{RIU} \right] = \frac{\Delta \lambda_{peak}(n_a)}{\Delta n_a}, \quad (3.5)$$

where  $\Delta \lambda_{peak}(n_a)$  is the shift of the peak in nm due to the variation of the RIU ( $n_a$ ).

### 3.3.3 Amplitude Sensitivity and Sensor Length

AS is another momentous performance indicating parameter. The transmitted power is observed at a static wavelength in phase matching conditions and the loss of the core depends on the change of the RI and core loss varies very strongly with the variation of the RI,  $\Delta n_a$ . The AS is measured numerically through this equation [73]

$$AS \text{ (RIU}^{-1}\text{)} = -\frac{\Delta \alpha_{loss}}{\Delta n_a} \times L = -\frac{\Delta \alpha_{loss}}{\Delta n_a \alpha_{neff}}, \quad (3.6)$$

$$L = \frac{1}{\alpha_{neff}}, \quad (3.7)$$

where  $\Delta \alpha_{loss}$  and L prevail the loss variation of two consecutive RI and sensor length (SL) respectively.

### 3.3.4 Sensor Resolution

Excluding AS and WS, there is another important parameter that is used to measure the smallest change that can be detected by the sensor. This parameter is named as sensor resolution (SR). The SR of the RI is the capability to measure the smallest fraction of RI precisely and in the case of wavelength, the resolution measures the resonant wavelength peak shift for a certain change in analyte's RI with a minimum spectral resolution. The wavelength resolution can be expressed as [39]

$$R [RIU] = \frac{\Delta n_a \times \Delta \lambda_{min}}{\Delta \lambda_{peak}}, \quad (3.8)$$

here  $\Delta n_a$  = change in analyte's RI,  $\Delta\lambda_{min}$  = minimum spectral resolution, and  $\Delta\lambda_{peak}$  = peak shift of resonant wavelength. In this case, the sensor resolution is calculated for  $\Delta n_a = 0.01$  and  $\Delta\lambda_{min} = 0.1$  nm. So, from Eqn. (3.8), it is explicit that resolution is inversely proportional to the resonance wavelength peak shift. A greater resonance shift indicates that the smallest fraction of RIs can be identified accurately.

### 3.3.5 FOM and Detection limit

Moreover, the figure of merit (FOM) and detection accuracy (DA) are an especial characterization parameters and helps calculate the sensor's performance. Both are directly related to the FWHM of the CL spectrum. FOM and DA are calculated using the following equations [4]

$$FOM = \frac{WS}{FWHM(nm)}, \quad (3.9)$$

$$DA = \frac{1}{FWHM(nm)}, \quad (3.10)$$

where the WS is calculated in nm/RIU, and FWHM is in nm. The lower value of FWHM, and the higher value of WS lessen the probability of false detection. So higher FOM indicates better DA indirectly.

## 3.4 Fabrication Feasibility Study

Various deposition techniques, such as chemical vapor deposition (CVD), modified CVD, and outside vapor deposition (OVD), can be used to deposit gold on the top of the PCF layer. For PCF, the fabrication process may be stack and draw, drilling, extrusion, sol-gel, capillary stacking, and 3D printing technologies [19, 74]. However, most of them are suitable only for circular air holes. Figure 3.3 (a) indicates the cross-sectional view of the geometrical structure of the proposed sensor. Since our proposed model contains asymmetric (rectangular) air-holes, 3D printing fabrication technology, and extrusion are the likeliest techniques and researchers in [38] experimentally designed PCF with asymmetric air holes. Therefore, our proposed PCF SPR sensor is practicable to fabricate and to be used in different applications.

## **3.5 Summary**

This chapter covers the basic design of our proposed sensor with theoretical study of proper PM selection. It gives us an idea of implementing our proposed sensor through the block diagram specimen. Here, we have also studied different parameters to measure the performance of our proposed sensor numerically. The upcoming chapters will fulfill the objectives mentioned in the objection section of the introduction chapter.

# Chapter 4

## Simulation Results and Discussion

### 4.1 Introduction

In this chapter, optimization of structural parameters, performance analysis of different simulations, and comparative performance analysis have been shown with relevant plots. Each design parameter is chosen by a corresponding discussion and a corresponding discussion is given with each result which focuses on the performance that helps to make a conclusion from the simulated data.

### 4.2 Optimization of structural and performance reinforcement parameters

The signal transmission method, sensing principle, and sensing mode of an optical fiber are entirely different from the other sensors, such as an electrical sensor. The sensitivity of a fiber sensor depends on the geometrical design of the sensor, modulation intensity of light, and interaction between the core and SPP mode. The direction of the light is controllable by the position and number of air holes. In this section, the following cases will be considered for measuring the overall performance of the proposed sensor, and it greatly depends on the perfect choice of geometrical parameters. So, choosing an optimized value for each parameter is very important then the overall sensor performance will be analyzed step by step. In this section, the following geometrical parameters will be optimized in a systematic way.

## 4.2.1 Normal Approach of air holes

In this subsection, the effect of gold layer variation, the height of the air holes, and the inclination of the air hole is studied on the performance of the sensor. Then the parameter optimization is made and taken for measuring the overall performance of the proposed sensor.

### 4.2.1.1 Variation of the gold layer thickness

In this sub subsection, the impact of sensing layer (Gold) thickness is studied concerning WS. Figure 4.1 displays the confinement loss as a function of wavelength for different thicknesses of the gold layer ( $t_g$ ). It shows us how the performance of the sensor changes with different value of  $t_g$ . Here,  $t_g = 30$  nm is used as an optimized parameter because maximum confinement loss is obtained at this  $t_g$  for RI = 1.38 given in Table 4.1. The maximum confinement loss is 1.945 dB/cm for RI = 1.38 and  $t_g =$

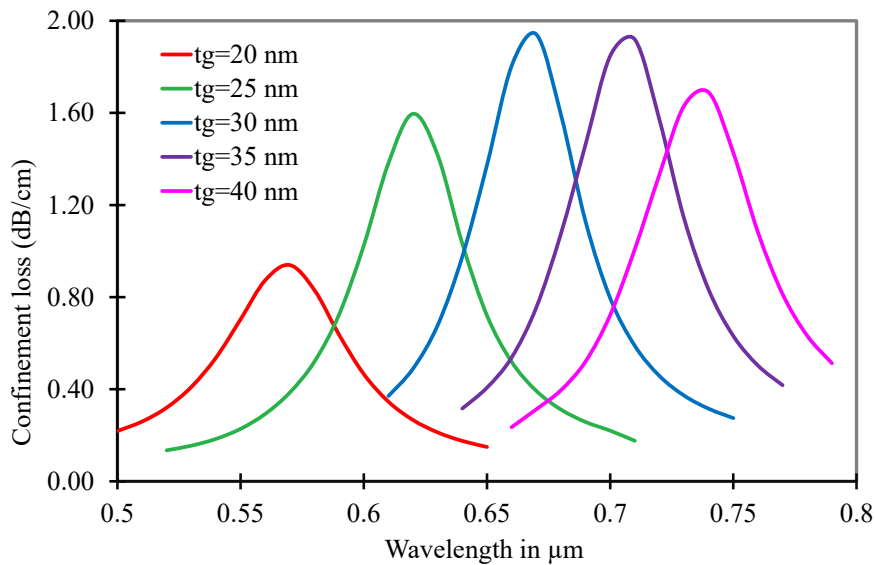


Figure 4.1: Confinement loss with different thicknesses of Gold layer ( $t_g$ ).

30 nm at an operating wavelength of 0.67  $\mu\text{m}$ . We observe the effect of  $t_g$  by changing its value from the optimized value while other parameters have been kept undisturbed. So,  $t_g$  is varied by  $\pm 5$  nm and  $\pm 10$  nm from the optimized value and for each case, the confinement loss is found decreased with a different resonance wavelength depicted in figure 4.1. For  $t_g$  equals to 20 nm, 25 nm, 35 nm, and 40 nm, the confinement losses are 0.939 dB/cm, 1.60 dB/cm, 1.92 dB/cm and 1.69 dB/cm with resonance wavelength of 0.57 nm, 0.62 nm, 0.71 nm and 0.74 nm respectively with RI = 1.38 shown in Table 4.1. So, using the same sensor with different  $t_g$  different resonance wavelengths will be found.

Table 4.1: Effect of  $t_g$  on Confinement Loss with RI = 1.38.

$t_g$ (nm)	$\lambda$ ( $\mu\text{m}$ )	Maximum Confinement loss (dB/cm)
20	0.57	0.939
25	0.62	1.60
30	0.67	1.94
35	0.71	1.92
40	0.74	1.69

Table 4.2: Performance Analysis of The Sensor with Different Air-holes Height.

Value of $h_1$ and $h_2$	RI = 1.38		RI = 1.39		AS (RIU <sup>-1</sup> )
	$\lambda$ ( $\mu\text{m}$ )	Maximum confinement loss (dB/cm)	$\lambda$ ( $\mu\text{m}$ )	Maximum confinement loss (dB/cm)	
-5%	0.67	3.42	0.71	5.02	428
Optimum	0.67	1.94	0.71	2.88	391
+5%	0.66	1.04	0.71	1.58	447

#### 4.2.1.2 Variation of Air Hole Height

Here, the effect of the height of the air hole on the performance of the sensor will be analyzed and discussed with respect to WS and AS. To detect the effect of air hole height, we have manually changed the height of the air holes keeping other parameters undisturbed. The height of the air holes has been changed  $\pm 5\%$  of the optimum height and then the CL has been calculated and plotted against wavelength as shown in figure 4.2 for RI of 1.38 and 1.39 with appropriate labeling. From the figure, it is clear that

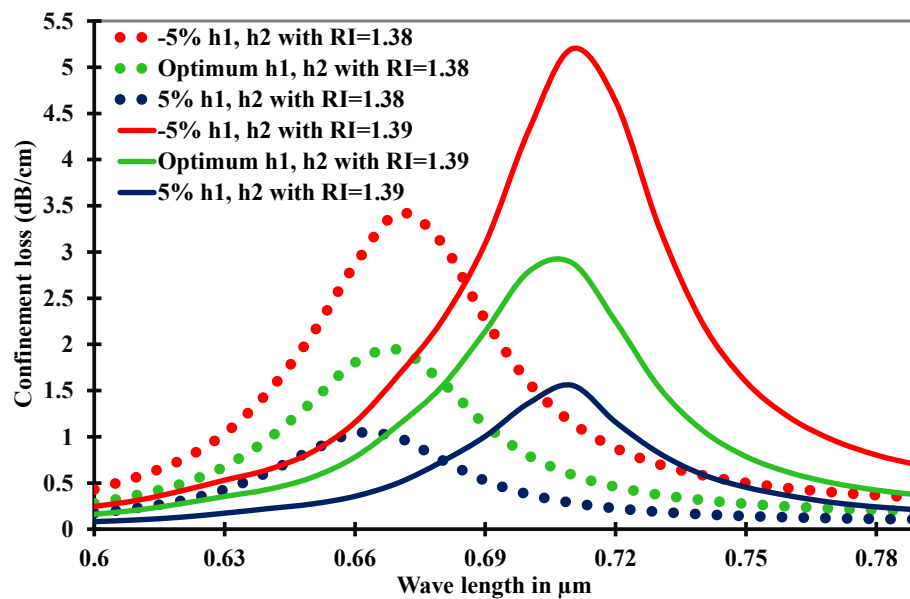


Figure 4.2: Effect of air holes height on confinement loss with RI = 1.38 and 1.39.

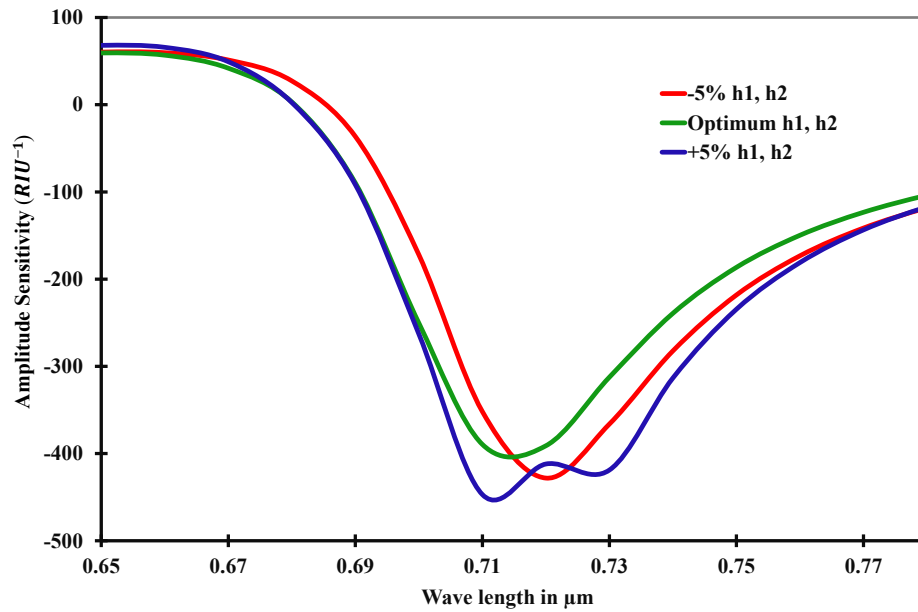


Figure 4.3: Effect of the height of air holes on AS with RI = 1.38 and 1.39.

the CL increases if the height of the air-holes is decreased and vice versa for both RI of 1.38 and 1.39. If the height of the air hole decreases, the CL increases because of the amount of leakage from the core to the cladding increases. On the other hand, when the height of the air hole increases the amount of leakage decreases which results in lower confinement losses. So, the air-hole height is inversely proportional to the confinement losses as well as WS. The resonance wavelength slightly increases and shifts with the decrements of the air hole's height (same as the CL) and vice versa. Figure 4.3 labels the AS of the proposed sensor showing the effect of height of air hole on AS. From figure 4.2, the maximum CLs are 3.42 dB/cm and 5.02 dB/cm for RI of 1.38 and 1.39 shown in Table 4.2. Figure 4.3 indicates that AS curve is a little bit unstable for the increase of height of air-hole, however, the curve becomes balanced in fashion for decreasing height of air hole.

#### 4.2.1.3 Effect of Inclination

This subsection highlights the effect of angular displacement ( $\Phi$ ) of the air holes in the case of WS. Here the change of  $\Phi$  the air hole is done intentionally to analyze its effect on sensor performance while the other parameters are considered unchanged. The air holes are placed with an  $\Phi$  of  $\pm 2^\circ$  and  $\pm 4^\circ$  and the CL is measured and plotted in figure 4.4. The positive  $\Phi$  of the air holes is plotted with a solid line and the negative with a dotted line. The CLs due to positive and negative changes in  $\Phi$  have overlapped with each other and these changes in  $\Phi$  increase the CLs. Using the optimum parameters with no change in  $\Phi$ , the maximum CL is 1.94 dB/cm at a resonance wavelength of

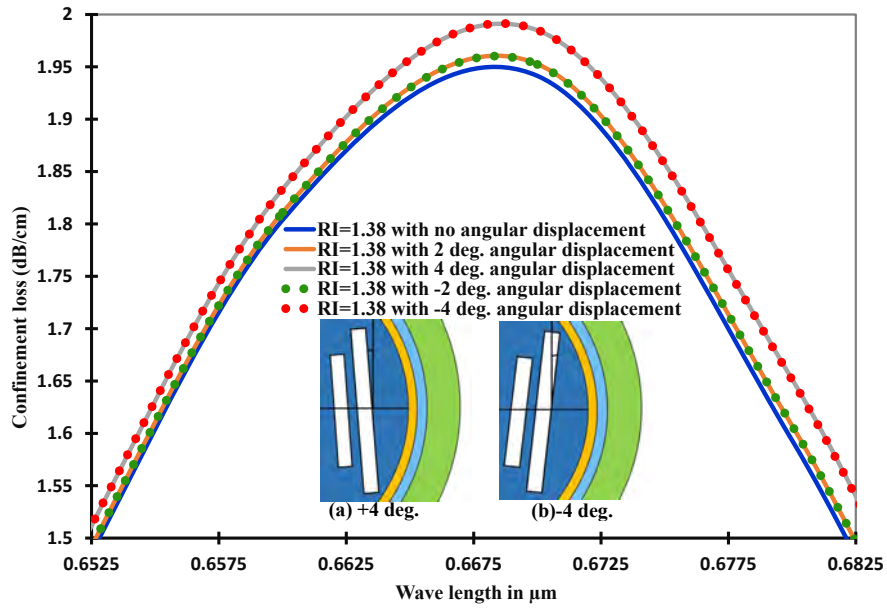


Figure 4.4: Effect of inclination on confinement loss with RI = 1.38.

Table 4.3: Effect of Inclination on Confinement Loss with RI = 1.38.

Inclination(°)	$\lambda(\mu\text{m})$	Maximum Confinement loss (dB/cm)
-4	0.67	1.99
-2		1.95
0		1.94
+2		1.95
+4		1.99

0.67 nm. With a change of  $\pm 2^\circ$  and  $\pm 4^\circ$  in  $\Phi$ , the CLEs are 1.95dB/cm and 1.99 dB/cm respectively given in Table 4.3. Due to inclination, the amount of leakage of light from the core to the cladding increases and therefore enhances the CLEs.

Finally, we can say that the sensor performance will not be hampered if any inclination occurs during fabrication or the sensor is twisted during implementation. Rather it will increase the CL as well as the sensitivity of the proposed sensor operating at the same wavelength.

## 4.2.2 Inclined Approach

In this subsection, for the inclined approach of the air holes, the angular displacement ( $\Phi$ ) of the air holes is optimized first and then step by step the thickness of the gold layer, height, and width of the air holes, addition and thickness variation of the adhesive layer, effect of the metallic strip instead of circular sensing layer, thickness variation of analyte layer and lastly the thickness variation of PML is studied. An optimized value is chosen for each parameter.



### 4.2.2.1 Inclination of Air holes

In this subsection, we will optimize the angular displacement ( $\Phi$ ) of the air holes and figure 4.5 shows the cross sectional view with different value of  $\Phi$ . Due to the variation of  $\Phi$ , the air hole rotates from the center axis and for  $\Phi = 50^\circ$ , two adjacent air holes just touch one another. Again, for  $\Phi = 90^\circ$  in figure 4.5 (s), they just overlap each other. For simulation purpose, we just consider  $\Phi$  up to  $50^\circ$ . Since it is the first taken parameter for optimization, we will just consider other non-optimized parameters here and they will remain undisturbed while the change in  $\Phi$  will be made. Using RI = 1.38 and RI = 1.39, the performance of the proposed sensor will be optimized for different  $\Phi$  of the air holes. Figure 4.6 (a) shows the CLEs of the proposed sensor for different  $\Phi$ . The solid lines labeled in figure 4.6 (a) show CLEs for RI = 1.38 and the dotted lines for RI = 1.39. From figure 4.6 (a), CL increases with the increase of the angular rotation of the air holes because it increases the total amount of leakage from core to cladding region, and the resonance wavelength moves to a larger wavelength.

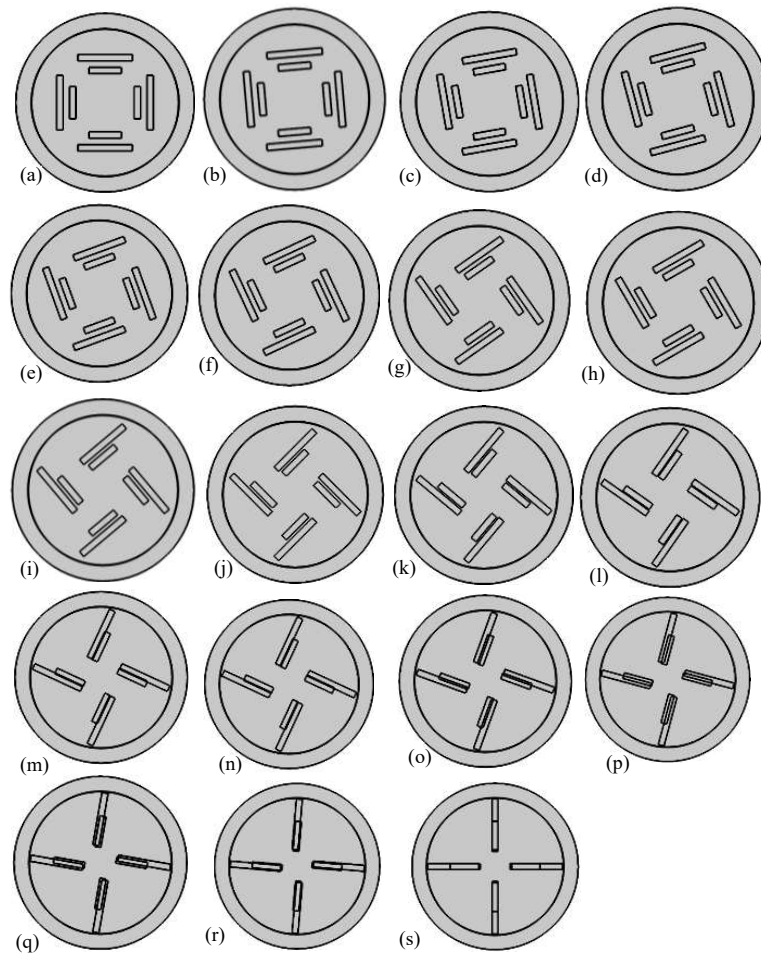


Figure 4.5: Angular rotation of the air holes with  $\Phi$  (a)  $0^\circ$  to (s)  $90^\circ$  with a increment of  $5^\circ$  for the geometrical structure of the proposed sensor.

After the resonance point, CL drops to a lower value with the increment of wavelength but changes become asymmetric for the larger value of  $\Phi$ . Here, the angular rotation is varied from  $30^\circ$  to  $40^\circ$  with a variation of  $5^\circ$ . The change in AS due to the variation of the angular rotation of the air holes is shown in figure 4.6 (b) with proper labeling. From figure 4.6 (a), we can see that CL increases with the  $\Phi$  but from figure 4.6 (b) maximum AS is  $-571.04$  1/RIU for  $\Phi = 35^\circ$  at a wavelength of 810 nm with a sharp AS curve having a minimum FWHM of 57.50 nm. Necessary data are stored in table 4.4. So, we may conclude that maximum AS, minimum FWHM with a DA of 0.0174 per nm, great FOM of 104.34, and WS of 6000 nm/RIU are obtained for  $35^\circ$ . So  $\Phi = 35^\circ$  is chosen as an optimized value.

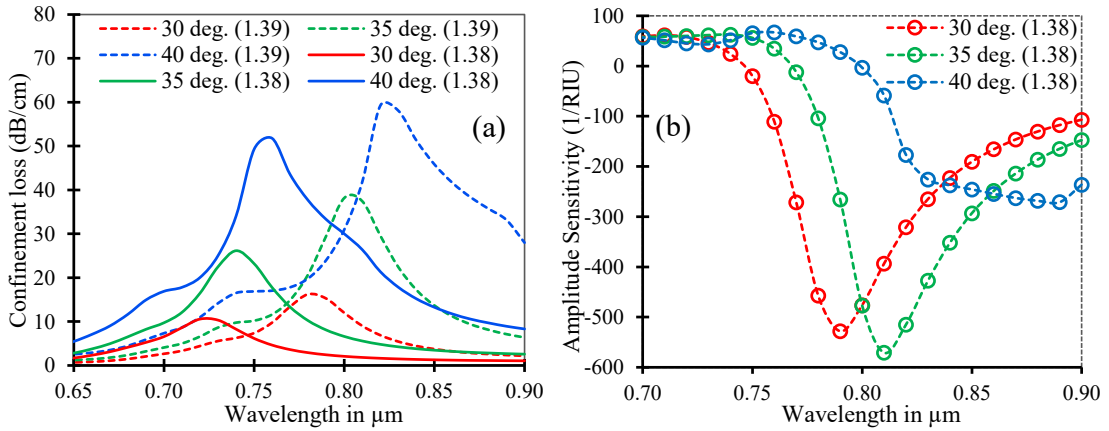


Figure 4.6: Effect of angular rotation of the air holes on (a) CL and (b) AS with RI of 1.38 and 1.39 for the geometrical structure of the proposed sensor.

#### 4.2.2.2 Thickness variation of the gold layer

The choice of appropriate plasmonic material plays a vital role in the overall performance of the sensor. For the proposed structure, gold is chosen as the plasmonic material. The thickness of the gold layer ( $t_{au}$ ) plays a vital role in tuning. Figure 4.7 (a) shows the CL for different thickness of  $t_{au}$  with  $\Phi = 35^\circ$ . The solid lines labeled in figure 4.7 (a) show CL for RI = 1.38 and the dotted lines for RI = 1.39. Due to the damping effect, CL decreases with the increase of  $t_{au}$ . The difference between maximum obtained CL for RI = 1.39 and RI = 1.38 is 29.02 dB/cm and other data are summarized in table 4.4. Figure 4.7 (b) shows the graphical representation of AS for RI= 1.38 and the maximum AS is obtained for  $t_{au} = 25$  nm at a wavelength of 760 nm.

Again,  $t_{au} = 25$  nm shows a minimum full width half maximum (FWHM) of 49.50 nm which indicates the sharpness of the loss curve. In addition, a maximum ( $\text{RIU}^{-1}$ ) of  $-677.52$  is obtained at this thickness having a difference of  $51.26$   $\text{RIU}^{-1}$  from the  $2^{\text{nd}}$  maximum AS with maximum FOM. Making a trade-off among AS, FOM, WS, DA,

Table 4.4: Different Geometrical Parameters optimization of the proposed sensor for RI = 1.38 and 1.39

Parameters	Quantity	Peak CL (dB/cm)		Peak AS (1/RIU)	Peak WS	FWHM (nm)	DA (1/nm)	FOM
		1.39	1.38					
Angular phase, $\Phi$ (Deg.)	30,	16.23,	10.57,	-528.04,	6000,	63.00,	0.0159,	95.24,
	35,	38.17,	26.15,	-571.04,	6000,	57.50,	0.0174,	104.34,
	40	59.22	51.77	-271.11	6000	80.00	0.0125	75.00
Thickness of gold layer, $t_{au}$ (nm)	20,	61.06,	29.96,	-626.26,	5000,	51.50,	0.0194,	98.09,
	25,	54.34,	32.04,	-677.52,	6000,	49.50,	0.0202,	121.21,
	30	16.24	10.57	528.03	6000	65.00	0.0154	92.31
1st layer airhole height, $h_1$ (nm)	2.375,	52.67,	30.09,	-629.54,	5000,	53.50,	0.0187,	93.46,
	2.500,	54.34,	32.04,	-677.52,	6000,	50.75,	0.0197,	118.22,
	2.625	52.14	30.83	-697.53	6000	53.60	0.0186	111.94
1st layer airhole width, $w_1$ (nm)	0.475	49.72,	29.51,	-661.78,	6000,	50.00,	0.0200,	120.00,
	0.500	54.34,	32.04,	-677.52,	6000,	50.75,	0.0197,	118.22,
	0.525	49.32	34.90	-695.27	6000	52.00	0.0192	115.38
2nd layer airhole height, $h_2$ (nm)	4.0375,	68.84,	49.79,	-546.49,	6000,	47.00,	0.0213,	127.66,
	4.2500,	54.34,	32.04,	-677.52,	6000,	50.75,	0.0197,	118.22,
	4.4625	31.82	19.89	-620.38	6000	55.00	0.0181	109.09
2nd layer airhole width, $w_2$ (nm)	0.475	59.35,	34.23,	-679.17,	6000,	50.75,	0.0197,	118.22,
	0.500	54.34,	32.04,	-677.52,	6000,	50.75,	0.0197,	118.22,
	0.525	49.32	29.83	-667.86	6000	51.75	0.0193	115.94
Airhole height, $h_1$ & $h_2$ (nm)	with -5%, optimum,	80.62,	47.73,	-608.39,	5000,	48.50,	0.0206,	103.09,
	with +5%	54.34,	32.04,	-677.52,	6000,	50.75,	0.0197,	118.22,
		29.80	18.54	-627.71	6000	59.00	0.0169	101.69
Airhole width, $w_1$ & $w_2$ (nm)	with -5%, optimum,	54.17,	31.56,	-660.57,	6000,	51.50,	0.0194,	116.50,
	with +5%	54.34,	32.04,	-677.52,	6000,	50.75,	0.0197,	118.22,
		54.42	32.56	-682.72	6000	51.40	0.0195	116.73

and FWHM,  $t_{au} = 25$  nm is taken as an optimized thickness of the gold Layer. Fig.4.7 (c) and (d) show the CL and AS of the proposed sensor respectively with  $\Phi = 0^\circ$  and the maximum is obtained at  $t_{au} = 30$  nm. At a wavelength of 750 nm, the maximum AS is  $-455.95$  RIU $^{-1}$  which is lower than the maximum AS obtained for  $t_{au} = 25$  nm. However, we can conclude that the choice of gold layer thickness directly depends on the  $\Phi$  of the air holes, and the resonance wavelength of maximum AS becomes different for different value of  $t_{au}$ .

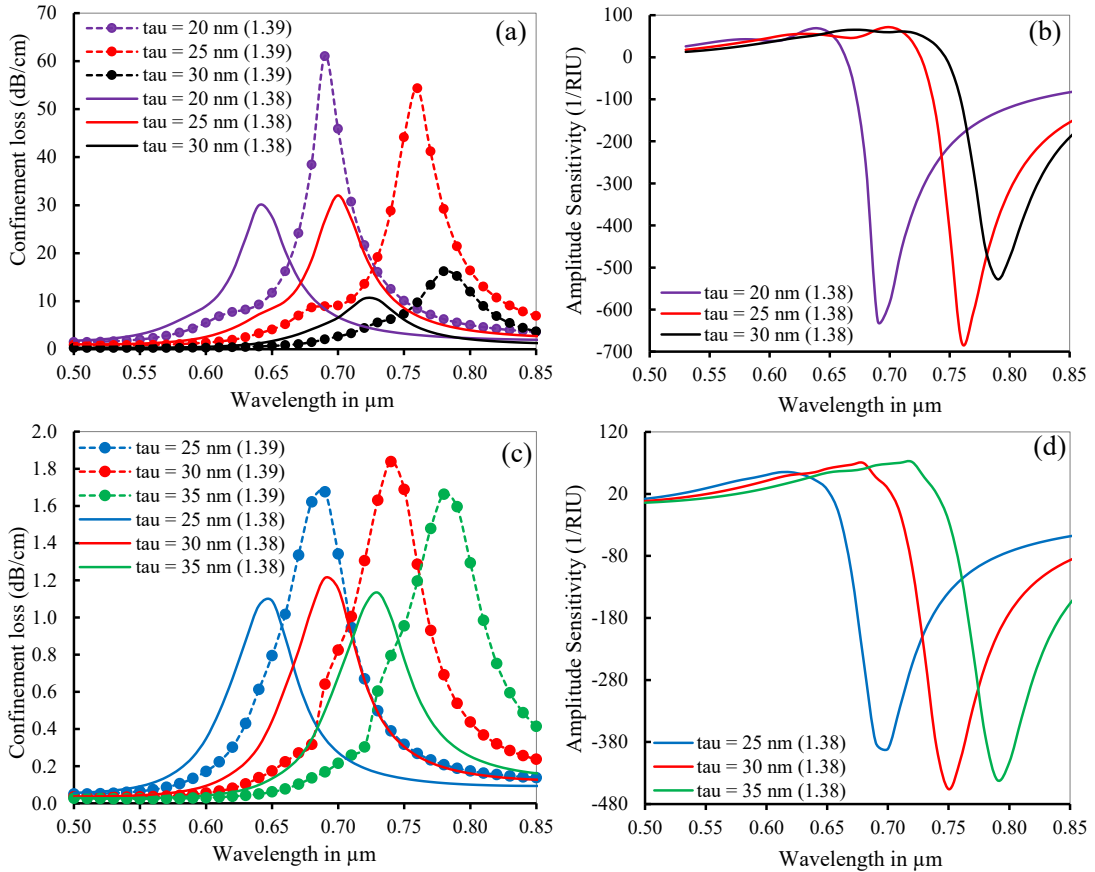


Figure 4.7: Effect of gold layer thickness on (a), (c) CL and (b), (d) AS with  $\Phi = 35^\circ$  and  $0^\circ$  respectively for RI of 1.38 and 1.39 of the proposed geometrical sensor structure.

#### 4.2.2.3 Variation of Air Hole height

This subsection will discuss the effect of air holes height variation on CL peak, AS, resonance wavelength variation, and WS with FOM and FWHM. Three cases will be considered for the height variation of the air holes. Firstly, the height of the 1<sup>st</sup> layer air holes from the center will be varied and the other parameters including the 2<sup>nd</sup> layer air hole height will remain constant. Secondly, the height of the 2<sup>nd</sup> layer air hole will be varied and all other parameters will remain undisturbed. Lastly, the height of both air holes will be varied in the same fashion keeping others constant. Figure 4.8 (a) and

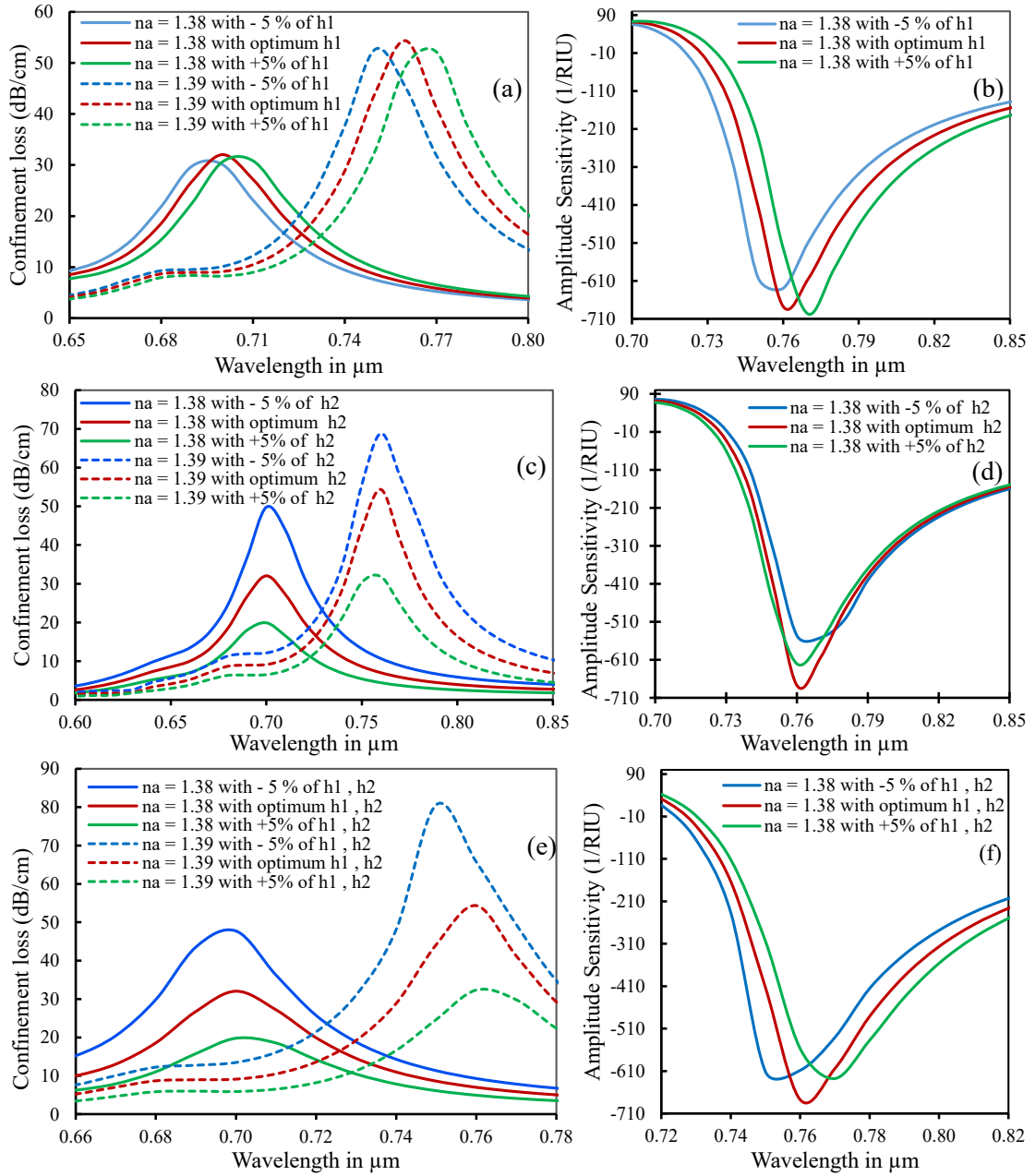


Figure 4.8: Effect of air-hole height on (a), (c), (f) CL and (b), (d), (f) AS with  $\Phi = 35^\circ$  and  $t_{au} = 25$  nm for RI of 1.38 and 1.39 of the proposed geometrical sensor structure.

(b) show the effect of  $h_1$  on CL and AS respectively. In figure 4.8 (a), CL is maximum for  $h_1 = 2.50 \mu\text{m}$  and resonance peaks shift to different wavelengths with the change of  $h_1$  but CL decreases for other cases. From table 4.4, we may conclude that FWHM is minimum for  $h_1 = 2.50 \mu\text{m}$  and maximum FOM is obtained at the same time with higher DA. So,  $h_1 = 2.50 \mu\text{m}$  is taken considering the above-mentioned parameters.

Now the height of the  $2^{\text{nd}}$  layer air holes,  $h_2$  will be varied only keeping other parameters undisturbed. Figure 4.8 (c) and (d) depict the effect of  $h_2$  on CL and AS respectively for this case. From figure 4.8 (c), CL increases with the decrements of  $h_2$  but resonance peaks are constant in a fixed wavelength of 700 nm and 760 nm for RI = 1.38 and RI = 1.39, respectively. The change of the  $h_2$  is inversely proportional to the amount of leakage light and the maximum change of CL is almost 22.3 dB/cm for  $h_2 = 4.25 \mu\text{m}$ . Maximum AS obtained from figure 4.8 (d) is  $-677.52 \text{ RIU}^{-1}$  for  $h_2 = 4.25 \mu\text{m}$  with constant WS. FWHM, DA, and FOM follow the same fashion as CL. Consider a tradeoff among the above-mentioned parameters,  $h_2 = 4.25 \mu\text{m}$  is chosen as an optimized value for the height of the  $2^{\text{nd}}$  layer air holes. Lastly, both  $h_1$  and  $h_2$  are varied in the same fashion and the effect is shown in figure 4.8 (e) and (f). From figure 4.8 (e) and (f), we can see that mostly the CL, FWHM, DA, and AS follow the effect of changing  $h_2$  only but WS, FOM, and their resonance peaks follow the effect of changing  $h_1$  only. CL is inversely proportional to the increment of both  $h_1$  and  $h_2$ . Maximum AS, FOM obtained from this case is with  $h_1 = 2.50 \mu\text{m}$  and  $h_2 = 4.25 \mu\text{m}$ . So finally, the height of the air holes is optimized and a summary of the optimized result is given in table 4.4.

#### 4.2.2.4 Variation of Air Hole Width

In the earlier subsection, the effect of air holes width variation will be discussed on CL peak, AS, resonance wavelength variation, and WS with FOM and FWHM. For the width variation of the air holes, the same three cases will be considered here as the air hole height. Figure 4.9 (a) and (b) show the effect of  $1^{\text{st}}$  layer air hole width variation on CL and AS, respectively. In figure 4.9 (a) and (b) CL and AS increase with the increment of  $w_1$  but resonance peaks are constant in a fixed wavelength of 700 nm and 760 nm for RI = 1.38 and RI = 1.39 respectively. From table 4.4, we may conclude that AS, FWHM, DA, and FOM decrease with the increment of  $w_1$  but WS remains constant. So,  $w_1 = 0.50 \mu\text{m}$  is taken considering the above-mentioned parameters.

Now the Width of the  $2^{\text{nd}}$  layer air width,  $w_2$  will be varied only keeping other parameters undisturbed. Figure 4.9 (c) and (d) depict the effect of  $w_2$  on CL and AS respectively. From figure 4.9 (c), CL decreases with the increment of  $w_2$ . The change of the  $w_2$  is inversely proportional to the amount of leakage light and it does not shift the resonance condition. Using table 4.4, we may conclude that As, DA, and FOM de-

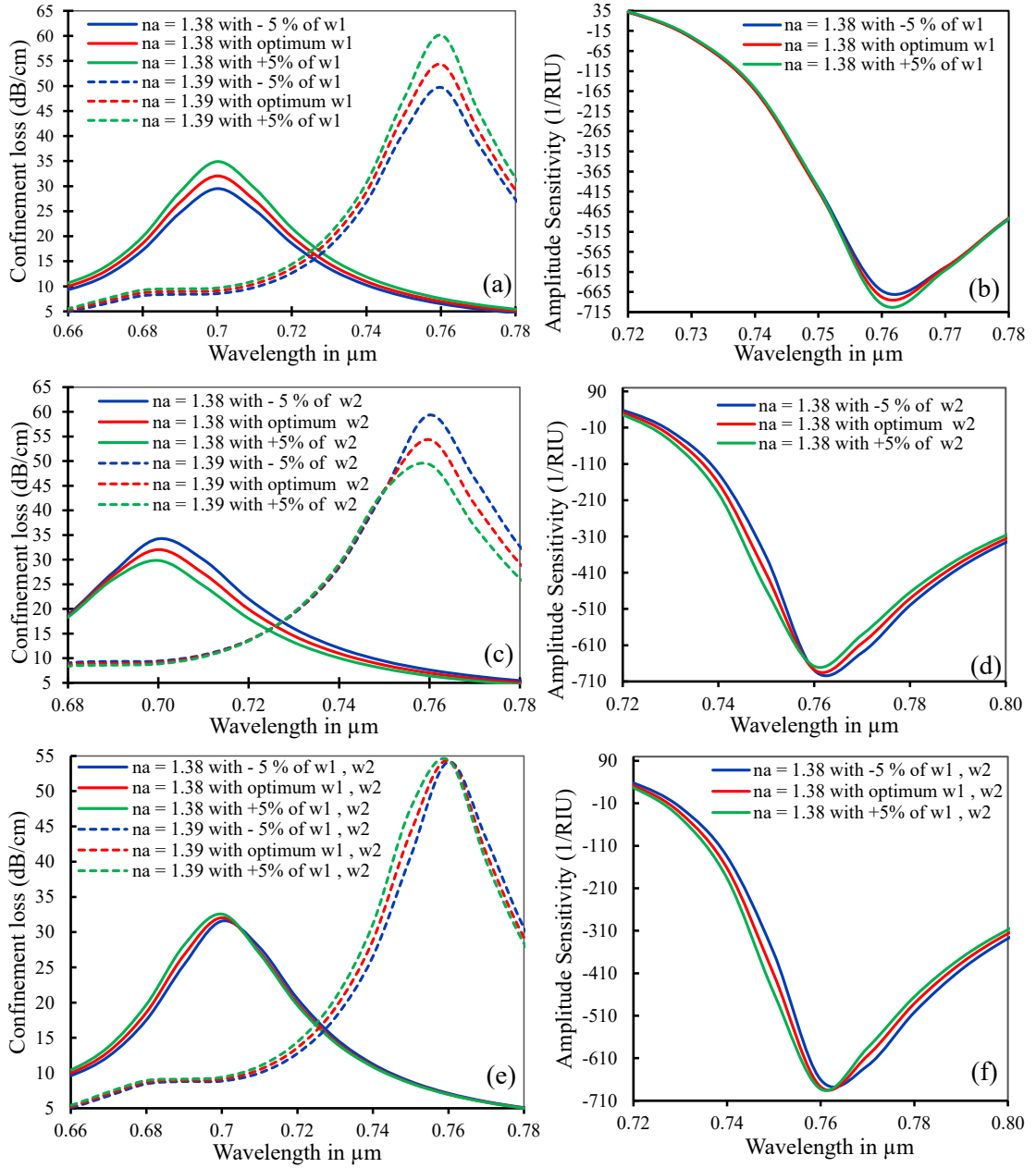


Figure 4.9: Effect of air-hole width on (a), (c), (f) CL and (b), (d), (f) AS with  $\Phi = 35^\circ$  and  $t_{au} = 25$  nm for RI of 1.38 and 1.39 of the proposed geometrical sensor structure.

crease with the increment of  $w_2$  but FWHM becomes wider with the increment of  $w_2$ . Considering a tradeoff among the above-mentioned parameters,  $w_2 = 0.50 \mu\text{m}$  is chosen as an optimized value for the width of  $2^{\text{nd}}$  layer air holes with constant WS.

Lastly, both  $w_1$  and  $w_2$  are varied in the same fashion and the effect is shown in figure 4.9 (e) and (f). From figure 4.9 (e) and (f), we can conclude that CL and AS do not change very much for both  $h_1$  and  $h_2$ , but CL changes an average of 22.25 dB/cm due to a change of RI from 1.38 to 1.39. Maximum FOM and minimum DA obtained from this case is  $w_1 = 0.50 \mu\text{m}$  and  $w_2 = 0.50 \mu\text{m}$ . So finally, the width of the air holes is optimized, and a summary of the optimized result is given in table 4.4.

#### 4.2.2.5 Addition and Effect of the Adhesive Layer

In this subsection, the effect of adhesive layer thickness on the performance of the proposed sensor is discussed considering other optimized parameters as constant for the inclined approach of the air holes. Figure 4.10 shows the graphical representation of the geometrical structure of the proposed sensor with the adhesive layer. Here  $\text{TiO}_2$  is used as the adhesive layer and the thickness of  $\text{TiO}_2$  is  $t$ . Now,  $t$  is varied to get an optimized output. Here,  $t$  is varied up to 10 nm and the effect of  $t$  is presented in figure 4.11.

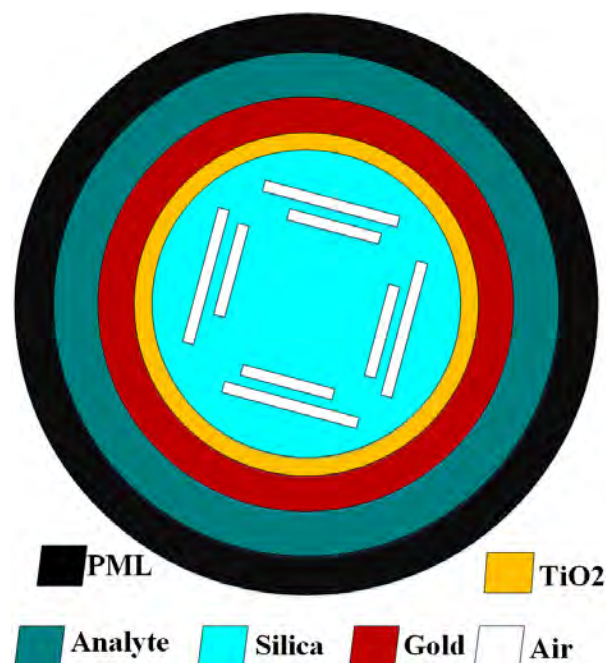


Figure 4.10: Geometrical structure of the proposed sensor with the adhesive layer.

CL increases with RI and maximum AS ( $\text{RIU}^{-1}$ ) of -698.59 is obtained for  $t = 5 \text{ nm}$  with an average AS of  $-670.35 \text{ RIU}^{-1}$ . WS remained constant for different values of  $t$ , and all the necessary data, including maximum CL with the operating wavelengths in



Table 4.5: Effect of the adhesive layer on CL and AS with RI of 1.38 and 1.39 for the geometrical structure of the proposed sensor.

Thickness of TiO <sub>2</sub> , t (nm)	Maximum				WS (nm/RIU)	AS (RIU <sup>-1</sup> )
	Confinement loss (dB/cm)		λ(nm)			
	1.39	1.38	1.39	1.38		
0	54.34	32.03	760	700	6000	-677.52
5	51.20	32.89	790	730	6000	-698.59
10	31.30	31.30	820	760	6000	-634.93

nm, is shown in table 4.5. Considering all the necessary data,  $t = 5$  nm is chosen as an optimized value for the TiO<sub>2</sub> layer.

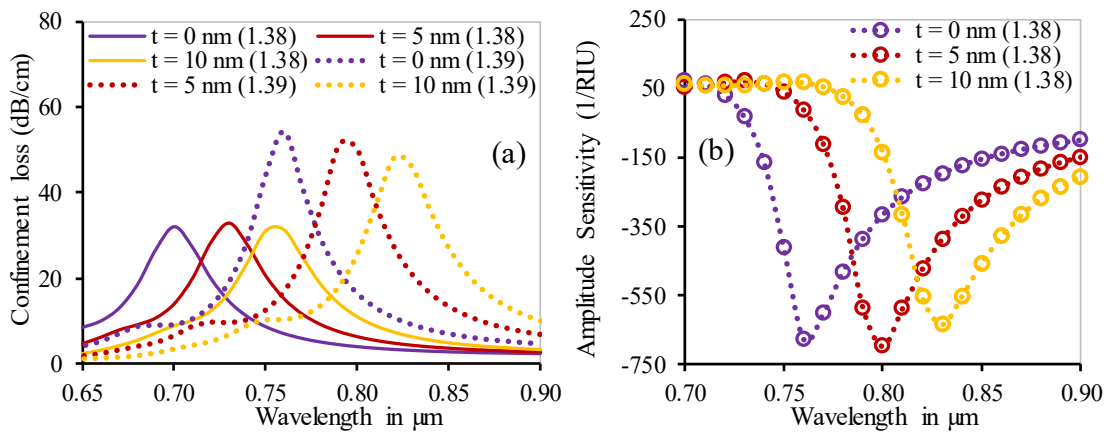


Figure 4.11: Effect of the adhesive layer on (a) CL and (b) AS with RI of 1.38 and 1.39 for the geometrical structure of the proposed sensor.

#### 4.2.2.6 Effect of Metallic Stripe

In this subsection, the effect of the metallic stripe on the performance of the proposed sensor is discussed considering other optimized parameters as constant for the inclined approach of the air holes. Here the circular ring of TiO<sub>2</sub> and gold layer is replaced by four metallic stripes on the outer surface of the proposed SiO<sub>2</sub> structure. CL increases due to the use of metallic stripe but resonance wavelength shifted to lower wavelength. At the same time, WS remains the same but maximum AS (RIU<sup>-1</sup>) decreases to 650.32 from -698.59 (obtained for the circular ring) shown in Figure 4.12. From table 4.6, AS (RIU<sup>-1</sup>) decreases to 6.91 % due to the use of metallic stripe but it also uses 54.45 % less metallic layer used totally in the previous model.

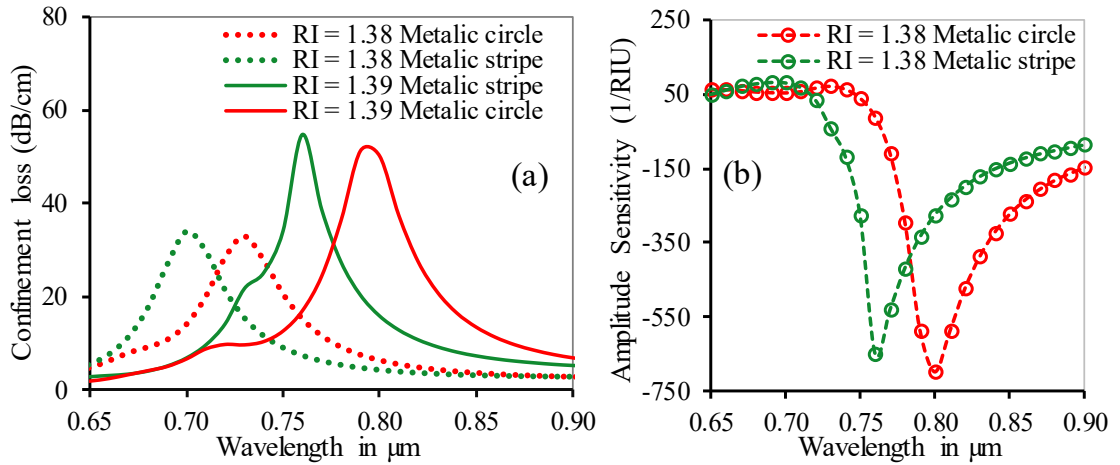


Figure 4.12: Effect of the metallic stripe on (a) CL and (b) AS with RI of 1.38 and 1.39 for the geometrical structure of the proposed sensor.

Table 4.6: Effect of the metallic stripe on CL and AS with RI of 1.38 and 1.39 for the geometrical structure of the proposed sensor.

Factors	Maximum		$\lambda(\text{nm})$		WS (nm /RIU)	AS (RIU <sup>-1</sup> )	Perimeter length, S ( $\mu\text{m}$ )	$\Delta$ AS (-%)	$\Delta$ S (+%)
	Confinement								
	1.39	1.38	1.39	1.38					
Metallic Ring	51.20	32.89	790	730	6000	-698.59	36.002	6.91	54.45
Metallic Stripe	54.76	33.91	760	700	6000	-650.32	16.4012		

#### 4.2.2.7 Thickness Variation of Analyte Layer

In this subsection, the effect of analyte layer thickness (ALT) variation on the performance of the proposed sensor is discussed considering other optimized parameters as constant for the inclined approach of the air holes. Here, the thickness of analyte layer is varied from 1.15  $\mu\text{m}$  up to 1.25  $\mu\text{m}$  with a variation of 0.05  $\mu\text{m}$  and the effect of analyte layer thickness variation is presented in figure 4.13 (a) and (b). CL is lower for

Table 4.7: Effect of the analyte layer thickness on CL and AS with RI of 1.33 and 1.34 for the geometrical structure of the proposed sensor.

Thickness of analyte layer ( $\mu\text{m}$ )	Maximum		$\lambda(\text{nm})$		WS (nm/RIU)	AS (RIU <sup>-1</sup> )
	Confinement					
	1.34	1.33	1.34	1.33		
1.15	9.0116	7.156	600	590	1000	-82.844
1.20	9.0111	7.155	600	590	1000	-82.798
1.25	9.0141	7.159	600	590	1000	-82.773

analyte thickness of 1.20  $\mu\text{m}$  but AS (RIU<sup>-1</sup>) is inversely proportional to the variation

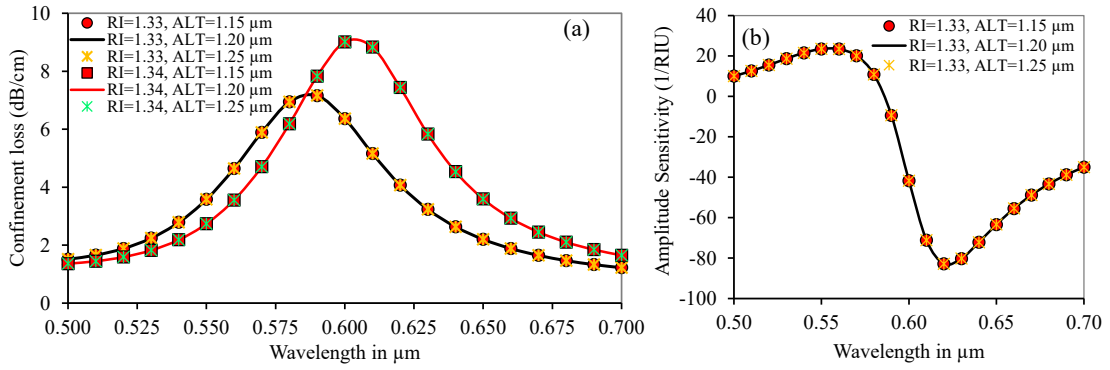


Figure 4.13: Effect of the analyte layer on (a) CL and (b) AS with RI of 1.33 and 1.34 for the geometrical structure of the proposed sensor.

of thickness. WS remained constant for different thickness of analyte layer, and all the necessary data, including maximum CL with the operating wavelengths in nm, is shown in table 4.7. Changes in the performance parameters is negligible due to the thickness variation of the analyte layer. Considering all the necessary data, analyte thickness of 1.20  $\mu\text{m}$  is chosen as an optimized value for the analyte layer.

#### 4.2.2.8 Thickness Variation of PML

In this subsection, the effect of PML thickness variation on the performance of the proposed sensor is discussed considering other optimized parameters as constant for the inclined approach of the air holes. Here, the thickness of PML is varied from 10% to 20% of the total radius of the proposed structure with a variation of 5% and the effect of PML thickness variation is presented in figure 4.14 (a) and (b). CL is lower for RI

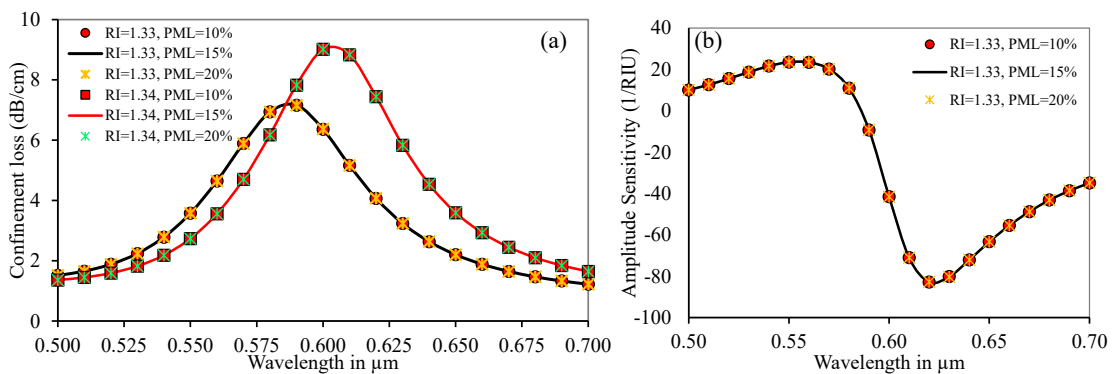


Figure 4.14: Effect of the PML on (a) CL and (b) AS with RI of 1.33 and 1.34 for the geometrical structure of the proposed sensor.

= 1.34 with PML thickness of 15% but maximum AS ( $\text{RIU}^{-1}$ ) of -82.834 is obtained for this thickness. WS remained constant for different thickness of analyte layer, and all the necessary data, including maximum CL with the operating wavelengths in nm,

Table 4.8: Effect of the PML thickness on CL and AS with RI of 1.33 and 1.34 for the geometrical structure of the proposed sensor.

Thickness of PML	Maximum Confinement				WS (nm/RIU)	AS (RIU <sup>-1</sup> )
	loss (dB/cm)		$\lambda$ (nm)			
	1.34	1.33	1.34	1.33		
10 %	9.013	7.156	600	590	1000	-82.821
15 %	9.009	7.161	600	590	1000	-82.834
20 %	9.017	7.159	600	590	1000	-82.734

is shown in table 4.8. Changes in the performance parameters is negligible due to the thickness variation of the PML. Considering all the necessary data, PML thickness of 15% of the total radius is chosen as an optimized value for the PML.

### 4.3 Performance Analysis

In this section, the performance of the proposed sensor will be discussed with proper numerical records with appropriate graphical representation. Here, the sensitivity of the proposed sensor has been studied based on the following parameters a) confinement loss, b) wavelength sensitivity, c) amplitude sensitivity, d) sensor resolution, and e) linearity considering the normal and inclined approach of the air holes. For the inclined approach, single and double sensing layer with circular ring and arc is considered.

#### 4.3.1 Dispersion relationship

The sensitivity of a fiber sensor depends on the geometrical design of the sensor, modulation intensity of light, and interaction between the core and SPP mode. This subsection will discuss the dispersion relation as a function of wavelength for the SPP mode and core mode for an analyte with a specific RI.

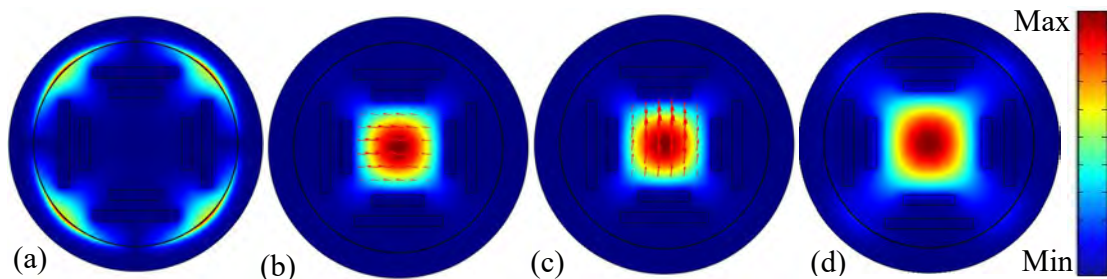


Figure 4.15: Optical field distribution for the (a) SPP Mode, (b) to (c) core guided mode for both  $x$ - and  $y$ - polarization (d) coupling mode.

### 4.3.1.1 Normal Approach

Figure 4.15 shows the field distribution of the (a) SPP mode, (b) to (c) core guided mode for both  $y$ - and  $x$ - polarization respectively, and (d) coupling mode between core and SPP mode of the proposed sensor. From the dispersion relation with wavelength depicted in figure 4.16, we can conclude that both  $y$ - and  $x$ -polarized modes have the same sensitivity because their confinement loss is the same for the same analyte. For all other calculations, we are considering only the  $y$ -polarized mode because the  $x$  plane of the proposed model is identical to the  $y$  plane. The dispersion relation for  $x$  and  $y$ -

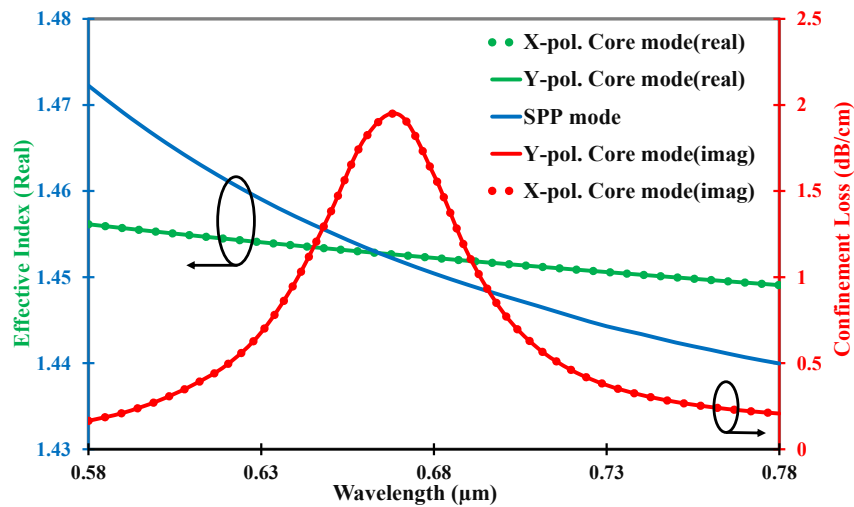


Figure 4.16: Dispersion relation as a function of wavelength for the SPP mode and core mode with an analyte RI of 1.38.

polarized mode of the proposed sensor as a function of wavelength is depicted in figure 4.16 for the both SPP mode and core mode. For an analyte RI of 1.38, the maximum CL is 1.94 dB/cm for both  $x$  and  $y$ - polarized mode at a wavelength of 0.67  $\mu\text{m}$ . CL curves are represented by the red dotted line and solid line for both  $x$  and  $y$ - polarized mode respectively. The blue and green lines (dotted line and solid line for  $x$  and  $y$ - polarized mode respectively) are used to denote the dispersion relation of the SPP mode and core mode respectively. The real value of the effective index for SPP and core mode is the same at 0.67  $\mu\text{m}$  and this corresponding wavelength is the so called resonance wavelength since phase matching happens at this wavelength transferring maximum energy which results in maximum CL.

### 4.3.1.2 Inclined Approach

Considering the inclined approach of the air holes, the basic dispersion relation among the SPP and core modes for RI = 1.38 is represented by figure 4.17 where the core

and SPP modes are embedded with proper labeling. Here, the primary axis is used to represent the imaginary value of the effective index of the core mode as CL, and the real value of the effective index of core and SPP mode is represented by the secondary axis for different values of RI. In figure 4.17, various labeling is used to differentiate between  $x$  and  $y$ - polarized confinement losses and the effective value of refractive indices. From

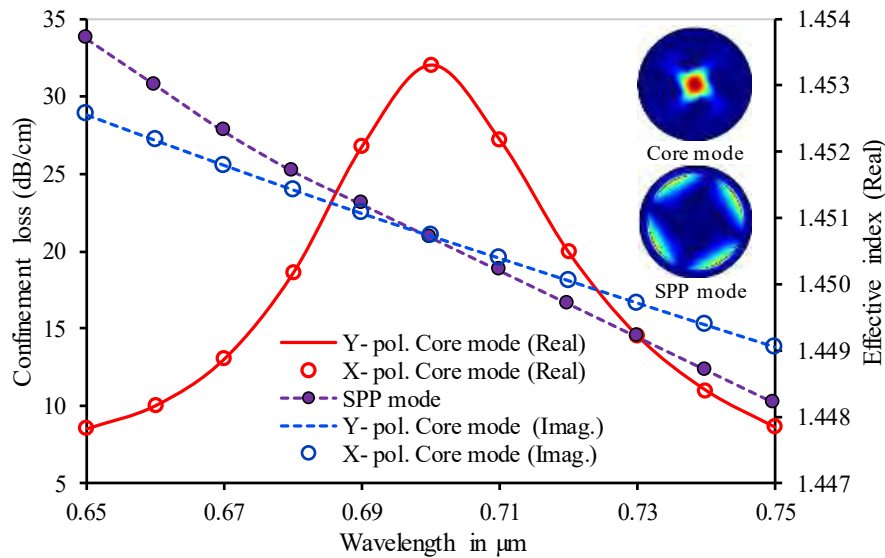


Figure 4.17: Phase matching condition among the SPP mode, core mode (imag.), and core mode (real) for RI = 1.38.

the numerical analysis, the real value of the effective indices is same for both  $x$  and  $y$ -polarization but there is a little difference between the CLEs. For example, maximum CL occurs at the operating wavelength of 700 nm and CLEs are 32.0382 and 32.0365 dB/cm for  $y$  and  $x$ -polarized mode respectively. In this particular wavelength phase matching condition occurs and the real value of the effective index of SPP and core mode becomes equal to each other. This particular wavelength is known as resonance wavelength and maximum energy is relocated from the core to the cladding. Since the interaction of the relocated energy and metal is stronger in  $y$ -polarized mode than the  $x$ -polarized mode, only the  $y$ -polarization will be considered for further calculation.

### 4.3.2 Confinement Loss

When lots of modes are kept in a small core, the core cannot bind all the modes inside the core. Some of them circulate partially out of the core, and leakage of energy occurs. Energy relocates from the core to the cladding layer, an EM wave penetrates in between the metal-dielectric interface, and this EM wave is known as the evanescent field. This evanescent field propagates from the core to the cladding layer and strikes the metal surface. It frees the weekly attached electrons from the metal surface and produces

SPW. Due to the leakage phenomenon, energy relocation from the core to the cladding layer decreases the total energy inside the core, resulting in CL. It is an essential central parameter to measure the proposed sensor's performance and is calculated through the Eqn. 3.4.

#### 4.3.2.1 Normal Approach

For the normal approach of the air holes with a certain value of the RI of the analyte, we have calculated the CL curve by Eqn. 3.4, and it reaches its maximum value at resonance wavelength. The maximum CLs gained from figure 4.18 are 0.439 dB/cm, 0.554 dB/cm, 0.726 dB/cm, 0.962 dB/cm, 1.38 dB/cm, 1.94 dB/cm, 2.88 dB/cm, 4.64 dB/cm, 7.86 dB/cm, 14.6 dB/cm, and 23.4 dB/cm at the resonant wavelength of 570 nm, 580 nm, 600 nm, 620 nm, 640 nm, 670 nm, 710 nm, 760 nm, 840 nm, 970 nm, and 1190 nm respectively for the value of RI from 1.33 to 1.43 with an increment of 0.01 in y-polarized mode. From figure 4.18, we can conclude that the CL of the fiber is increasing with the increase of RI of the analyte, and the phase matching condition is changed with the change of RI. The analytes of higher RI have a greater capability to absorb light than the lower ones. Since the analytes with different RI absorb different amounts of light, the phase matching condition occurs at a different wavelength; consequently, the resonance peak shifts.

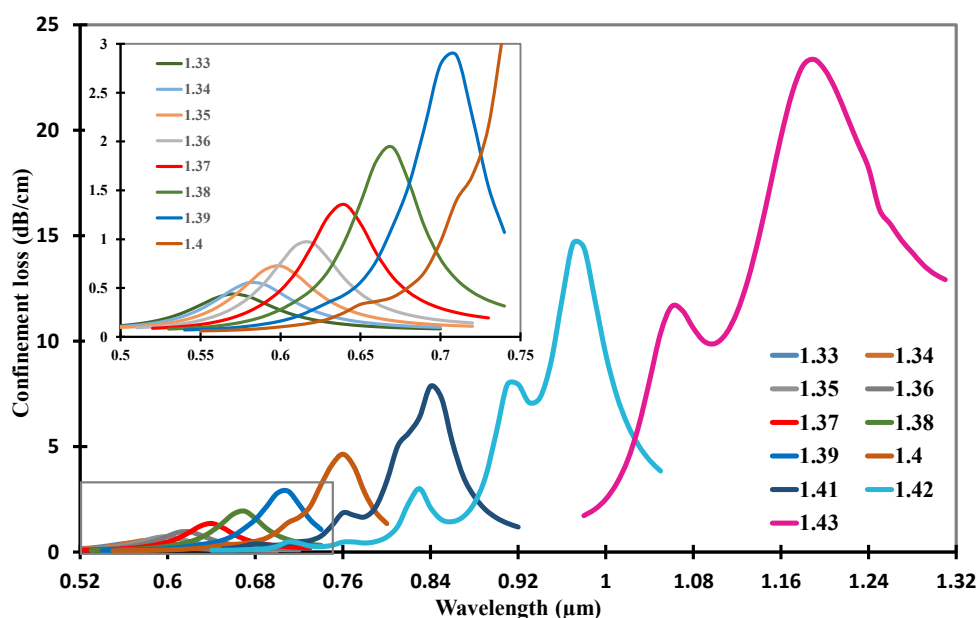


Figure 4.18: Confinement loss spectrum of the proposed sensor for core mode with analytes of different RI from 1.33 to 1.43.

### 4.3.2.2 Inclined Approach

Figure 4.19 shows the graphical representation of CL for different analytes from RI = 1.29 to RI = 1.42 with suitable labeling for the inclined approach of the air holes. From the above-mentioned figure, it can be ascertained that the peak of CL shifts from

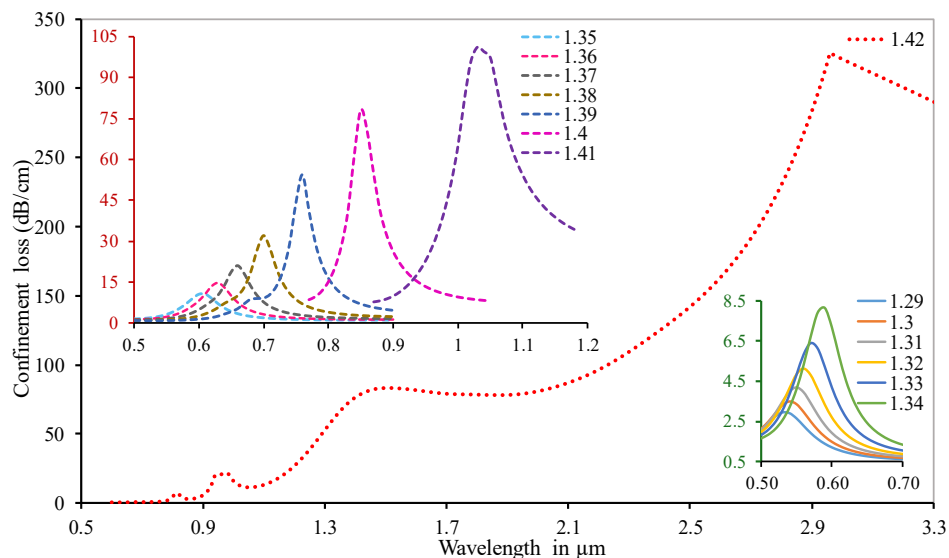


Figure 4.19: Descriptive presentation of Confinement Losses with different operating wavelength for RI of 1.29 to 1.42.

a lower operating wavelength of 530 nm to a higher wavelength of 2960 nm with the increment of RI. The phase matching condition steps to a higher wavelength since RI greatly influences the effective mode index. The lower profoundness of the CL is found at RI = 1.29, and deepness increases with the increment of RI. The average value of the CL is 47.99 dB/cm with a step size of 0.01. All the necessary data are summarized in table 4.10 and CL curve with RI = 1.39 has the most expected sharp peak with the lowest FWHM and highest DA to avoid false detection. FWHM increases for both increment and decrement of the RI from 1.39. Again, figure 4.20 shows the intensity curve of the CLEs for RI = 1.29 to 1.42 with a wavelength of 0.50 μm to 3.00 μm that is an alternative to indicate the shifting of resonance wavelength.

### 4.3.3 Wavelength Sensitivity

In this subsection, the variation of the resonance peak of the CL is measured to determine the variation of RI. Here, through the wavelength interrogation method, sensitivity is calculated for each unit of RI known as RIU for both normal and inclined approaches of the air holes using Eqn. 3.5.



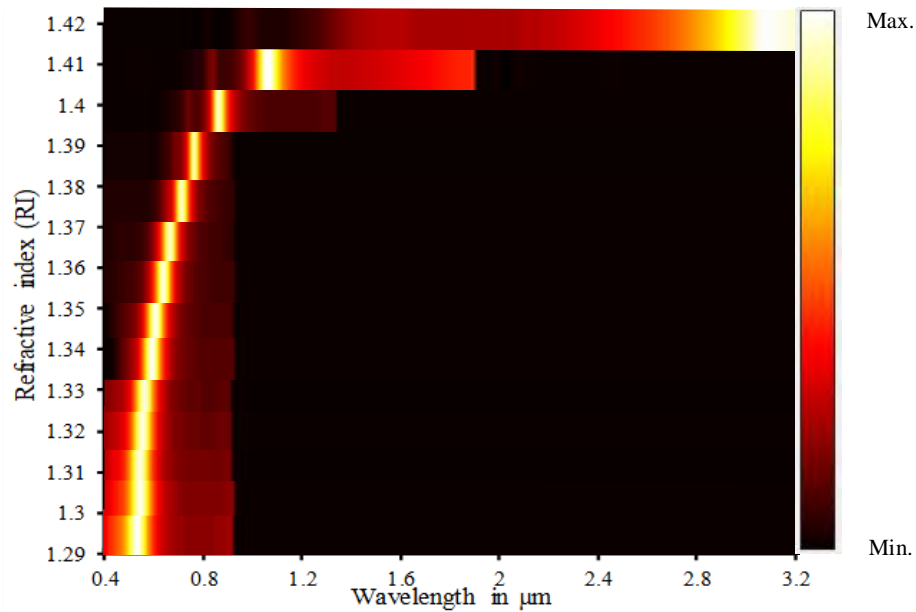


Figure 4.20: Graphical representation of confinement losses through intensity for analytes with RI = 1.29 to RI = 1.42.

#### 4.3.3.1 Normal Approach

From figure 4.18 the maximum CLEs are obtained at the resonant wavelengths of 570 nm, 580 nm, 600 nm, 620 nm, 640 nm, 670 nm, 710 nm, 760 nm, 840 nm, 970 nm, and 1190 nm respectively for the value of RI from 1.33, 1.34, 1.35, 1.36, 1.37, 1.38, 1.39, 1.40, 1.41 and 1.42 respectively in y-polarized mode. Necessary data in figure 4.18 are concise in Table 4.9. The shifting of the resonant wavelengths are 10 nm, 20 nm, 20 nm, 20 nm, 30 nm, 40 nm, 50 nm, 80 nm, 130 nm, and 220 nm with a corresponding WS of 1000 nm/RIU, 2000 nm/RIU, 2000 nm/RIU, 2000 nm/RIU, 3000 nm/RIU, 4000 nm/RIU, 5000 nm/RIU, 8000 nm/RIU, 13000 nm/RIU, and 22000 nm/RIU at RI of 1.33, 1.34, 1.35, 1.36, 1.37, 1.38, 1.39, 1.40, 1.41 and 1.42 respectively. From Table 4.9, the maximum WS is 22,000 nm/RIU at a RI of 1.42 and the average WS is 6,200 nm/RI.

#### 4.3.3.2 Inclined Approach

From figure 4.19, the variation of RI is from 1.29 to 1.42 with a step size of 0.01 and the variation of the resonance wavelength peak are 10, 10, 10, 10, 20, 20, 20, 30, 40, 60, 90, 170 and 1940 nm in between two adjacent RI for y polarized light. From table 4.10, the maximum WS is 194000 nm/RIU with an average WS of 18692.3 nm/RIU. The RI detection range of our proposed sensor is from 1.29 to 1.42, and in figure 4.17, the CL

Table 4.9: Performance Analysis of the Proposed Sensor for Different Analyte RI With  $\Delta n_a = 0.01$ ,  $t_g = 30$  nm at Y-Polarized Mode.

Analyte RI	Maximum confinement loss (dB/cm)	Sensor length (cm)	Resonance Peak shift (nm)	WS (nm/RIU)	AS (RIU <sup>-1</sup> )	WR (RIU)
1.33	0.439	2.278	0.57	1000	63.82	$1 \times 10^{-4}$
1.34	0.554	1.805	0.58	2000	81.78	$5 \times 10^{-5}$
1.35	0.726	1.377	0.60	2000	113.37	$5 \times 10^{-5}$
1.36	0.962	1.040	0.62	2000	161.76	$5 \times 10^{-5}$
1.37	1.38	0.725	0.64	3000	246.83	$3.33 \times 10^{-5}$
1.38	1.94	0.515	0.67	4000	391.08	$2.5 \times 10^{-5}$
1.39	2.88	0.347	0.71	5000	710.84	$2 \times 10^{-5}$
1.40	4.64	0.216	0.76	8000	1242.48	$1.5 \times 10^{-5}$
1.41	7.86	0.127	0.84	13000	1782.56	$7.6 \times 10^{-6}$
1.42	14.6	0.0685	0.97	22000	862.31	$4.54 \times 10^{-6}$
1.43	23.4	0.0427	1.19	N/A	N/A	N/A

intensity of each analyte is shown by normalized value. It moves to a higher wavelength making a clear separation with the increasing RI. This shifting of wavelength helps to get better WS, and WS along with FWHM help to get a good FOM. Although FWHM is lower at RI = 1.39, FOM increases due to the constant increasing nature of WS. The maximum FOM (RIU<sup>-1</sup>) value is 1732.143 for RI = 1.41, and the average FOM is 201.15 RIU<sup>-1</sup>.

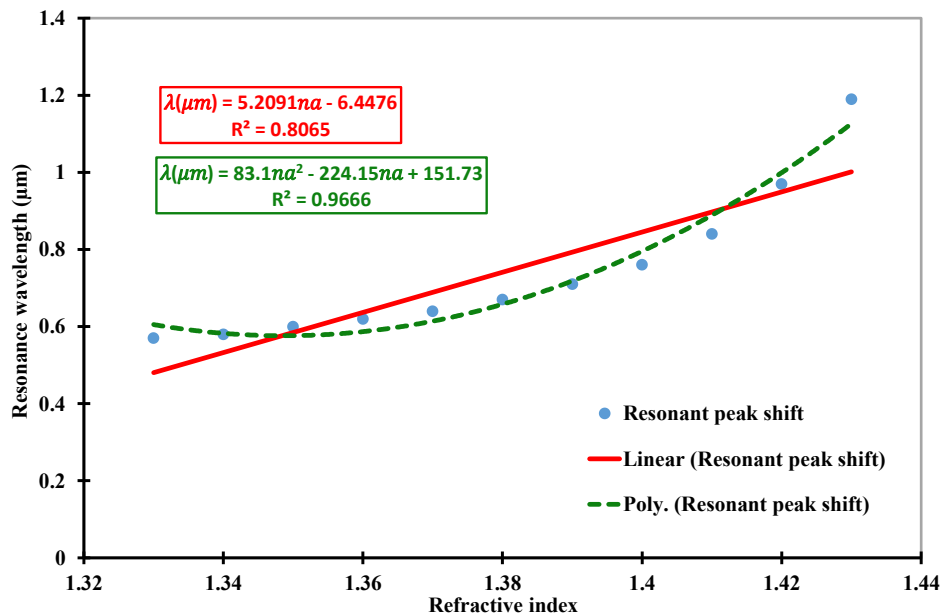


Figure 4.21: Peak shift of resonant wavelength with the variation of RI.

### 4.3.4 Linearity

Linear fitting (binomial function) and polynomial fitting (trinomial function) of the resonant peak shift are plotted in figure 4.21 by the red solid line and green dotted line respectfully. These curve fittings are done with the help of the following equation  $\lambda(\mu m) = 5.209n_a - 6.4476$  with  $R^2 = 0.8065$  and  $\lambda(\mu m) = 83.1n_a^2 - 224.15n_a + 151.73$  with  $R^2 = 0.9666$  respectively for  $n_a(RI)$  within 1.33 to 1.42 and later one provides better than the former one and  $R^2 = 0.9666$  indicates that it is close to ideal.

Again, the curve fitting of the resonance peak shift for inclined approach of air holes is shown in figure 4.22 through the following polynomial equation  $y = 5E+07x^6 - 4E+08x^5 + 1E+09x^4 - 3E+09x^3 + 3E+09x^2 - 1E+09x + 3E+08$  having  $R^2 = 0.9883$  which indicates the perfect fitting of the resonance curve and ideality.

### 4.3.5 Amplitude Sensitivity and Sensor length

The loss of the core depends on the change of the RI, and core loss varies enormously with the RI variation,  $\Delta n_a$ . The transmitted power is observed at a static wavelength in phase matching conditions. AS is an important way to measure the performance of the proposed sensor. It is calculated using the Eqn. 3.6 and it depends on the CL of two adjacent RI. SL is calculated using Eqn. 3.7.

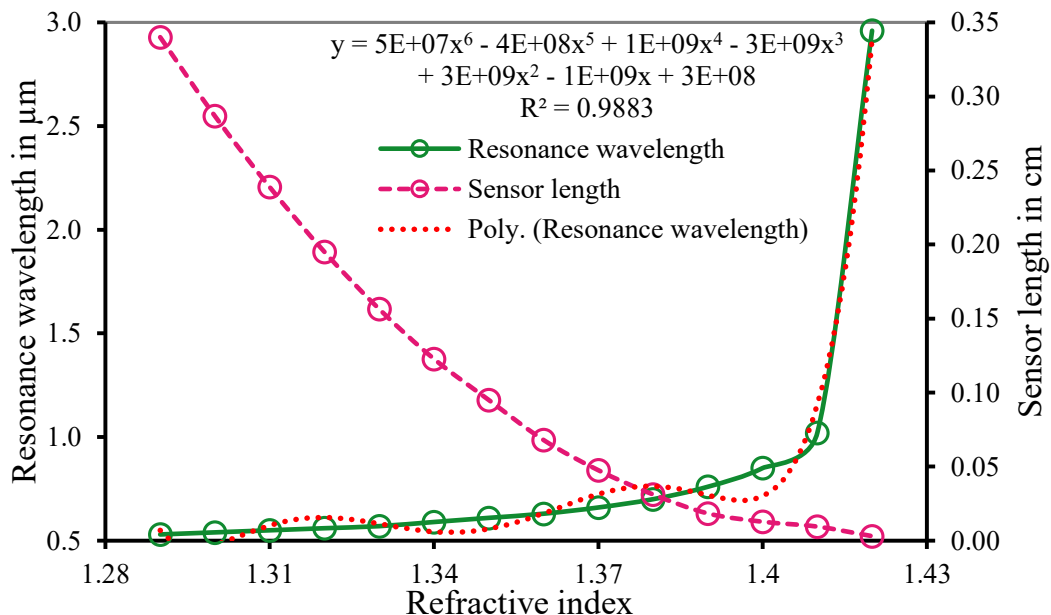


Figure 4.22: Propagation length and peak shift of the proposed sensor with various RI for the inclined approach of air holes.

Table 4.10: Performance Investigation of the Proposed Sensor with  $t_{cu} = 25$  nm,  $\Phi = 35$  deg. and  $\Delta n_a = 0.01$  using Analytes of Different RI.

na	$CL_{max}$ (dB/cm)	$\lambda$ (nm)	$\Delta\lambda$ (nm)	L cm	WS (nm/RIU)	WR (RIU)	AS (1/RIU)	FWHM (nm)	DA (1/nm)	FOM (1/RIU)
1.29	2.941	530	10	0.34002	1000	$1 \times 10^{-4}$	-30.181	128.5	0.007782	7.782101
1.3	3.488	540	10	0.286697	1000	$1 \times 10^{-4}$	-36.646	106.5	0.00939	9.389671
1.31	4.188	550	10	0.238777	1000	$1 \times 10^{-4}$	-45.091	94	0.010638	10.6383
1.32	5.128	560	10	0.195008	1000	$1 \times 10^{-4}$	-56.526	85.5	0.011696	11.69591
1.33	6.395	570	20	0.156372	2000	$5 \times 10^{-4}$	-73.095	79.75	0.012539	25.07837
1.34	8.148	590	20	0.12273	2000	$5 \times 10^{-4}$	-98.722	75	0.013333	26.66667
1.35	10.524	610	20	0.095021	2000	$5 \times 10^{-4}$	-139.252	71	0.014085	28.16901
1.36	14.704	630	30	0.068009	3000	$3.33 \times 10^{-5}$	-213.333	64.35	0.01554	46.62005
1.37	21.01	660	40	0.047596	4000	$2.5 \times 10^{-5}$	-350.568	58	0.017241	68.96552
1.38	32.037	700	60	0.031214	6000	$1.67 \times 10^{-5}$	-677.522	50.75	0.019704	118.2266
1.39	54.344	760	90	0.018401	9000	$1.11 \times 10^{-5}$	-1024.23	43.75	0.022857	205.7143
1.4	78.178	850	170	0.012791	17000	$5.88 \times 10^{-6}$	-1103.603	52.5	0.019048	323.8095
1.41	105.342	1020	1940	0.009493	194000	$5.15 \times 10^{-7}$	-169.686	112	0.008929	1732.143
1.42	325.538	2960	NA	0.003072	NA	NA	NA	NA	NA	NA

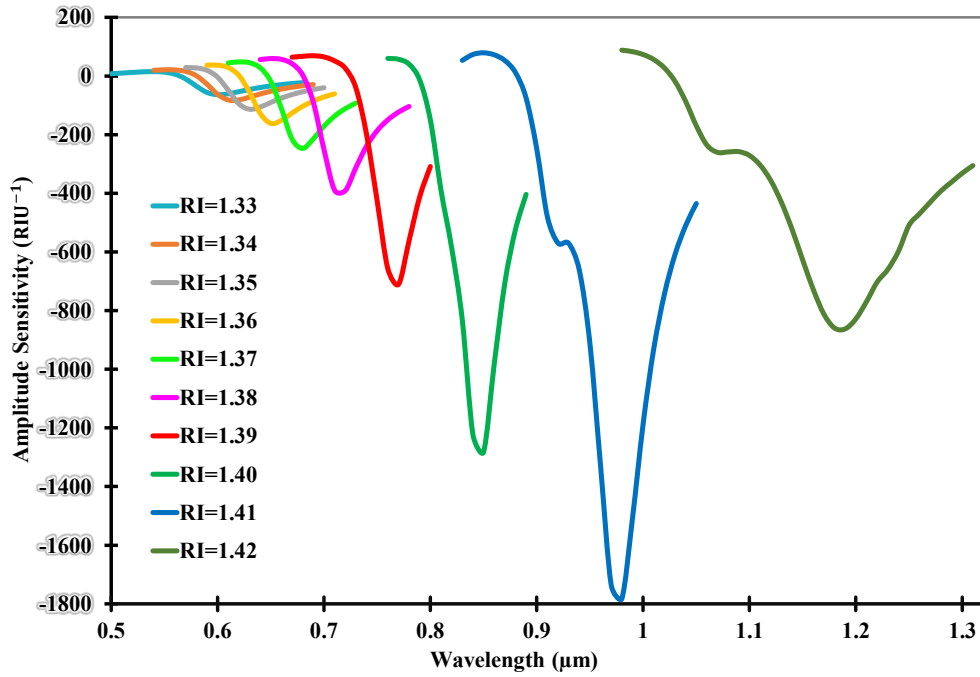


Figure 4.23: Amplitude sensitivity concerning wavelength for the value of RI from 1.33 to 1.43 in y-polarized mode.

#### 4.3.5.1 Normal Approach

From figure 4.21, the maximum CLEs are 0.439 dB/cm, 0.554 dB/cm, 0.726 dB/cm, 0.962 dB/cm, 1.38 dB/cm, 1.94 dB/cm, 2.88 dB/cm, 4.64 dB/cm, 7.86 dB/cm, 14.6 dB/cm, and 23.4 dB/cm at the resonant wavelength of 570 nm, 580 nm, 600 nm, 620 nm, 640 nm, 670 nm, 710 nm, 760 nm, 840 nm, 970 nm, and 1190 nm respectively for the value of RI from 1.33 to 1.43 with a increment of 0.01 in y-polarized mode. Now the corresponding AS are  $62.82 \text{ RIU}^{-1}$ ,  $81.78 \text{ RIU}^{-1}$ ,  $113.37 \text{ RIU}^{-1}$ ,  $161.759 \text{ RIU}^{-1}$ ,  $246.83 \text{ RIU}^{-1}$ ,  $391.085 \text{ RIU}^{-1}$ ,  $710.84 \text{ RIU}^{-1}$ ,  $1282.48 \text{ RIU}^{-1}$ ,  $1782.56 \text{ RIU}^{-1}$  and  $862.31 \text{ RIU}^{-1}$  at RI of 1.33, 1.34, 1.35, 1.36, 1.37, 1.38, 1.39, 1.40, 1.41, and 1.42 respectively, and necessary data are summarized in Table 4.9. From Table 4.9, the maximum AS is  $1782.56 \text{ RIU}^{-1}$  at a RI of 1.41 and the average AS is  $569.683 \text{ RIU}^{-1}$ . Sensor length or propagation length is an auxiliary parameter to measure the RI of various analytes and it can be obtained using Eqn. 3.7. It provides an alternative way to detect analytes of various RI and it can be anticipated that the sensor length for a particular RI is only dependable on the CL. From figure 4.18, it is observed that CL increases with the rise of the RI and it results in the decrements of the sensor length as depicted in figure 4.24.

From Table 4.9, the maximum sensor length is 2.278 cm, and the minimum sensor length is  $42.7 \mu\text{m}$  for an analyte RI of 1.33 and 1.43, respectively. So, we can conclude that a sensor with a size of a few micrometers to a few centimeters may be used to detect

different analytes for the normal approach of the air holes.

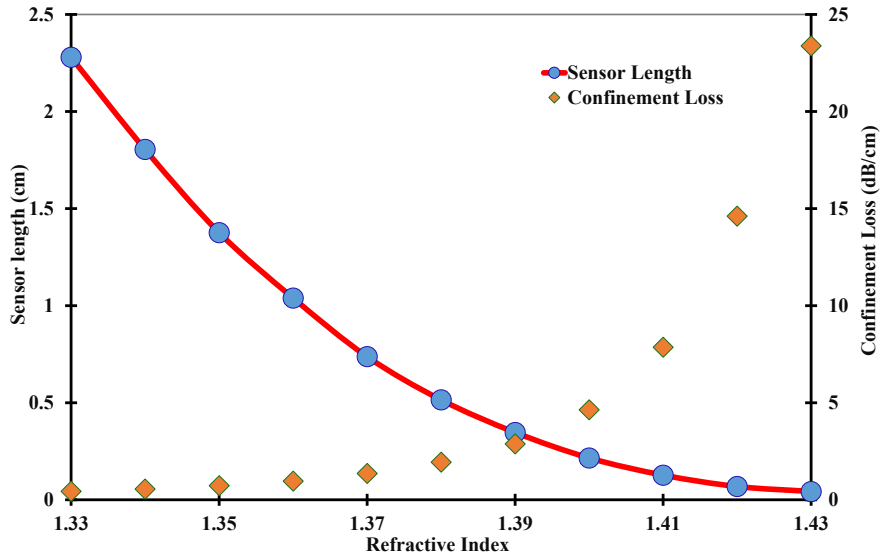


Figure 4.24: Sensor length with different analyte RI for normal approach.

#### 4.3.5.2 Inclined Approach

For the inclined approach of the air holes, Table 4.10 shows the numerical records including AS for RI = 1.29 to RI = 1.42 with a difference of 0.01. The graphical representation of AS is shown in figure 4.25 with proper labeling. At a RI of 1.40, the maximum AS  $RIU^{-1}$  of -1103.603 is found and the average As  $RIU^{-1}$  is -308.624. The peak of the AS also shifts to the higher wavelength with the increment of RI and it follows the same fashion as the CL curve. Again, figure 4.22 shows the graphical representation of the SL of the proposed sensor for RI = 1.29 to 1.42. SL decreases with the increment of RI because increment in RI helps to increase the CL but CL is inversely proportional to SL. With the help of Table 4.10, the maximum, minimum, and average lengths of the proposed sensor are 0.340 cm, 30.72  $\mu\text{m}$ , and 0.1161 cm respectively. So, for detecting various analytes, the length of the proposed sensor may vary between a few micrometers to a few centimeters for the inclined approach of the air holes and the overall length of the sensor decreases from the previous approach.

#### 4.3.6 Sensor Resolution

The SR of the proposed sensor will be discussed in this subsection. SR of the proposed sensor is calculated utilizing the Eqn. 3.8, which helps to measure the lowest fraction of RI change of analytes that the proposed sensor can identify.

Table 4.11: Performance Investigation of the Proposed Sensor with  $t_{au} = 25$  nm,  $t_{tio_2} = 05$  nm,  $\Phi = 35$  deg. and  $\Delta n_a = 0.01$  using Analytes of Different RI.

na	$CL_{max}$ (dB/cm)	$\lambda$ (nm)	$\Delta\lambda$ (nm)	L cm	WS (nm/RIU)	WR (RIU)	AS (1/RIU)	FWHM (nm)	DA (1/nm)	FOM (1/RIU)
1.29	3.362	540	10	0.297442	1000	$1 \times 10^{-4}$	-33.736	109	0.009174	9.174312
1.3	3.976	550	10	0.251509	1000	$1 \times 10^{-4}$	-40.825	96	0.010417	10.41667
1.31	4.759	560	10	0.210128	1000	$1 \times 10^{-4}$	-50.045	87	0.011494	11.49425
1.32	5.767	570	20	0.1734	2000	$5 \times 10^{-5}$	-63.718	80.5	0.012422	24.84472
1.33	7.158	590	10	0.139704	1000	$1 \times 10^{-4}$	-82.794	76	0.013158	13.15789
1.34	9.009	600	20	0.111	2000	$5 \times 10^{-5}$	-111.853	71.98	0.013893	27.7855
1.35	11.618	620	30	0.086073	3000	$3.33 \times 10^{-5}$	-154.56	68.5	0.014599	43.79562
1.36	15.911	650	30	0.06285	3000	$3.33 \times 10^{-5}$	-229.23	53	0.018868	56.60377
1.37	21.629	680	50	0.046234	5000	$2 \times 10^{-5}$	-377.37	60	0.016667	83.33333
1.38	32.89	730	60	0.030404	6000	$1.67 \times 10^{-5}$	-689.59	56	0.017857	107.1429
1.39	51.2	790	100	0.019531	10000	$1 \times 10^{-5}$	-1138.52	50.5	0.019802	198.0198
1.4	86.015	890	200	0.011626	20000	$5 \times 10^{-6}$	-1136.89	52	0.019231	384.6154
1.41	115.349	1090	2160	0.008669	216000	$4.63 \times 10^{-7}$	-118.989	109	0.009174	1981.651
1.42	688.741	3250	NA	0.001452	NA	NA	NA	0	NA	NA

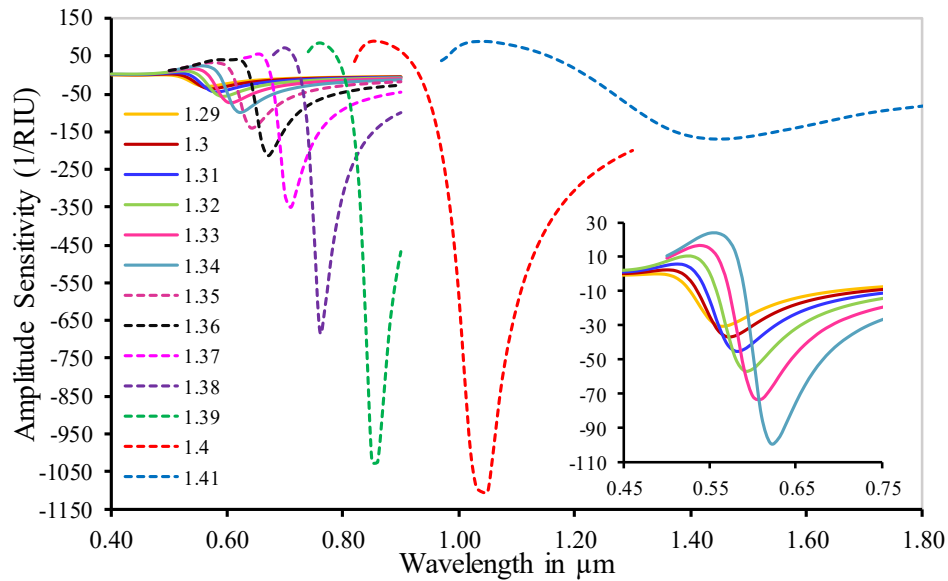


Figure 4.25: Amplitude sensitivity through graphical depiction for the proposed sensor using different analytes with RI of 1.30 to 1.43.

#### 4.3.6.1 Normal Approach

So, from above Eqn. 3.8, it is explicit that resolution is inversely proportional to the resonance wavelength peak shift. A greater resonance shift indicates that the tiniest fraction of RIs can be identified accurately. Table 4.9 has summarized the resolution for different analyte's RI for the normal approach of the air holes, and the top SR for the proposed sensor is  $4.54 \times 10^{-6}$  RIU for RI of 1.42, and it designates that the proposed sensor can detect the change of RI more or less around  $10^{-6}$ .

#### 4.3.6.2 Inclined Approach

All the necessary data associated with SR for inclined approach of the air holes from RI = 1.29 to 1.41 is given in Table 4.10 and through Eqn. 3.8, we can conclude that SR and resonance peak losses are inversely proportionate to each other. The lowest possible fraction of RI change that can be identified by the sensor is  $5.15 \times 10^{-7}$  RIU. SR describes the greater capability of the proposed sensor to detect maximum RI change perfectly around  $10^{-7}$  RIU and the average SR (RIU) for RI = 1.29 to RI = 1.41 is  $4.942 \times 10^{-5}$ . So, from Table 4.9 and table 4.10, we can conclude that the inclined approach has better SR.



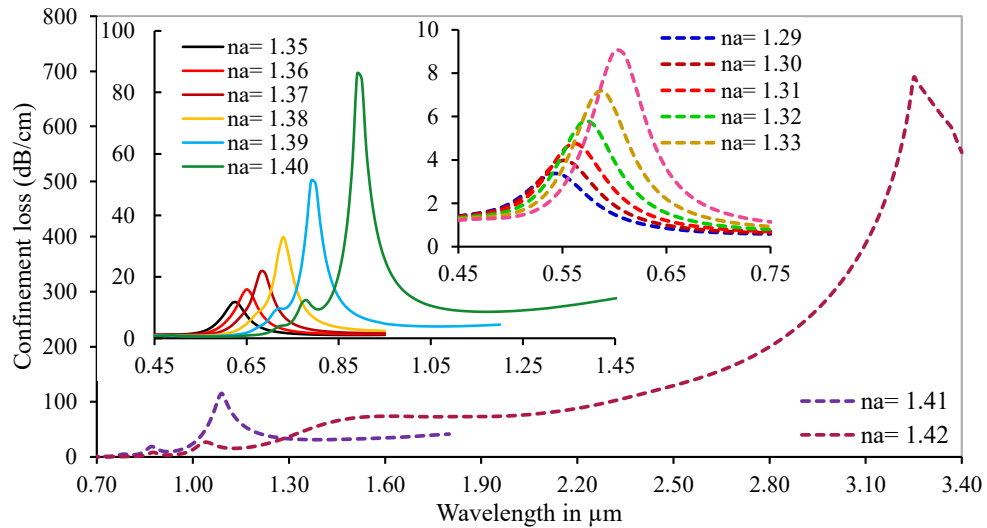


Figure 4.26: Descriptive presentation of Confinement Losses with different operating wavelength for RI of 1.29 to 1.42.

#### 4.3.7 Performance Analysis with Double Layer PM

Figure 4.26 shows the graphical representation of CL for different analytes from RI = 1.29 to RI = 1.42 for the inclined approach of the air holes with a double layer of PM. From figure 4.26, it can be ascertained that the peak of CL shifts from a lower operating wavelength of 540 nm to a higher wavelength of 3250 nm with the increment of RI. The phase matching condition steps to a higher wavelength for double PM than single PM shown in Table 4.10 and 4.11. The lower profoundness of the CL is found at RI = 1.29, and deepness increases with the increment of RI. The average value of the CL is 75.527 dB/cm with a step size of 0.01. All the necessary data are summarized in Table 4.11, and the CL curve with RI = 1.39 has the most expected sharp peak with the lowest FWHM and highest DA to avoid false detection like the single PM proposed model. FWHM increases for both increment and decrement of the RI from 1.39. For the variation of RI is from 1.29 to 1.42 with a step size of 0.01 and the variation of the resonance wavelength peak are 10, 10, 10, 20, 10, 20, 30, 30, 50, 60, 100, 200, and 2160 nm in between two adjacent RI for y- polarized light. From Table 4.11, the maximum WS is 216000 nm/RIU with an average WS of 20846.15 nm/RIU. The RI detection range of our proposed sensor is from 1.29 to 1.42. This shifting of wavelength helps to get better WS and WS along with FWHM help to get a good FOM. Although FWHM is lower at RI = 1.39, FOM increases due to the constant increasing nature of WS. The maximum value of FOM is 1981.651 RIU<sup>-1</sup> for RI = 1.41 and the average FOM (RIU<sup>-1</sup>) is 227.08.

For the inclined approach of the air holes, Table 4.11 shows the numerical records including AS for RI = 1.29 to RI = 1.42 with a difference of 0.01. The graphical

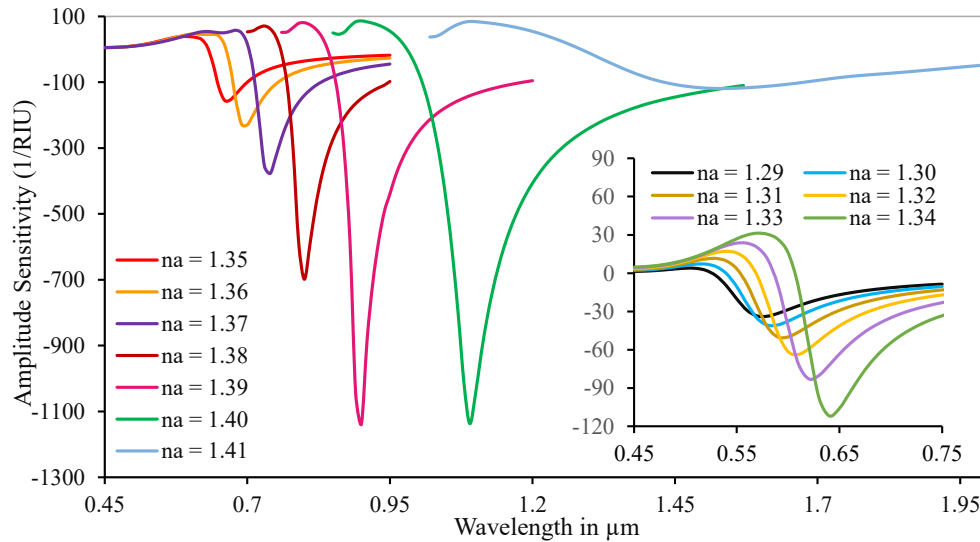


Figure 4.27: Amplitude sensitivity through graphical depiction for the proposed sensor using different analytes with RI of 1.29 to 1.41.

representation of of AS is shown in figure 4.27 with proper labeling. At a RI of 1.39, the maximum AS  $RIU^{-1}$  of -1138.52 is found and the average AS  $RIU^{-1}$  is -325.24. The peak of the AS also shifts to the higher wavelength with the increment of RI and it follows the same fashion as the CL curve.

Table 4.12: Relative Performance Analysis of the Suggested Sensor with the Detection Range of RI.

Ref.	Detection Range of RI	AS ( $RIU^{-1}$ )	WS (nm/ $RIU$ )	WR ( $RIU$ )
[21]	1.420 - 1.530	159.7	11,700	$8.55 \times 10^{-6}$
[22]	1.330 - 1.400	1086	12,000	$8.33 \times 10^{-6}$
[19]	1.330 - 1.410	635.5	11,500	$8.70 \times 10^{-6}$
[20]	1.350 - 1.460	N/A	1,931.03	N/A
[18]	1.330 - 1.400	1085	9,000	$1.11 \times 10^{-5}$
[23]	1.330 - 1.490	N/A	25,900	N/A
[24]	1.330 - 1.400	N/A	11,600	$9.71 \times 10^{-5}$
[75]	1.380 - 1.420	513	4875	$2.50 \times 10^{-5}$
[76]	1.345 - 1.410	N/A	12,450	$8.03 \times 10^{-6}$
[77]	1.300 - 1.310	148	6,000	$0.16 \times 10^{-6}$
[1]	1.330 - 1.380	420.4	4,600	$2.17 \times 10^{-5}$
[78]	1.400 - 1.430	N/A	15,180	$5.68 \times 10^{-6}$
Prop.	1.290 - 1.420	1138.52	216,000	$4.63 \times 10^{-7}$

### 4.3.8 Application

Our proposed biosensor is designed to detect different biological analytes. Examples of bioanalytes include a sequence of nucleic acid (DNA or RNA), a bacterium, a virus

particle, a specific protein, a simple biochemical compound (e.g., glucose, sucrose, fructose etc.) and so on. Except biological analyte our proposed sensor can also detect kerosene, ethanol (solution), Glycerol (solution), water, Methanol (solution), and sugar contents in pepsi, coca-Cola, 7up, sprite, fanta, and mirinda, etc.

Table 4.13: Refractive Indexes of Sucrose Solution.

<b>International Scale (1963) of Refractive Indices of different Sucrose Solutions</b>							
<b>Percentage</b>	<b>Index</b>	<b>Percentage</b>	<b>Index</b>	<b>Percentage</b>	<b>Index</b>	<b>Percentage</b>	<b>Index</b>
0	1.330	25	1.3723	50	1.4200	75	1.4774
1	1.3344	26	1.3740	51	1.4221	76	1.4799
2	1.3359	27	1.3758	52	1.4242	77	1.4825
3	1.3373	28	1.3775	53	1.4264	78	1.4850
4	1.3388	29	1.3793	54	1.4285	79	1.4876
5	1.3403	30	1.3811	55	1.4307	80	1.4901
6	1.3418	31	1.3829	56	1.4329	81	1.4927
7	1.3433	32	1.3847	57	1.4351	82	1.4954
8	1.3448	33	1.3865	58	1.4373	83	1.4980
9	1.3463	34	1.3883	59	1.4396	84	1.5007
10	1.3478	35	1.3902	60	1.4418	85	1.5033
11	1.3494	36	1.3920	61	1.4441		
12	1.3509	37	1.3939	62	1.4464		
13	1.3525	38	1.3958	63	1.4486		
14	1.3541	39	1.3978	64	1.4509		
15	1.3557	40	1.3997	65	1.4532		
16	1.3573	41	1.4016	66	1.4555		
17	1.3589	42	1.4036	67	1.4579		
18	1.3605	43	1.4056	68	1.4603		
19	1.3622	44	1.4076	69	1.4627		
20	1.3638	45	1.4096	70	1.4651		
21	1.3655	46	1.4117	71	1.4676		
22	1.3672	47	1.4137	72	1.4700		
23	1.3689	48	1.4158	73	1.4725		
24	1.3706	49	1.4179	74	1.4749		

#### 4.3.8.1 Concentration Detection of Sucrose Solution

Table 4.13. shows the refractive indices of different sucrose solutions. Here, pure water is considered as 0% sucrose solution and refractive indices varies with the concentrations. variation of sucrose concentration in the solution. This above-mentioned table shows up to 85 percent and the detection range of our proposed sensor is 1.29 to 1.42 and it can detect maximum 50 percent of sucrose solution. The RI of the solution increases with the increment of solution concentration. For detecting the concentration

Table 4.14: Concentration Detection of Different Sucrose solutions.

Concentration %	RI	$CL_{max}$ (dB/cm)	$\lambda$ (nm)	$\Delta\lambda$ (nm)	WS (nm/RIU)	WR (RIU)	AS (1/RIU)	FWHM (nm)	DA (1/nm)	FOM (1/RIU)
0	1.3300	7.158	590	10	970.874	$1.03 \times 10^{-2}$	NA	75	0.01333	12.945
5	1.3403	9.039	600	20	2666.67	$3.75 \times 10^{-3}$	31.002	72	0.01389	37.037
10	1.3478	11.18	620	20	2531.65	$3.95 \times 10^{-3}$	40.264	68	0.01471	37.2301
15	1.3557	13.945	640	20	2469.14	$4.05 \times 10^{-3}$	51.909	65	0.01538	37.9867
20	1.3638	17.848	660	30	3529.41	$2.83 \times 10^{-3}$	68.877	61	0.01639	57.8592
25	1.3723	23.759	690	40	4545.45	$2.20 \times 10^{-3}$	89.206	57	0.01754	79.7448
30	1.3811	32.783	730	60	6593.41	$1.52 \times 10^{-3}$	116.572	54	0.01852	122.1
35	1.3902	50.14	790	100	10526.3	$9.50 \times 10^{-4}$	138.905	50	0.02	210.526
40	1.3997	91.481	890	190	19191.9	$5.21 \times 10^{-4}$	171.601	45.5	0.02198	421.8
45	1.4096	116.709	1080	NA	NA	NA	199.431	100.5	0.00995	NA

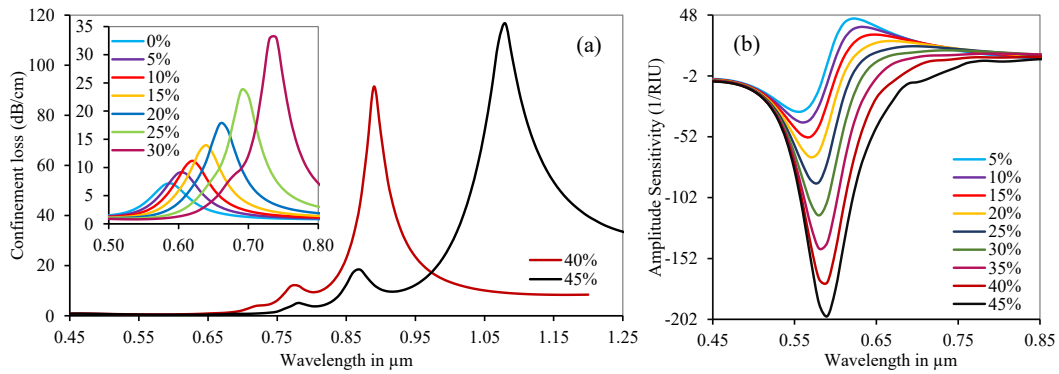


Figure 4.28: Confinement loss (a) and Amplitude sensitivity (b) for different sucrose solutions

of sucrose solution through our proposed sensor, 5% concentration variation is considered. Figure 4.28 (a) shows the CL spectrum labelled with different concentration and resonance peak shifts to right with the increment of sucrose concentration. The maximum value of CL (dB/cm) is 7.158, 9.039, 11.18, 13.945, 17.848, 23.759, 32.783, 50.14, 91.481, and 116.709 for the concentration of 0% to 45% with a step size of 5%. The maximum WS (nm/RIU) is 19191.9 with an average WS (nm/RIU) of 5891.65. All necessary data (WS, WR, FWHM, DA, and FOM) is shown in table 4.14. Figure 4.28 (b) shows the AS of the corresponding CL spectrum and here, 0% sucrose solution is considered as the reference. The depth of AS increases with the increase of sucrose solution concentration. The value of AS (RIU)<sup>-1</sup> is 31.002, 40.264, 51.909, 68.877, 89.206, 116.572, 138.905, 171.601, and 199.431 for 5%, 10%, 15%, 20%, 25%, 30%, 35%, 40%, to 45% sucrose solution respectively. Observing both WS and AS, the concentration of sucrose solution can be identified.

### 4.3.9 Summary

This work presented features; one of the significant findings of this dissertation is the maximum AS approximately 1138.52 RIU<sup>-1</sup> and the maximum WS of 216000 nm/RIU with the analyte RI = 1.39 having a maximum SR of  $4.63 \times 10^{-7}$  RIU. This study has also found an excellent adjusted R<sup>2</sup> of 0.9891 with polynomial curve fitting. Therefore, the higher sensitivity with low confinement loss makes our sensor a potential candidate for detecting any biological and biochemical analyte in the measurement range of 1.29 to 1.42. A relative comparison in Table 4.12 is shown to compare the performance of our proposed sensor with the existing one.

# Chapter 5

## Conclusions

### 5.1 Conclusions

In this dissertation, three different cases of a proposed PCF based SPR sensor are studied and analyzed numerically. The main objective of this thesis is to design and numerically investigate the performance of a PCF based plasmonic biosensor with optimized asymmetric slotted air hole. To that, we have first designed and optimized a PCF based SPR sensor with slotted air holes in a normal approach. Then, the appearance of the air holes has been modified, and the sensor's performance is optimized and calculated. Above mentioned two cases had been studied for single layer PM. Finally, the inclined approach of the air holes has been studied and investigated numerically for the double layer PM. The guiding properties of the proposed sensor are analyzed based on the wavelength and amplitude interrogation method. A summary of our proposed PCF based SPR sensor is given below:

#### 5.1.1 Normal Approach

In this work, a slotted PCF based plasmonic biosensor is considered for the first time, designed and thoroughly analyzed for detecting analytes of different RI using FEM through COMSOL Multiphysics. Based on the numerical results, we can say that our proposed sensor can be used to detect analytes with RI ranging from 1.33 to 1.43. The uppermost WS is 22,000 nm/RIU with a WR of  $4.54 \times 10^{-6}$  RIU for an analyte with RI of 1.42 for y- polarized mode. The maximum AS is  $1782.56 \text{ RIU}^{-1}$  at a RI of 1.41. Moreover, the average AS and WS are  $569.683 \text{ RIU}^{-1}$  and 6,200 nm/RI respectively. The structure of the proposed biosensor is very simple and feasible to manufacture for different applications in biochemical industries as a candidate for detecting different

biochemical and biological analytes.

### 5.1.2 Inclined Approach with Single PM

In this work, a novel PCF is numerically characterized by introducing the inclined approach of the air holes through FEM based mode solver software for bio-analyte sensing within a range from RI = 1.29 to RI = 1.42. To support SPR the entire outer surface of the proposed sensor is covered by the thin gold film (25 nm). Sensing methodology is adequately addressed, and each of the designed parameters of the sensor structure is tuned sufficiently to find out the desired sensing performance. Considering RI changes at the outer surface, appealing sensing performance such as maximum WS of 1,94,000 nm/RIU and maximum AS of 1103.603 RIU<sup>-1</sup> is attained. In addition, the proposed sensor possesses a resolution of  $5.15 \times 10^{-7}$  RIU, linearity of 0.9883, FOM of 1732.143 RIU<sup>-1</sup>, and DA of 0.022857 nm<sup>-1</sup>.

### 5.1.3 Inclined Approach with Double PM

Both of the above mentioned works have used single PM but here, we have used a thin layer of TiO<sub>2</sub> of 5nm as an adhesive layer in between the gold and SiO<sub>2</sub>. For considering the extra layer of TiO<sub>2</sub>, the sensing performance of the proposed sensor has been given in Table 5.1.

Table 5.1: Performance Comparison of Proposed Sensor for Single and Double PM within a Range from RI = 1.29 to RI = 1.42.

Parameter List	Parameter Value	
	Single PM	Double PM
AS (RIU <sup>-1</sup> )	1103.603	1138.52
WS (nm/RIU)	194000	216000
WR (RIU)	$5.15 \times 10^{-7}$	$4.63 \times 10^{-7}$
FOM (RIU <sup>-1</sup> )	1732.143	1981.651
DA (nm <sup>-1</sup> )	0.022857	0.019802
Linearity	0.9883	0.9891

## 5.2 Future Prospects of Our Work

With the advancement of technology, PCF based SPR sensing is a competitive and promising scheme. However, from the point of practical implementation, significant progress has not been made to ease the fabrication challenges, and the performance of

the proposed model is still under question for this circumstance. Due to this critical limitation, a few experimental works are reported, and most of the reported research based on PCF-SPR is carried by theoretical and simulation models. Therefore, investigating PCF sensors with a wide range of refractive indices experimentally in practical applications can be a potential future work. Further potential future work may focus on

i) Proof of concept demonstration to real PCF based SPR sensor development and to use different background materials for the proposed model

ii) In this research work, the noble PM gold (Au) is used. Other PMs such as Silver, Copper and Aluminium can be used to measure the performance of the proposed sensor and investigate the changes in overall performance due to the change of PM.

iii) Here,  $\text{TiO}_2$  is used as an adhesive material to reduce the limitation of gold and uplift the overall performance. Other adhesive materials that may be used with gold or  $\text{TiO}_2$  may be investigated with Silver, Aluminum, and Copper. Detection of analytes from more chemical and biological samples may be studied.

iv) The proposed model is designed to detect a single analyte at a time. So, modification can be done in the proposed structure to detect multiple analytes simultaneously.

v) Our thesis work is based on the external sensing scheme. So, internal sensing or both internal and external sensing schemes may be explored to give more flexibility, observe the sensing performance practically, and compare the experimental results with the simulation ones.



## References

- [1] M. R. Hasan, S. Akter, A. A. Rifat, S. Rana, K. Ahmed, R. Ahmed, H. Subbaraman, and D. Abbott, "Spiral photonic crystal fiber-based dual-polarized surface plasmon resonance biosensor," *IEEE Sensors Journal*, vol. 18, no. 1, pp. 133–140, 2017.
- [2] L. Papa, "Diagnostic method and sensor device for detecting lesions in body tissues," Jan. 22 1980, "U.S. Patent 4,184,486". [Online]. Available: "<https://patents.google.com/patent/US4184486A/en>"
- [3] M. A. Mollah, M. Yousufali, I. M. Ankan, M. M. Rahman, H. Sarker, and K. Chakrabarti, "Twin core photonic crystal fiber refractive index sensor for early detection of blood cancer," *Sensing and Bio-Sensing Research*, vol. 29, p. 100344, 2020.
- [4] N. Jahan, M. M. Rahman, M. Ahsan, M. A. Based, M. M. Rana, S. Gurusamy, and J. Haider, "Photonic crystal fiber based biosensor for pseudomonas bacteria detection: A simulation study," *IEEE Access*, vol. 9, pp. 42 206–42 215, 2021.
- [5] M. Al Mahfuz, M. A. Hossain, E. Haque, N. H. Hai, Y. Namihira, and F. Ahmed, "Dual-core photonic crystal fiber-based plasmonic ri sensor in the visible to near-ir operating band," *IEEE Sensors Journal*, vol. 20, no. 14, pp. 7692–7700, 2020.
- [6] M. A. Mollah and M. S. Islam, "Novel single hole exposed-suspended core localized surface plasmon resonance sensor," *IEEE Sensors Journal*, vol. 21, no. 3, pp. 2813–2820, 2020.
- [7] M. De, T. K. Gangopadhyay, and V. K. Singh, "Prospects of photonic crystal fiber for analyte sensing applications: an overview," *Measurement Science and Technology*, vol. 31, no. 4, p. 042001, 2020.
- [8] A. Nooke, U. Beck, A. Hertwig, A. Krause, H. Krüger, V. Lohse, D. Negendank, and J. Steinbach, "On the application of gold based spr sensors for the detection of hazardous gases," *Sensors and Actuators B: Chemical*, vol. 149, no. 1, pp. 194–198, 2010.

- [9] M. S. Islam, M. R. Islam, J. Sultana, A. Dinovitser, B. W.-H. Ng, and D. Abbott, "Exposed-core localized surface plasmon resonance biosensor," *JOSA B*, vol. 36, no. 8, pp. 2306–2311, 2019.
- [10] Z.-W. Ding, T.-T. Lang, Y. Wang, and C.-L. Zhao, "Surface plasmon resonance refractive index sensor based on tapered coreless optical fiber structure," *Journal of Lightwave Technology*, vol. 35, no. 21, pp. 4734–4739, 2017.
- [11] T. Wu, Y. Shao, Y. Wang, S. Cao, W. Cao, F. Zhang, C. Liao, J. He, Y. Huang, M. Hou *et al.*, "Surface plasmon resonance biosensor based on gold-coated side-polished hexagonal structure photonic crystal fiber," *Optics express*, vol. 25, no. 17, pp. 20 313–20 322, 2017.
- [12] L. Coelho, J. de Almeida, J. Santos, R. Ferreira, P. André, and D. Viegas, "Sensing structure based on surface plasmon resonance in chemically etched single mode optical fibres," *Plasmonics*, vol. 10, no. 2, pp. 319–327, 2015.
- [13] R. Jha and G. Badenes, "Effect of fiber core dopant concentration on the performance of surface plasmon resonance-based fiber optic sensor," *Sensors and Actuators A: Physical*, vol. 150, no. 2, pp. 212–217, 2009.
- [14] W. Luo, X. Li, J. Meng, Y. Wang, and X. Hong, "Surface plasmon resonance sensor based on side-polished d-shaped photonic crystal fiber with split cladding air holes," *IEEE Transactions on Instrumentation and Measurement*, vol. 70, pp. 1–11, 2021.
- [15] F. Haider, R. A. Aoni, R. Ahmed, W. J. Chew, and G. A. Mahdiraji, "Alphabetic-core assisted microstructure fiber based plasmonic biosensor," *Plasmonics*, vol. 15, no. 6, pp. 1949–1958, 2020.
- [16] F. Haider, M. Mashrafi, R. A. Aoni, R. Haider, M. Hossen, T. Ahmed, G. A. Mahdiraji, and R. Ahmed, "Multi-analyte detection based on integrated internal and external sensing approach," *IEEE Transactions on NanoBioscience*, 2021.
- [17] Y. E. Monfared and M. Qasymeh, "Plasmonic biosensor for low-index liquid analyte detection using graphene-assisted photonic crystal fiber," *Plasmonics*, vol. 16, no. 3, pp. 881–889, 2021.
- [18] A. K. Paul, A. K. Sarkar, A. B. S. Rahman, and A. Khaleque, "Twin core photonic crystal fiber plasmonic refractive index sensor," *IEEE Sensors Journal*, vol. 18, no. 14, pp. 5761–5769, 2018.

- [19] A. K. Paul, A. K. Sarkar, and A. Khaleque, "Dual-core photonic crystal fiber plasmonic refractive index sensor: a numerical analysis," *Photonic Sensors*, vol. 9, no. 2, pp. 151–161, 2019.
- [20] Z. Guo, Z. Fan, X. Kong, and Z. Meng, "Photonic crystal fiber based wide-range of refractive index sensor with phase matching between core mode and metal defect mode," *Optics Communications*, vol. 461, p. 125233, 2020.
- [21] A. K. Paul, M. S. Habib, N. H. Hai, and S. A. Razzak, "An air-core photonic crystal fiber based plasmonic sensor for high refractive index sensing," *Optics Communications*, vol. 464, p. 125556, 2020.
- [22] M. Al Mahfuz, M. A. Mollah, M. R. Momota, A. K. Paul, A. Masud, S. Akter, and M. R. Hasan, "Highly sensitive photonic crystal fiber plasmonic biosensor: Design and analysis," *Optical Materials*, vol. 90, pp. 315–321, 2019.
- [23] H. Han, D. Hou, L. Zhao, N. Luan, L. Song, Z. Liu, Y. Lian, J. Liu, and Y. Hu, "A large detection-range plasmonic sensor based on an h-shaped photonic crystal fiber," *Sensors*, vol. 20, no. 4, p. 1009, 2020.
- [24] P. Bing, J. Sui, G. Wu, X. Guo, Z. Li, L. Tan, and J. Yao, "Analysis of dual-channel simultaneous detection of photonic crystal fiber sensors," *Plasmonics*, pp. 1–6, 2020.
- [25] M. Yousufali, M. A. Mollah, and K. Ahmed, "Multimode interference-based photonic crystal fiber glucose sensor," *Plasmonics*, vol. 16, no. 3, pp. 811–818, 2021.
- [26] M. A. Mahfuz, M. Hossain, E. Haque, N. H. Hai, Y. Namihira, F. Ahmed *et al.*, "A bimetallic-coated, low propagation loss, photonic crystal fiber based plasmonic refractive index sensor," *Sensors*, vol. 19, no. 17, p. 3794, 2019.
- [27] M. A. Jabin, K. Ahmed, M. J. Rana, B. K. Paul, M. Islam, D. Vigneswaran, and M. S. Uddin, "Surface plasmon resonance based titanium coated biosensor for cancer cell detection," *IEEE Photonics Journal*, vol. 11, no. 4, pp. 1–10, 2019.
- [28] V. Koubova, E. Brynda, L. Karasova, J. Škvor, J. Homola, J. Dostalek, P. Tobiška, and J. Rošický, "Detection of foodborne pathogens using surface plasmon resonance biosensors," *Sensors and Actuators B: Chemical*, vol. 74, no. 1-3, pp. 100–105, 2001.
- [29] S. Fang, H. J. Lee, A. W. Wark, and R. M. Corn, "Attomole microarray detection of micrornas by nanoparticle-amplified spr imaging measurements of surface polyadenylation reactions," *Journal of the American Chemical Society*, vol. 128, no. 43, pp. 14 044–14 046, 2006.

- [30] X. Fan and I. M. White, "Optofluidic microsystems for chemical and biological analysis," *Nature photonics*, vol. 5, no. 10, p. 591, 2011.
- [31] T. Akimoto, S. Sasaki, K. Ikebukuro, and I. Karube, "Refractive-index and thickness sensitivity in surface plasmon resonance spectroscopy," *Applied optics*, vol. 38, no. 19, pp. 4058–4064, 1999.
- [32] T. Ahmed, A. K. Paul, M. S. Anower, and S. A. Razzak, "Surface plasmon resonance biosensor based on hexagonal lattice dual-core photonic crystal fiber," *Applied Optics*, vol. 58, no. 31, pp. 8416–8422, 2019.
- [33] J. Homola, "Surface plasmon resonance sensors for detection of chemical and biological species," *Chemical reviews*, vol. 108, no. 2, pp. 462–493, 2008.
- [34] K. Ahmed, M. J. Haque, M. A. Jabin, B. K. Paul, I. S. Amiri, and P. Yupa-pin, "Tetra-core surface plasmon resonance based biosensor for alcohol sensing," *Physica B: Condensed Matter*, vol. 570, pp. 48–52, 2019.
- [35] I. Stemmler, A. Brecht, and G. Gauglitz, "Compact surface plasmon resonance-transducers with spectral readout for biosensing applications," *Sensors and Actuators B: Chemical*, vol. 54, no. 1-2, pp. 98–105, 1999.
- [36] A. P. Turner, "Biosensors: Fundamentals and applications—historic book now open access," *Biosensors and bioelectronics*, no. 65, p. A1, 2015.
- [37] M. F. O. Hameed and S. Obayya, *Computational photonic sensors*. Springer, 2019. [Online]. Available: "https://link.springer.com/book/10.1007/978-3-319-76556-3"
- [38] S. Atakramians, "Terahertz waveguides: a study of microwires and porous fibres." Ph.D. dissertation, Faculty of Engineering, University of Adelaide, Australia, January, 2011.
- [39] A. A. Rifat, R. Ahmed, A. K. Yetisen, H. Butt, A. Sabouri, G. A. Mahdiraji, S. H. Yun, and F. M. Adikan, "Photonic crystal fiber based plasmonic sensors," *Sensors and Actuators B: Chemical*, vol. 243, pp. 311–325, 2017.
- [40] C.-L. Tien, H.-Y. Lin, and S.-H. Su, "High sensitivity refractive index sensor by d-shaped fibers and titanium dioxide nanofilm," *Soft Matter Photonics*, p. 17, 2018.
- [41] Q. Wang, X.-Z. Wang, H. Song, W.-M. Zhao, and J.-Y. Jing, "A dual channel self-compensation optical fiber biosensor based on coupling of surface plasmon polariton," *Optics & Laser Technology*, vol. 124, p. 106002, 2020.

- [42] H. Heidarzadeh, "Analysis and simulation of a plasmonic biosensor for hemoglobin concentration detection using noble metal nano-particles resonances," *Optics Communications*, vol. 459, p. 124940, 2020.
- [43] J. Zenneck, "Über die fortpflanzung ebener elektromagnetischer wellen längs einer ebenen leiterfläche und ihre beziehung zur drahtlosen telegraphie," *Annalen der Physik*, vol. 328, no. 10, pp. 846–866, 1907.
- [44] A. Sommerfeld, "Über die ausbreitung der wellen in der drahtlosen telegraphie," *Annalen der Physik*, vol. 333, no. 4, pp. 665–736, 1909.
- [45] R. H. Ritchie, "Plasma losses by fast electrons in thin films," *Physical review*, vol. 106, no. 5, p. 874, 1957.
- [46] C. Powell and J. Swan, "Effect of oxidation on the characteristic loss spectra of aluminum and magnesium," *Physical Review*, vol. 118, no. 3, p. 640, 1960.
- [47] E. Stern and R. Ferrell, "Surface plasma oscillations of a degenerate electron gas," *Physical Review*, vol. 120, no. 1, p. 130, 1960.
- [48] A. Otto, "Excitation of nonradiative surface plasma waves in silver by the method of frustrated total reflection," *Zeitschrift für Physik A Hadrons and nuclei*, vol. 216, no. 4, pp. 398–410, 1968.
- [49] E. Kretschmann and H. Raether, "Radiative decay of non radiative surface plasmons excited by light," *Zeitschrift für Naturforschung A*, vol. 23, no. 12, pp. 2135–2136, 1968.
- [50] B. Liedberg, C. Nylander, and I. Lundström, "Biosensing with surface plasmon resonance—how it all started," *Biosensors and Bioelectronics*, vol. 10, no. 8, pp. i–ix, 1995.
- [51] J. Homola, S. S. Yee, and G. Gauglitz, "Surface plasmon resonance sensors," *Sensors and actuators B: Chemical*, vol. 54, no. 1-2, pp. 3–15, 1999.
- [52] R. Ince and R. Narayanaswamy, "Analysis of the performance of interferometry, surface plasmon resonance and luminescence as biosensors and chemosensors," *Analytica chimica acta*, vol. 569, no. 1-2, pp. 1–20, 2006.
- [53] P. V. Lambeck, "Integrated opto-chemical sensors," *Sensors and Actuators B: Chemical*, vol. 8, no. 1, pp. 103–116, 1992.
- [54] S. Blair and Y. Chen, "Resonant-enhanced evanescent-wave fluorescence biosensing with cylindrical optical cavities," *Applied Optics*, vol. 40, no. 4, pp. 570–582, 2001.

- [55] Y. Zhou, A. Dibos, G. Scuri, D. Wild, A. High, L. Jauregui, C. Shu, K. De Greve, K. Pistunova, A. Joe *et al.*, “Tunable strong coupling of excitons in 2d semiconductors to surface plasmon polaritons,” in *APS March Meeting Abstracts*, vol. 2018, 2018, pp. E37–006.
- [56] J. Homola, I. Koudela, and S. S. Yee, “Surface plasmon resonance sensors based on diffraction gratings and prism couplers: sensitivity comparison,” *Sensors and Actuators B: Chemical*, vol. 54, no. 1-2, pp. 16–24, 1999.
- [57] I. Arghir, F. Delport, D. Spasic, and J. Lammertyn, “Smart design of fiber optic surfaces for improved plasmonic biosensing,” *New biotechnology*, vol. 32, no. 5, pp. 473–484, 2015.
- [58] A. K. Sharma, R. Jha, and B. Gupta, “Fiber-optic sensors based on surface plasmon resonance: a comprehensive review,” *IEEE Sensors Journal*, vol. 7, no. 8, pp. 1118–1129, 2007.
- [59] B. Lee, S. Roh, and J. Park, “Current status of micro-and nano-structured optical fiber sensors,” *Optical Fiber Technology*, vol. 15, no. 3, pp. 209–221, 2009.
- [60] J. Homola, *Surface plasmon resonance based sensors*. Springer Science & Business Media, 2006, vol. 4.
- [61] E. M. Elkaramany, M. F. O. Hameed, and S. Obayya, “Fundamentals of photonic crystals,” in *Computational Photonic Sensors*. Springer, 2019, pp. 29–52.
- [62] R. A. Aoni, R. Ahmed, M. M. Alam, and S. Razzak, “Optimum design of a nearly zero ultra-flattened dispersion with lower confinement loss photonic crystal fibers for communication systems,” *Int. J. Sci. Eng. Res*, vol. 4, pp. 1–4, 2013.
- [63] J. Homola, “Present and future of surface plasmon resonance biosensors,” *Analytical and bioanalytical chemistry*, vol. 377, no. 3, pp. 528–539, 2003.
- [64] M. Manuel, B. Vidal, R. López, S. Alegret, J. Alonso-Chamarro, I. Garces, and J. Mateo, “Determination of probable alcohol yield in musts by means of an spr optical sensor,” *Sensors and Actuators B: Chemical*, vol. 11, no. 1-3, pp. 455–459, 1993.
- [65] L. Zhang and D. Uttamchandani, “Optical chemical sensing employing surface plasmon resonance,” *Electronics Letters*, vol. 24, no. 23, pp. 1469–1470, 1988.
- [66] S. Nelson, K. S. Johnston, and S. S. Yee, “High sensitivity surface plasmon resonance sensor based on phase detection,” *Sensors and actuators B: Chemical*, vol. 35, no. 1-3, pp. 187–191, 1996.

- [67] K. Matsubara, S. Kawata, and S. Minami, "Optical chemical sensor based on surface plasmon measurement," *Applied optics*, vol. 27, no. 6, pp. 1160–1163, 1988.
- [68] A. Kruchinin and Y. G. Vlasov, "Surface plasmon resonance monitoring by means of polarization state measurement in reflected light as the basis of a dna-probe biosensor," *Sensors and Actuators B: Chemical*, vol. 30, no. 1, pp. 77–80, 1996.
- [69] K. Saitoh and M. Koshiba, "Full-vectorial finite element beam propagation method with perfectly matched layers for anisotropic optical waveguides," *Journal of lightwave technology*, vol. 19, no. 3, pp. 405–413, 2001.
- [70] D. Ferrarini, L. Vincetti, M. Zoboli, A. Cucinotta, and S. Selleri, "Leakage properties of photonic crystal fibers," *Optics Express*, vol. 10, no. 23, pp. 1314–1319, 2002.
- [71] A. Vial, A.-S. Grimault, D. Macías, D. Barchiesi, and M. L. De La Chapelle, "Improved analytical fit of gold dispersion: Application to the modeling of extinction spectra with a finite-difference time-domain method," *Physical Review B*, vol. 71, no. 8, p. 085416, 2005.
- [72] M. S. Islam, C. M. Cordeiro, J. Sultana, R. A. Aoni, S. Feng, R. Ahmed, M. Doraki, A. Dinovitser, B. W.-H. Ng, and D. Abbott, "A hi-bi ultra-sensitive surface plasmon resonance fiber sensor," *IEEE access*, vol. 7, pp. 79 085–79 094, 2019.
- [73] B. Gauvreau, A. Hassani, M. F. Fehri, A. Kabashin, and M. Skorobogatiy, "Photonic bandgap fiber-based surface plasmon resonance sensors," *Optics express*, vol. 15, no. 18, pp. 11 413–11 426, 2007.
- [74] M. S. Islam, J. Sultana, A. A. Rifat, A. Dinovitser, B. W.-H. Ng, and D. Abbott, "Terahertz sensing in a hollow core photonic crystal fiber," *IEEE Sensors Journal*, vol. 18, no. 10, pp. 4073–4080, 2018.
- [75] C. Liu, W. Su, Q. Liu, X. Lu, F. Wang, T. Sun, and P. K. Chu, "Symmetrical dual d-shape photonic crystal fibers for surface plasmon resonance sensing," *Optics express*, vol. 26, no. 7, pp. 9039–9049, 2018.
- [76] G. Wang, S. Li, G. An, X. Wang, Y. Zhao, W. Zhang, and H. Chen, "Highly sensitive d-shaped photonic crystal fiber biological sensors based on surface plasmon resonance," *Optical and Quantum Electronics*, vol. 48, no. 1, p. 46, 2016.
- [77] T. Huang, "Highly sensitive spr sensor based on d-shaped photonic crystal fiber coated with indium tin oxide at near-infrared wavelength," *Plasmonics*, vol. 12, no. 3, pp. 583–588, 2017.

- [78] M. Liu, X. Yang, P. Shum, and H. Yuan, “High-sensitivity birefringent and single-layer coating photonic crystal fiber biosensor based on surface plasmon resonance,” *Applied optics*, vol. 57, no. 8, pp. 1883–1886, 2018.